

The Iron Yield of Core-collapse Supernovae

ÓSMAR RODRÍGUEZ,¹ DAN MAOZ,¹ AND EHUD NAKAR¹

¹*School of Physics and Astronomy, Tel Aviv University, Tel Aviv 69978, Israel*

ABSTRACT

We present a systematic analysis of 191 stripped-envelope supernovae (SE SNe), aimed to compute their ^{56}Ni masses from the luminosity in their radioactive tails ($M_{\text{Ni}}^{\text{tail}}$) and/or in their maximum light, and the mean ^{56}Ni and iron yields of SE SNe and core-collapse SNe. Our sample consists of SNe Iib, Ib, and Ic from the literature and from the Zwicky Transient Facility Bright Transient Survey. To calculate luminosities from optical photometry, we compute bolometric corrections using 49 SE SNe with optical and near-IR photometry, and develop corrections to account for the unobserved UV and IR flux. We find that the equation of Khatami & Kasen for radioactive ^{56}Ni -powered transients with a single free parameter does not fit the observed peak time-luminosity relation of SE SNe. Instead, we find a correlation between $M_{\text{Ni}}^{\text{tail}}$, peak time, peak luminosity, and decline rate, which allows measuring individual ^{56}Ni masses to a precision of 14%. Applying this method to the whole sample, we find, for SNe Iib, Ib, and Ic, mean ^{56}Ni masses of 0.066 ± 0.006 , 0.082 ± 0.009 , and $0.132 \pm 0.011 M_{\odot}$, respectively. After accounting for their relative rates, for SE SNe as a whole we compute mean ^{56}Ni and iron yields of 0.090 ± 0.005 and $0.097 \pm 0.007 M_{\odot}$, respectively. Combining these results with the recent Type II SN mean ^{56}Ni mass derived by Rodríguez et al., core-collapse SNe, as a whole, have mean ^{56}Ni and iron yields of 0.055 ± 0.006 and $0.058 \pm 0.007 M_{\odot}$, respectively. We also find that radioactive ^{56}Ni -powered models typically underestimate the peak luminosity of SE SNe by 60–70%, suggesting the presence of an additional power source contributing to the luminosity at peak.

Keywords: transients: supernovae — nuclear reactions, nucleosynthesis, abundances

1. INTRODUCTION

Core-collapse (CC) supernovae (SNe) are the explosions of massive stars ($M_{\text{ZAMS}} \gtrsim 8 M_{\odot}$), triggered by the gravitational collapse of their iron cores (see Burrows & Vartanyan 2021 for a current review of the explosion mechanism). Like all SNe, CC SNe are important in multiple astrophysical roles, including as element and dust factories, as kinetic energy sources affecting star formation and galaxy evolution, as the sites of cosmic-ray acceleration, as the progenitors of neutron stars and possibly black holes, and as distance indicators.

CC SNe are spectroscopically separated into two classes: H-rich SNe (SNe II; Minkowski 1941) and stripped-envelope (SE) SNe (Clocchiatti & Wheeler 1997). The latter class includes the H-poor

Type Iib (Filippenko 1988), the H-free Type Ib (Wheeler & Levreault 1985; Elias et al. 1985), and the H-free/He-poor Type Ic (Wheeler & Harkness 1986). Within the latter group, those SNe having line widths $> 15000 \text{ km s}^{-1}$ around maximum light are referred to as broad-line Ic (Ic-BL) SNe, while those associated with gamma-ray bursts (GRBs) are labelled GRB-SNe (see Modjaz et al. 2016). Among SE SNe there are some cases showing narrow emission lines of He (SNe Ibn; Pastorello et al. 2008a) and C and/or O (SNe Icn; Gal-Yam et al. 2021, 2022) in the spectra, indicative of interaction of the ejecta with circumstellar material (CSM). In addition, some SNe Ib and Ic display peculiar double-peaked light curves, such as SNe 2005bf (Anupama et al. 2005; Tominaga et al. 2005; Folatelli et al. 2006), PTF11mb (Taddia et al. 2018a), 2019cad (Gutiérrez et al. 2021), and 2019stc (Gomez et al. 2021). For those SNe, a double-peaked ^{56}Ni distribution in radius within the ejecta and/or the presence of a magnetar are invoked to explain the morphology of their light curves. SNe belonging to

the SN Ibn and Icn subgroups, and those with peculiar double-peaked light curves are not included in the present analysis of SE SNe.

The light curves of SE SNe at early epochs are characterized by a peak in optical/UV bands followed by a rapid decline. The decline feature, thought to be produced by the cooling of the SN progenitor envelope after the shock breakout, depends on the properties of the progenitor system (e.g. Nakar & Piro 2014). This so called cooling phase has been observed in some SNe with early-time data such as SN Iib 1993J (e.g. Richmond et al. 1994), SN Ib 2008D (e.g. Modjaz et al. 2009), and SN Ic 2006aj (e.g. Campana et al. 2006), among others. After the cooling phase, the γ -rays and positrons produced by the decay of radioactive materials synthesized in the explosion power the light curves, which rise to the characteristic peak of SE SNe. This peak, thought to be powered by the radioactive ^{56}Ni decay chain $^{56}\text{Ni} \rightarrow ^{56}\text{Co} \rightarrow ^{56}\text{Fe}$, is characterized by its maximum luminosity so-called peak luminosity (L_{peak}) and the peak time (t_L^{peak}), defined as the date of the peak luminosity minus the explosion epoch. The light curves then decline and, at epochs $\gtrsim 60$ d after explosion, the ejecta becomes optically thin and the luminosity begins to decrease exponentially with time. The latter phase, called the radioactive tail, is also powered by the radioactive ^{56}Ni decay chain in an ejecta with transparency to γ -rays increasing over time (Colgate & McKee 1969). The dependence of the bolometric light curve of SE SNe on the amount of ^{56}Ni synthesized in the explosion enables an estimate of the ^{56}Ni mass yield (M_{Ni}) of these events.

Measuring the ^{56}Ni mass of CC SNe is important for testing the various progenitor scenarios and explosion mechanisms that have been proposed for different CC SNe, as the M_{Ni} yield depends sensitively on the explosion properties and on the core structure of the progenitor (e.g. Suwa et al. 2019). Indeed, analyses of ^{56}Ni mass distributions have shown that SE SNe produce, on average, more ^{56}Ni than SNe II (e.g. Kushnir 2015; Anderson 2019; Meza & Anderson 2020; Sharon & Kushnir 2020; Rodríguez et al. 2021; Afsariardchi et al. 2021), which may suggest significant differences in the progenitor structures and/or explosion properties between both SN types. Equally important, the empirical estimate of the mean ^{56}Ni mass and the iron yield of CC SNe is a critical ingredient for studies of cosmic and Galactic chemical enrichment (e.g. Maoz & Graur 2017; Weinberg et al. 2017).

The most accurate measurement of the ^{56}Ni mass is obtained by observing the luminosity during the radioactive tail (e.g. Sharon & Kushnir 2020; Afsariardchi et al.

2021). Given that luminosities in this phase are available only for a small fraction of SE SNe, alternatives methods have been used to measure ^{56}Ni masses from the early part of the light curve. In particular, the ^{56}Ni masses of SE SNe have been typically estimated through the analytical light-curve model of Arnett (1982) (e.g. Cano 2013; Lyman et al. 2016; Taddia et al. 2015, 2018b, 2019; Prentice et al. 2019; Barbarino et al. 2021) and through Arnett’s rule (e.g. Prentice et al. 2016), which is a prediction of the Arnett model in which the peak luminosity is equal to the heating rate from the decay of ^{56}Ni and ^{56}Co at that time (e.g. Stritzinger & Leibundgut 2005). However, the model of Arnett (1982) was developed for SNe Ia (Dessart et al. 2016; Woosley et al. 2021), so there is no reason to expect that this model and Arnett’s rule provide ^{56}Ni masses of SE SNe much better than order of magnitude estimates. Indeed, numerical models have shown that the Arnett light-curve model and Arnett’s rule overestimate the ^{56}Ni masses of SE SNe (e.g. Dessart et al. 2015, 2016; Khatami & Kasen 2019; Woosley et al. 2021). This was confirmed empirically by Afsariardchi et al. (2021), who found that the ^{56}Ni masses of 27 SE SNe inferred through Arnett’s rule are, on average, greater than those computed from the luminosity in their radioactive tail by a factor of ~ 2 (see also Sharon & Kushnir 2020). The reason why Arnett’s rule is not accurate for SE SNe is that the peak of the luminosity is seen roughly at the time that the time of diffusion of radiation through most of the ejecta towards the observer becomes comparable to the dynamical time. At that time, the observed luminosity includes two components: a significant fraction (but not necessary all) of the instantaneous radioactive heating; and energy that was deposited at earlier times and suffered some adiabatic losses during the ejecta expansion, before it was able to diffuse to the observer. There is no reason to expect that the combination of these two components will match exactly the total instantaneous radioactive energy deposition.

The ^{56}Ni masses of SE SNe have also been computed through hydrodynamical modeling of light curves (e.g. Utrobin 1996; Nakamura et al. 2001; Mazzali et al. 2002; Sauer et al. 2006; Tanaka et al. 2009; Tsvetkov et al. 2009; Folatelli et al. 2014, 2015; Bersten et al. 2012, 2014, 2018; Ergon et al. 2015; Morales-Garoffolo et al. 2015; Bufano et al. 2014; Fremling et al. 2016; Taddia et al. 2016, 2018b; Balakina et al. 2021). In particular, Taddia et al. (2018b) found that the ^{56}Ni masses inferred with the Arnett model are consistent with those computed with the hydrodynamical models generated with the code of

Bersten et al. (2011). This means that if the Arnett model and Arnett’s rule provide similar ^{56}Ni masses, then hydrodynamical models could also overestimate the ^{56}Ni masses of SE SNe.

Based on the energy conservation equation of Katz et al. (2013), Khatami & Kasen (2019) proposed a new relation that, assuming that peak luminosity is powered only by radioactive ^{56}Ni heating, allows to estimate M_{Ni} as a function of L_{peak} , t_L^{peak} , and a dimensionless parameter called β that depends on the spatial distribution of M_{Ni} and on the ejecta opacity, among others parameters. This method was employed by Meza & Anderson (2020) for estimating lower limits for ^{56}Ni masses of 37 SE SNe, using the β parameters suggested in Khatami & Kasen (2019). On the other hand, Afsariardchi et al. (2021) calculated β values for 27 SE SNe with ^{56}Ni masses computed from the luminosity in the radioactive tail. They found that these ^{56}Ni masses and those computed with the Khatami & Kasen (2019) relation and empirical median β values for each SN subtypes are, on average, consistent within 17%. They also found that their empirical β values are systematically lower than those based on the numerical light-curve models of Dessart et al. (2016) and Ertl et al. (2020), among others. This is primarily because the observed sample of Afsariardchi et al. (2021) has significantly higher peak luminosities for a given ^{56}Ni mass than the models mentioned above. Indeed, Ertl et al. (2020) and Woosley et al. (2021) (who recomputed the light curves of Ertl et al. 2020 with a better treatment of the radiation transport) reported that a substantial fraction of observed SE SNe is more luminous than their brightest models, while Sollerman et al. (2022) found that 36% of the SNe Ib/Ic in their sample are brighter than the maximum r -band brightness predicted by models of Woosley et al. (2021). Given that numerical models seem to underestimate the peak luminosities of SE SNe, the use of the Khatami & Kasen (2019) relation and the mean β values computed with these models could, on average, overestimate the ^{56}Ni masses of SE SNe.

The ^{56}Ni mass distribution of SNe I Ib, Ib, and Ic, along with their mean ^{56}Ni masses have been widely analyzed in the literature (e.g. Drout et al. 2011; Cano 2013; Kushnir 2015; Taddia et al. 2015, 2018b, 2019; Lyman et al. 2016; Prentice et al. 2016, 2019; Anderson 2019; Meza & Anderson 2020; Sharon & Kushnir 2020; Afsariardchi et al. 2021; Barbarino et al. 2021; Ouchi et al. 2021). In these works, however, we identify a number of shortcomings affecting the inferred ^{56}Ni masses and the mean M_{Ni} values:

1. The ^{56}Ni masses are mostly computed with the Arnett model or Arnett rule, so those values and the reported mean ^{56}Ni masses are overestimated. Among the works mentioned above, only Sharon & Kushnir (2020) and Afsariardchi et al. (2021) reported accurate ^{56}Ni masses measured from the luminosity in the radioactive tail. However, their samples contain only 11 and 27 SE SNe, respectively, so the reported mean ^{56}Ni masses for each SE SN subtype may not be representative of the SN I Ib, Ib, and Ic populations.
2. The host galaxy reddenings (E_{B-V}) are mostly inferred from the equivalent width of the host galaxy Na ID absorption line (EW_{NaID} , e.g. Turatto et al. 2003; Poznanski et al. 2012) and from color curves (Stritzinger et al. 2018a). The methods of Turatto et al. (2003) and Poznanski et al. (2012) are based on the observed correlation between EW_{NaID} and reddening for SNe Ia and the Milky Way (MW), respectively, so there is no reason to expect such correlations to hold for regions where SE SNe explode. The color method of Stritzinger et al. (2018a) assumes that SNe in the SN I Ib, Ib, and Ic groups have the same intrinsic color curves between zero and 20 d since the time of V -band maximum light. SE SNe are photometrically and spectroscopically diverse, so it is not expected that the color method provide precise E_{B-V} values, while the accuracy of the methodology strongly depends on the completeness of the SN sample used to calibrate the method. Stritzinger et al. (2018a) used only three SNe per SN subtype for calibrating the color method, therefore their E_{B-V} estimates could be, on average, potentially under- or overestimated.
3. The bolometric light curves, necessary to estimate M_{Ni} , can be computed by integrating the spectral energy distribution (SED) constructed with UV, optical, and IR photometry (e.g. Taddia et al. 2018b; Sharon & Kushnir 2020). However, UV and IR photometry is usually available only for bright SNe, so the bolometric correction (BC) technique is used as an alternative method to compute luminosities from optical photometry. Lyman et al. (2014, 2016) presented BCs for SE SNe for the various bands and colors, which are typically used to infer luminosities (e.g. Lyman et al. 2016; Taddia et al. 2019; Afsariardchi et al. 2021; Barbarino et al. 2021). These BCs, however, are based on six or fewer SNe per subtype, and were computed for all SE SNe as

a whole rather than separately for each SN subtype. In addition, the BCs for Sloan bands are based on synthetic, rather than observed, photometry.

Thus, accurate and statistically robust estimations of the mean ^{56}Ni masses of SNe IIB, Ib, and Ic has not been possible so far due to (1) the low number of SNe used to compute BCs, calibrate the color method, and calculate the mean ^{56}Ni masses, and (2) shortcomings in the methodology to compute BCs, E_{B-V} from EW_{NaID} , and ^{56}Ni masses from the early part of the light curves. The number of SE SNe with optical photometry and the fraction with additional UV/IR photometry have increased dramatically in the last ten years. Therefore, it is now feasible to improve the BC determination, the color method calibration, and the ^{56}Ni mass distribution with the newly available data. On the other hand, to solve the shortcomings mentioned above, it is necessary to carry out a new analysis to improve the methods used to compute BC, E_{B-V} , and M_{Ni} . In particular, to further increase the number of SE SNe with ^{56}Ni estimates, it is necessary to investigate alternative methods to accurately infer ^{56}Ni masses from peak times and peak luminosities, such as the [Khatami & Kasen \(2019\)](#) relation and empirical correlations.

The goal of this work is to accurately estimate the mean ^{56}Ni masses of SNe IIB, Ib, and Ic which, combined with the recent mean ^{56}Ni mass for SNe II reported by [Rodríguez et al. \(2021\)](#) and the relative SN rates of [Shivvers et al. \(2017\)](#), allow an evaluation of the mean ^{56}Ni and iron yields of CC SNe as a whole. To this end, we collect and analyze data from a variety of sources for almost 200 SE SNe having photometry near maximum light.

The paper is organized as follows. In Section 2 we present our sample of SNe and their basic properties. In Section 3 we describe the methods we use to measure host galaxy reddenings, bolometric corrections, bolometric light curves, and ^{56}Ni masses. In Section 4 we present the M_{Ni} distribution and the mean ^{56}Ni mass for each SN subtype, and evaluate the mean ^{56}Ni and iron yield of SE SNe and CC SNe as a whole. In particular, in Section 4.2 we show a new correlation between ^{56}Ni mass, peak time, peak luminosity, and decline rate. Comparison to previous work and discussion of systematics appear in Section 5. Our conclusions are summarised in Section 6.

2. DATA SET

For this work, we select SNe IIB, Ib, and Ic (including SNe Ic-BL) from the literature and from the Zwicky Transient Facility (ZTF; [Graham et al. 2019](#);

[Bellm et al. 2019](#); [Masci et al. 2019](#)) Bright Transient Survey¹ (BTS; [Fremming et al. 2020](#); [Perley et al. 2020](#)). From among these SNe we select those (1) in galaxies with known redshift² or with redshifts measured from H II region narrow emission lines in the spectra, and (2) having photometry at maximum light in at least two optical bands in at least one of the following filter systems: Johnson–Kron–Cousins *BVRI*, Sloan *gri*, and/or ZTF *gr*. For the selected SNe, we collect UV, optical, and IR photometry, along with optical and IR spectroscopy. We include the UV photometry taken by the Swift’s Ultraviolet/Optical Telescope (UVOT), which is available at the Swift’s Optical/Ultraviolet Supernova Archive³ (SOUSA; [Brown et al. 2014](#)). When necessary, we convert Sloan *gr* to ZTF *gr*, and vice versa, using the transformations provided in Appendix C. Among the photometry we collect, that obtained by the Carnegie Supernova Project I (CSP-I; [Stritzinger et al. 2018b](#)) is in natural CSP-I photometric systems. We transform the latter photometry to the standard system using the conversions provided in [Krisciunas et al. \(2017\)](#).

Our sample of 191 SNe is listed in Appendix Table F1. This includes the SN name (Column 1) and spectral subtype (Column 2), the host galaxy name (Column 3), the MW reddening E_{B-V}^{MW} (Column 4), the heliocentric SN redshift z (Column 5), the bands of the photometry we use (Column 6), and the references for the data (Column 7). MW reddenings are taken from [Schlafly & Finkbeiner \(2011\)](#), which have an associated random error of 16% ([Schlegel et al. 1998](#)). Throughout this work, for the MW we assume the extinction curve given by [Fitzpatrick \(1999\)](#) with a ratio of total to selective extinction $R_V = A_V/E_{B-V}$ of 3.1. In addition, all phases are divided by $(1+z)$ to account for time-dilation.

3. METHODOLOGY

3.1. ^{56}Ni Mass

3.1.1. ^{56}Ni mass from the radioactive tail luminosity

As mentioned earlier, the most accurate measurement of the ^{56}Ni mass is obtained by observing the bolometric luminosity during the radioactive tail, when the radiation diffusion time t_{diff} is much shorter than the time since the explosion t . At that point in time, all of the deposited radioactive heat that thermalizes in the ejecta escapes almost immediately in the form of IR, optical,

¹ <https://sites.astro.caltech.edu/ztf/bts/explorer.php>

² Available in the NASA/IPAC Extragalactic Database; <http://ned.ipac.caltech.edu>.

³ http://swift.gsfc.nasa.gov/docs/swift/sne/swift_sn.html

and UV radiation, so

$$L(t) = Q(t). \quad (1)$$

Here, L is the bolometric luminosity and Q is the instantaneous energy deposition rate that thermalizes within the ejecta. Since the peak time is observed when $t_{\text{diff}} \approx t$ and as t_{diff} drops roughly as t^{-2} , the ^{56}Ni mass can be accurately determined from the bolometric light curve at $t \gtrsim 3 t_L^{\text{peak}}$.

Under the assumption that the radioactive decay chain $^{56}\text{Ni} \rightarrow ^{56}\text{Co} \rightarrow ^{56}\text{Fe}$ is the unique heating source,

$$Q(t) = M_{\text{Ni}} q(t, t_{\text{esc}}), \quad (2)$$

where M_{Ni} is in units of M_{\odot} , and

$$q(t, t_{\text{esc}}) = q_{\gamma}(t) f_{\text{dep}}(t, t_{\text{esc}}) + q_{\text{pos}}(t). \quad (3)$$

Here, $q_{\gamma}(t)$ and $q_{\text{pos}}(t)$ are the total energy release rates of γ -rays and positron kinetic energy per unit M_{Ni} , respectively, while $f_{\text{dep}}(t, t_{\text{esc}})$ is the γ -ray deposition function, which describes the fraction of the generated γ -ray energy deposited in the ejecta. The terms $q_{\gamma}(t)$ and $q_{\text{pos}}(t)$ are given by

$$q_{\gamma}(t) = \left[6.45 e^{-\frac{t}{\tau_{\text{Ni}}}} + 1.38 e^{-\frac{t}{\tau_{\text{Co}}}} \right] \times 10^{43} \text{ erg s}^{-1}, \quad (4)$$

and

$$q_{\text{pos}}(t) = 0.046 \left[-e^{-\frac{t}{\tau_{\text{Ni}}}} + e^{-\frac{t}{\tau_{\text{Co}}}} \right] \times 10^{43} \text{ erg s}^{-1} \quad (5)$$

(Wygoda et al. 2019), where $\tau_{\text{Ni}} = 8.76$ d and $\tau_{\text{Co}} = 111.4$ d. To represent $f_{\text{dep}}(t, t_{\text{esc}})$ we adopt

$$f_{\text{dep}}(t, t_{\text{esc}}) = 1 - \exp[-(t_{\text{esc}}/t)^2] \quad (6)$$

(Clocchiatti & Wheeler 1997; Jeffery 1999), where t_{esc} is a characteristic time-scale that represents the γ -ray escape time.

To estimate M_{Ni} and t_{esc} for a given observed bolometric light curve in its radioactive-tail phase, we rewrite equation (1) as

$$\log L(t) = \log M_{\text{Ni}} + \log q(t, t_{\text{esc}}). \quad (7)$$

Given that typically $t_L^{\text{peak}} \sim 20$ d, and following Afsariardchi et al. (2021), we consider luminosities at $t > 60$ d as corresponding to the radioactive tail.

Let $\bar{y}(\theta, x)$ be the model that describes the correlation between the observables x and y , where θ is a vector containing the free parameters of the model. Given n measurements of x , y , and their 1σ errors (σ_x, σ_y), we compute θ maximizing the posterior probability

$$p(\theta|x, y, \sigma_x, \sigma_y) = p(\theta)\mathcal{L}(\theta|x, y, \sigma_x, \sigma_y). \quad (8)$$

Here, $p(\theta)$ is the prior function (assumed to be uninformative in this work), and $\mathcal{L}(\theta|x, y, \sigma_x, \sigma_y)$ is the likelihood function given by

$$\ln \mathcal{L}(\theta|x, y, \sigma_x, \sigma_y) = -\frac{1}{2} \sum_{j=1}^n \left[\ln V_j + \frac{(y_j - \bar{y}(\theta, x_j))^2}{V_j} \right], \quad (9)$$

where $V_j = \sigma_{y_j}^2 + (\partial \bar{y} / \partial x)^2 \sigma_{x_j}^2 + \sigma_0^2$ is the variance, and σ_0 is the error not accounted for in the errors in x_j and y_j . To evaluate whether it is necessary to include σ_0 in the variance, we use the Bayesian information criterion (BIC; Schwarz 1978). We compute the maximum likelihood $\ln \mathcal{L}_{\text{max}}$ for two models, one with and one without σ_0 . If the inclusion of σ_0 reduces the value of $\text{BIC} = -2 \ln \mathcal{L}_{\text{max}} + k \ln n$, where k is the number of free parameters, then we include σ_0 as a parameter to compute. We maximize the posterior probability in equation (8) by means of a Markov Chain Monte Carlo process using the python package EMCEE (Foreman-Mackey et al. 2013), which also provides the marginalized distributions of the parameters. We adopt the sample standard deviation ($\hat{\sigma}$) of those distributions as the 1σ error of the free parameters.

In our case, $x = t$, $y = \log L$, and $\theta = \{\log M_{\text{Ni}}, t_{\text{esc}}, \sigma_0\}$, while \bar{y} is given by equation (7). As priors we adopt uniform distributions between -4.0 and 0.3 dex for $\log M_{\text{Ni}}$, between 1 and 500 d for t_{esc} , and between -5.0 and -0.7 for $\log(\sigma_0)$. Since there are three free parameters, we need at least four $\log L$ measurements at $t > 60$ d. In addition, we require a minimum time coverage of 20 d in order to obtain a reliable t_{esc} value.

3.1.2. ^{56}Ni mass from the peak luminosity

Only the best sampled SNe have a detailed bolometric light curve of the radioactive tail that allows an accurate determination of the ^{56}Ni mass. For all other SNe, the ^{56}Ni mass is often determined based on the luminosity and the time of the peak. Since Arnett's rule is not accurate enough, in this paper we use two different approaches. The first is purely empirical, where we use the sample of SNe with ^{56}Ni mass estimation that is based on the radioactive tail to search for the best relation between peak time, peak luminosity, and ^{56}Ni mass. We also extend the search looking for other properties of the light curve near the peak that can improve the accuracy of the ^{56}Ni mass estimate.

The second approach is motivated by theory. Katz et al. (2013) have shown that the integral

$$E(t) = \frac{1}{t} \int_0^t t' (Q(t') - L(t')) dt', \quad (10)$$

where E is the internal energy of the ejecta, offers an energy conservation law that takes the adiabatic losses of the trapped radiation into account.⁴ Based on this equation, Khatami & Kasen (2019) found that the relation between L_{peak} and t_L^{peak} can be approximated by

$$L_{\text{peak}} = \frac{2}{(\beta t_L^{\text{peak}})^2} \int_0^{\beta t_L^{\text{peak}}} Q(t') t' dt'. \quad (11)$$

Here, β is a dimensionless parameter of order unity that depends mainly on the spatial distribution of the heating source and on the opacity of the ejecta. Thus, β can vary from one SN to another (as we later show is indeed the case). Under the assumption that SE SNe at peak are powered *only* by the radioactive ^{56}Ni decay chain, the heating source is given by equation (2), so equation (11) can be written as

$$\log(L_{\text{peak}}/M_{\text{Ni}}) = \log\left(\frac{12.808}{x_{\text{Ni}}^2} \left[1 - \frac{1 + x_{\text{Ni}}}{e^{x_{\text{Ni}}}}\right] + \frac{2.852}{x_{\text{Co}}^2} \left[1 - \frac{1 + x_{\text{Co}}}{e^{x_{\text{Co}}}}\right]\right), \quad (12)$$

where L_{peak} is in units of $10^{43} \text{ erg s}^{-1}$, $x_{\text{Ni}} = \beta t_L^{\text{peak}}/\tau_{\text{Ni}}$, and $x_{\text{Co}} = \beta t_L^{\text{peak}}/\tau_{\text{Co}}$. The average value of β and its variation between different SNe can be inferred from a sample of SNe with known M_{Ni} , L_{peak} , and t_L^{peak} values (e.g. Afsariardchi et al. 2021). The hope is that once calibrated, the peak time-luminosity relation (equation 12) allows, in principle, to estimate the ^{56}Ni mass of SE SNe based solely on measurements of t_L^{peak} and $\log L_{\text{peak}}$.

3.2. Light curve fits

The derivation of ^{56}Ni masses from observed photometric light curves, as outlined above, requires their interpolation in time. To interpolate the light curves of SE SNe, some authors have used analytical functions developed for SNe Ia (e.g. Taddia et al. 2018b, 2019; Barbarino et al. 2021). In this work, in order not to assume heuristic models, we perform LOESS non-parametric regression (Cleveland et al. 1992). For this purpose we use the Automated Loess Regression (ALR) code⁵ (Rodríguez et al. 2019), which performs LOESS regressions to the input photometry, taking into account observed and intrinsic errors, along with the presence of possible outliers. Figure 1 shows, as an example, the ALR fit applied to the B -band photometry of SN I Ib 1996cb (Qiu et al. 1999).

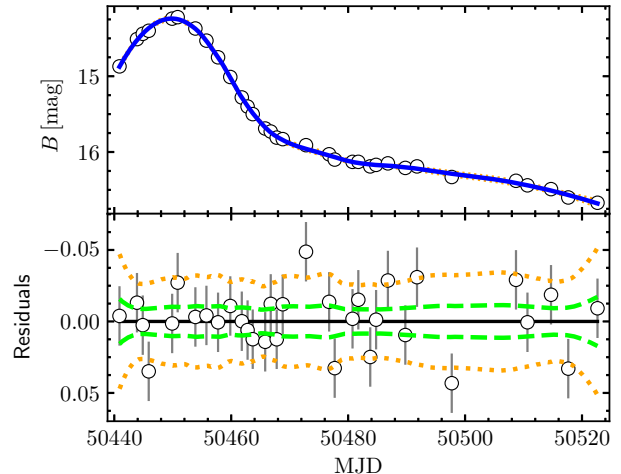


Figure 1. Top panel: B -band light curve of SN 1996cb, where the blue line is the ALR fit. Bottom panel: fit residuals, where dashed and dotted lines are the $\pm 1\sigma$ and $\pm 3\sigma$ limits, respectively. Error bars are 1σ errors.

3.3. Host galaxy distance moduli

Translating the observed light curve fluxes to luminosities naturally requires host-galaxy distances. We estimate host-galaxy distance moduli (μ) proceeding in the same way as in Rodríguez et al. (2021). Here we briefly summarize the general procedure.

We collect Cepheids period-luminosity distances (μ_{CPL}) and Tip of the Red Giant Branch distances (μ_{TRGB}) from the literature, along with Tully-Fisher distances (μ_{TF}) from the Extragalactic Distance Database⁶ (EDD, Tully et al. 2009). Then, we adopt the weighted average of μ_{CPL} , μ_{TRGB} , and μ_{TF} as μ and the weighted average error as the distance uncertainty σ_{μ} . If μ_{CPL} and μ_{TRGB} are not available, then we include distances calculated from recessional redshifts (μ_z) assuming a local Hubble-Lemaître constant (H_0) of $74.03 \pm 1.42 \text{ km s}^{-1} \text{ Mpc}^{-1}$ (Riess et al. 2019), $\Omega_m = 0.27$, $\Omega_{\Lambda} = 0.73$, and a velocity dispersion of 382 km s^{-1} (Wang et al. 2006) to account for the effect of peculiar velocities over μ_z . We also include distances computed with distance-velocity calculators based on smoothed velocity fields (μ_{SVF}) given by Shaya et al. (2017) and Graziani et al. (2019).⁷ We then adopt the weighted average of μ_{TF} , μ_z , and μ_{SVF} as μ and the weighted average error as σ_{μ} . In the case of NGC 3938 (the host of SN 2017ein) we include the distance modulus reported in Rodríguez et al. (2019) for SN II 2005ay, which also exploded in NGC 3938.

⁴ The equation in this form assumes that the initial heat in the ejecta, deposited by the SN shock, is negligible compared to the energy deposited by radioactive decay.

⁵ <https://github.com/olrodrig/ALR>

⁶ <http://edd.ifa.hawaii.edu/>

⁷ These calculators are available on the EDD website and described in Kourkchi et al. (2020).

All of the collected and final adopted distances are reported in Appendix Table F2. The mean μ uncertainty is 0.13 mag.

3.4. Explosion epochs

The estimation of ^{56}Ni masses requires the knowledge of the explosion epochs t_{expl} . The value of t_{expl} can be estimated as the midpoint time (t_{midpoint}) between the last non-detection ($t_{\text{non-det}}$) and the first SN detection (t_{detect}) epochs (e.g. Taddia et al. 2015). This method is useful when $t_{\text{non-det}}$ is a few days before t_{detect} , otherwise other methods are necessary to improve the estimation of t_{expl} . An alternative technique to calculate t_{expl} is by using the date of the peak of the x -band light curve, t_x^{peak} , where x represents any photometric filter.⁸ In this method, the quantity $t_x^{\text{peak}} - t_{\text{expl}}$ for each SN subtype is assumed to be a constant, whose value is determined with a sample of SNe with well-constrained explosion epochs (e.g. Taddia et al. 2018b). However, for SNe Ic, Taddia et al. (2019) and Barbarino et al. (2021) found a correlation between the increase in magnitude during the 10 d before the peak and the decrease in magnitude 15 d after the peak ($\Delta m_{15}(x)$, the decline rate). We therefore expect that, at least for SNe Ic, $t_x^{\text{peak}} - t_{\text{expl}}$ is not constant but varies with $\Delta m_{15}(x)$. Indeed, as we show in this section, for SNe Ib and Ic there is a correlation between both quantities for the V -band. This correlation provides a method to estimate explosion epochs relying not only on t_V^{peak} but also on $\Delta m_{15}(V)$.

We use our ALR light-curve fits (Section 3.2) to compute t_x^{peak} and $\Delta m_{15}(x)$ for the various optical bands, which are listed in Table F3 and Table F4, respectively. The $t_{\text{non-det}}$ and t_{detect} values are collected in Table F5.

To estimate t_{expl} , we use the V -band as a fiducial filter and proceed as follows. First, we calibrate the correlation between $t_V^{\text{peak}} - t_{\text{expl}}$ and $\Delta m_{15}(V)$ using SNe with $t_{\text{detect}} - t_{\text{non-det}}$ lower than 8 d and adopting t_{midpoint} as a first approximation for t_{expl} . Next, we use these correlations along with t_V^{peak} and $\Delta m_{15}(V)$ to estimate a second approximation for explosion epochs, $t_{\text{expl}}^{\text{peak}}$. Then, to include the constraint that the explosion epoch cannot be longer (shorter) than t_{detect} ($t_{\text{non-det}}$), for each SN we randomly generate 10^6 values from the normal distribution $\mathcal{N}(t_{\text{expl}}^{\text{peak}}, \sigma_{t_{\text{expl}}^{\text{peak}}})$ and select those values between $t_{\text{non-det}}$ and t_{detect} . Finally, we adopt the average of the selected values as our best estimate of t_{expl} . The detailed process used to compute our best estimates for t_V^{peak} , $\Delta m_{15}(V)$, and t_{expl} is presented below.

⁸ If the peak related to the shock cooling is observed, then t_x^{peak} is the date of the second peak.

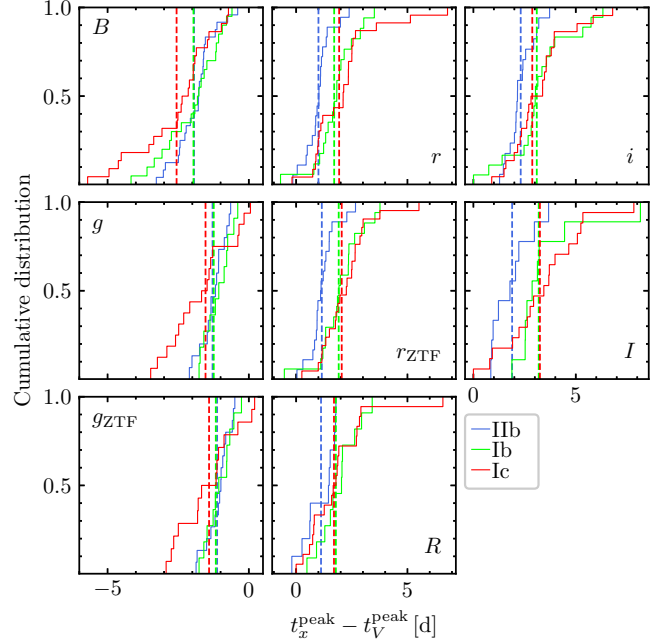


Figure 2. Cumulative distributions for the $t_x^{\text{peak}} - t_V^{\text{peak}}$ values. Dashed lines indicate mean values.

3.4.1. Peak epochs

Figure 2 shows the cumulative distribution functions (CDFs) for the $t_x^{\text{peak}} - t_V^{\text{peak}}$ values, while Table 1 summarises their average (ξ_x), $\sigma_{0,x}$, and $\hat{\sigma}$ values. We see that t_x^{peak} tends to increase as the x -band effective wavelength increases, which was previously reported by Taddia et al. (2015, 2018b). The reported ξ_x values are such that $t_x^{\text{peak}} = t_V^{\text{peak}} + \xi_x$, so each t_x^{peak} measurement provides an independent estimate of t_V^{peak} . For each SN, we combine its t_V^{peak} estimates into the single observable

$$\langle t_V^{\text{peak}} \rangle = \langle t_x^{\text{peak}} - \xi_x \rangle, \quad (13)$$

where angle brackets denote a weighted average with weights $w_x = 1/(\sigma_{t_x^{\text{peak}}}^2 + \sigma_{0,x}^2)$. The $\langle t_V^{\text{peak}} \rangle$ values and their weighted-average errors are listed in Column 11 of Table F3. Given that $\langle t_V^{\text{peak}} \rangle$ is our best estimate of t_V^{peak} , we adopt it as the final t_V^{peak} .

We estimate $t_V^{\text{peak}} - t_{\text{expl}}$ for SNe with $t_{\text{non-det}}$ up to eight days before t_{detect} , where we adopt $t_{\text{expl}} = t_{\text{midpoint}}$. The right-hand panel of Figure 3 shows the histograms for the $t_V^{\text{peak}} - t_{\text{expl}}$ values of SNe IIb, Ib, and Ic. Those distributions have mean ($\hat{\sigma}$) values of 19.1 (3.5), 15.8 (3.5), and 13.9 (5.3) d, respectively. This is consistent with the picture that the peak time of SNe Ic is on average earlier than that of SNe IIb and Ib (e.g. Valenti et al. 2011; Taddia et al. 2015; Prentice et al. 2016).

Table 1. Average $t_x^{\text{peak}} - t_V^{\text{peak}}$ values

x	SNe IIb				SNe Ib				SNe Ic			
	ξ_x (d)	$\sigma_{0,x}$ (d)	$\hat{\sigma}$ (d)	N	ξ_x (d)	$\sigma_{0,x}$ (d)	$\hat{\sigma}$ (d)	N	ξ_x (d)	$\sigma_{0,x}$ (d)	$\hat{\sigma}$ (d)	N
B	-1.9	0.6	0.7	24	-2.0	0.8	1.0	20	-2.6	1.2	1.4	22
g	-1.3	0.0	0.5	15	-1.2	0.4	0.5	11	-1.5	0.9	1.1	16
$gZTF$	-1.1	0.0	0.4	15	-1.2	0.3	0.5	11	-1.4	0.8	1.0	14
r	1.0	0.0	0.6	18	1.7	0.7	1.0	17	1.9	1.0	1.5	23
$rZTF$	1.1	0.0	0.6	18	1.9	0.8	1.0	17	2.0	0.6	1.1	21
R	1.1	0.6	0.7	10	1.8	0.7	0.9	11	1.7	0.9	1.5	18
i	2.3	0.6	0.7	17	3.1	1.4	1.6	18	2.9	0.8	1.4	22
I	1.9	0.9	1.0	9	3.2	0.0	1.9	9	3.2	1.6	2.0	17

NOTE—For $x = V$, $\xi_x = \sigma_{0,x} = 0$.

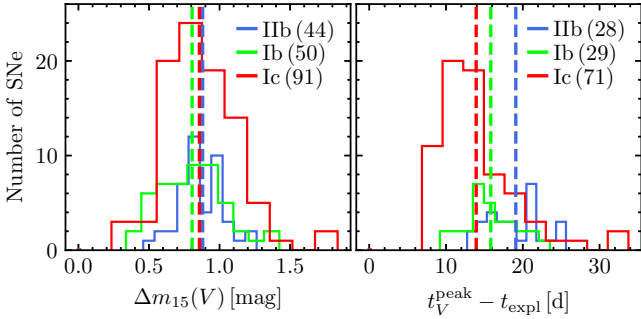


Figure 3. Histograms of $\Delta m_{15}(V)$ and $t_V^{\text{peak}} - t_{\text{expl}}$. Dashed lines indicate mean values.

3.4.2. Decline rates

Figure 4 shows $\Delta m_{15}(V)$ against $\Delta m_{15}(x)$ for optical bands. To describe the correlation between both quantities, we adopt a linear fit

$$\Delta m_{15}(V) = a_x + b_x \Delta m_{15}(x), \quad (14)$$

where a_x , b_x , $\sigma_{0,x}$ (calculated with equation 9) and $\hat{\sigma}$ values are collected in Table 2. Similar to $\langle t_V^{\text{peak}} \rangle$, for each SN we compute the weighted average of the $\Delta m_{15}(V)$ values obtained from different bands, i.e.,

$$\langle \Delta m_{15}(V) \rangle = \langle a_x + b_x \Delta m_{15}(x) \rangle, \quad (15)$$

with weights $w_x = 1/(b_x^2 \sigma_{\Delta m_{15}(x)}^2 + \sigma_{0,x}^2)$. The $\langle \Delta m_{15}(V) \rangle$ values and their weighted-mean errors are summarized in Column 11 of Table F4. Similar to $\langle t_V^{\text{peak}} \rangle$, we adopt $\langle \Delta m_{15}(V) \rangle$ as the final $\Delta m_{15}(V)$.

The left-hand panel of Figure 3 shows the histograms for the $\Delta m_{15}(V)$ estimates. The distributions for SNe IIb, Ib, and Ic have mean ($\hat{\sigma}$) values of 0.88 (0.16), 0.81 (0.24), and 0.86 (0.27) mag, respectively. Given

the apparent similarity between the distributions, we use the k -sample Anderson-Darling (AD) test (e.g. Scholz & Stephens 1987) to test whether the $\Delta m_{15}(V)$ samples of SNe IIb, Ib, and Ic are drawn from a common unspecified distribution (the null hypothesis). We obtain a standardized test statistics (T_{AD}) of 1.87 with an AD p -value (p_{AD}) of 0.05, meaning that the null hypothesis cannot be rejected at the 5% significance level. This is consistent with the study by Taddia et al. (2015), which found similar $\Delta m_{15}(r/R)$ and $\Delta m_{15}(g)$ distributions for SNe Ib and Ic.

3.4.3. Peak epoch versus decline rate

Figure 5 shows $t_V^{\text{peak}} - t_{\text{expl}}$ as a function of $\Delta m_{15}(V)$ for SNe with $t_{\text{detect}} - t_{\text{non-det}} < 8$ d, for which we adopt $t_{\text{expl}} = t_{\text{midpoint}}$. For SNe IIb we find that $t_V^{\text{peak}} - t_{\text{expl}}$ is consistent with a constant value, so we adopt $t_V^{\text{peak}} - t_{\text{expl}} = 19.1 \pm 3.5$ d. On the other hand, for SNe Ib and Ic we find a dependence of $t_V^{\text{peak}} - t_{\text{expl}}$ on $\Delta m_{15}(V)$, which we express as

$$t_V^{\text{peak}} - t_{\text{expl}} [\text{d}] = 21.8 - 7.3 \Delta m_{15}(V) \quad (16)$$

($\hat{\sigma} = 3.1$ d) for SNe Ib, and

$$t_V^{\text{peak}} - t_{\text{expl}} [\text{d}] = 3.0 + \frac{9.4}{\Delta m_{15}(V)} - \frac{0.6}{\Delta m_{15}(V)^2} \quad (17)$$

($\hat{\sigma} = 2.7$ d) for SNe Ic.

We use these $t_V^{\text{peak}} - t_{\text{expl}}$ calibrations to convert t_V^{peak} into $t_{\text{expl}}^{\text{peak}}$, which are listed along with their errors in Column 5 of Table F5. For SNe Ic 2006nx, 2013F, 2013dk, 2014ft, and 2021bm, which do not have $\Delta m_{15}(V)$ estimates, we adopt $t_V^{\text{peak}} - t_{\text{expl}} = 13.9 \pm 5.3$ d (the mean value of the distribution).

To evaluate whether the $t_V^{\text{peak}} - t_{\text{expl}}$ calibrations provide reasonable values for explosion epochs, in Figure 6 we show differences between $t_{\text{expl}}^{\text{peak}}$ and t_{detect} for

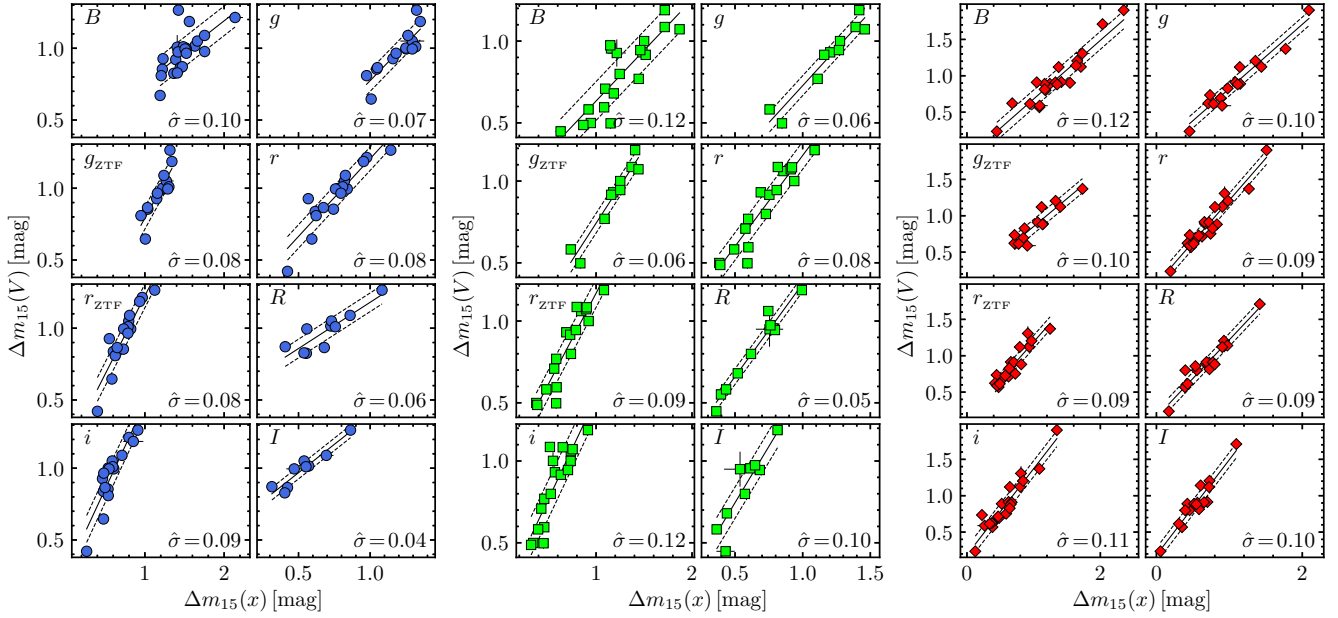


Figure 4. $\Delta m_{15}(V)$ as a function of $\Delta m_{15}(x)$ for SNe IIB (blue circles), Ib (green squares), and Ic (red diamonds). Solid lines are linear fits to the data, and dashed lines are the $\pm 1 \hat{\sigma}$ limits around the fits. Error bars indicate $\pm 1 \sigma$ errors.

Table 2. Parameters of the correlation between $\Delta m_{15}(V)$ and $\Delta m_{15}(x)$

x	SNe IIB					SNe Ib					SNe Ic				
	a_x	b_x	$\sigma_{0,x}$	$\hat{\sigma}$	N	a_x	b_x	$\sigma_{0,x}$	$\hat{\sigma}$	N	a_x	b_x	$\sigma_{0,x}$	$\hat{\sigma}$	N
B	0.33	0.43	0.10	0.10	23	0.01	0.62	0.11	0.12	20	-0.12	0.81	0.12	0.12	21
g	-0.25	1.02	0.07	0.07	14	-0.18	0.91	0.05	0.06	10	-0.06	0.88	0.07	0.10	15
g_{ZTF}	-0.21	1.00	0.06	0.08	14	-0.17	0.91	0.04	0.06	10	0.09	0.77	0.07	0.10	13
r	0.12	1.08	0.07	0.08	17	0.04	1.11	0.08	0.08	17	0.06	1.15	0.08	0.10	22
r_{ZTF}	0.14	1.08	0.07	0.08	17	0.05	1.12	0.07	0.09	17	0.15	1.04	0.06	0.09	20
R	0.54	0.64	0.06	0.07	10	0.09	1.14	0.04	0.05	11	0.15	1.06	0.07	0.09	17
i	0.26	1.19	0.08	0.09	17	0.14	1.25	0.11	0.12	18	0.19	1.19	0.09	0.11	21
I	0.57	0.79	0.03	0.04	9	0.06	1.38	0.04	0.10	9	0.18	1.31	0.10	0.10	16

NOTE—For $x = V$, $a_x = \sigma_{0,x} = 0$ and $b_x = 1.0$.

SNe 1998bw, 2006aj, 2008D, and 2016gkg. For these SNe, t_{detect} corresponds to the shock-breakout detection (for SN 2016gkg), the first γ -ray detection (for SN 1998bw), or the first X-ray detection (for SNe 2006aj and 2008D), thus t_{detect} is the best estimate for explosion epoch. In Figure 6 we see that the $t_{\text{expl}}^{\text{peak}} - t_{\text{detect}}$ value of each SN is consistent with zero within $1 \sigma_{t_{\text{expl}}^{\text{peak}}}$. In addition, the average ($\hat{\sigma}$) of the $t_{\text{expl}}^{\text{peak}} - t_{\text{detect}}$ estimates is of 0.7 d (1.7 d), so $t_{\text{expl}}^{\text{peak}}$ is statistically consistent with t_{detect} to $1 \hat{\sigma} / \sqrt{N}$. Therefore, even we do not know the exact explosion epoch for almost all SNe in our sample, we at least do not find systematic differences be-

tween our $t_{\text{expl}}^{\text{peak}}$ estimates and the explosion epochs for those SNe with well-known t_{expl} .

To include the constraint provided by $t_{\text{non-det}}$ and t_{detect} on the explosion epoch, for each SN we randomly generate 10^6 values from the normal distribution $\mathcal{N}(t_{\text{expl}}^{\text{peak}}, \sigma_{t_{\text{expl}}^{\text{peak}}})$. We then select the values between $t_{\text{non-det}}$ and t_{detect} , and compute the mean and $\hat{\sigma}$ value, which we adopt as the final t_{expl} and its error, respectively. Those estimates are reported in Column 6 of Table F5. The mean t_{expl} error for our SN sample is 1.4 d.

3.5. Host galaxy reddenings

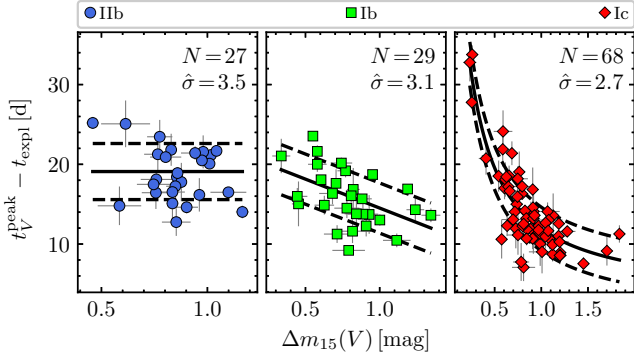


Figure 5. $t_V^{\text{peak}} - t_{\text{expl}}$ versus $\Delta m_{15}(V)$. Solid lines are the best fits to the data, while dashed lines are the $\pm 1 \hat{\sigma}$ limits. Error bars are 68% errors.

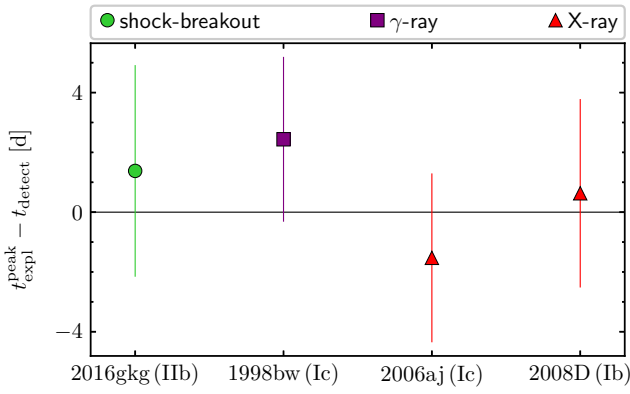


Figure 6. Differences between $t_{\text{expl}}^{\text{peak}}$ and the first detection epoch for SNe 1998bw (γ -ray detection), 2006aj and 2008D (X-ray detection), and 2016gkg (shock-breakout detection). Error bars are $1 \sigma_{t_{\text{expl}}^{\text{peak}}}$ errors.

To obtain luminosities, light curves must be corrected for the effects of dust extinction and reddening. In this work, we use color curves to compute E_{B-V} , and employ those estimates to calibrate the relation between E_{B-V} and EW_{NaID} for SE SNe.

3.5.1. Color curve shapes

For a given SN, we model its $c = x - y$ (where x and y represent any two photometric bands) color curve (corrected for MW reddening and K -correction, see Appendix B) as

$$c(t) = \delta_c + \Psi_c(t - t_y^{\text{peak}}), \quad (18)$$

where δ_c is the vertical intercept of the color curve, and Ψ_c is a polynomial representing the dependence of c on $t - t_y^{\text{peak}}$ (i.e. the shape of the color curve). Under the assumption that all SNe of a given subtype have the same intrinsic color curve given by

$$c_0(t) = \delta_{0,c} + \Psi_{0,c}(t - t_y^{\text{peak}}), \quad (19)$$

then $\Psi_c = \Psi_{0,c}$ and

$$\delta_c = \delta_{0,c} + E_{B-V} R_c. \quad (20)$$

Here, $R_c = E_{x-y}/E_{B-V}$, which depends on the R_V value characterising a host galaxy's extinction along the SN line of sight. The δ_c value of each color is therefore an indicator of E_{B-V} . In this work we use the independent colors $B-V$, $g-i$, $V-r$, $V-R$, $V-i$, $V-I$, and $(g-r)_{\text{ZTF}}$.

To measure δ_c for each SN in a sample of size N along with the parameters of $\Psi_{0,c}$, we minimize

$$s^2 = \sum_j^N \sum_k^{M_j > 1} [Y_{j,k} - \delta_{Y,j} - \Psi_{0,Y}(X_{j,k})]^2. \quad (21)$$

Here, $Y = c$, $X = t - t_y^{\text{peak}}$, M_j is the number of observations for the j -th SN, while the polynomial order of $\Psi_{0,Y}$ is determined with the BIC. To estimate δ_c we use data in the time range between t_y^{peak} and $t_y^{\text{peak}} + t_c^{\text{max}}$, where t_c^{max} is the time where the color curves reach their maximum value. We choose this time interval because color curves are found to be similar at such epochs (e.g. Stritzinger et al. 2018a), and because $\Psi_{0,c}$ can then be represented by a low-order polynomial. For a given SN, the error on δ_c is

$$\sigma_{\delta_c} = \sqrt{\hat{\sigma}_c^2 + [\langle \dot{\Psi}_{0,c} \rangle \sigma_{t_y^{\text{peak}}}]^2}, \quad (22)$$

where $\hat{\sigma}_c$ is the $\hat{\sigma}$ dispersion of the $c - \delta_c$ values around $\Psi_{0,c}$, while $\langle \dot{\Psi}_{0,c} \rangle$ is the average of the time derivative of $\Psi_{0,c}$.

The top panel of Figure 7 shows the $V-i$ color curves of 23 SNe IIb in our sample, with $t - t_i^{\text{peak}}$ between zero and $t_{V-i}^{\text{max}} = 23.3$ d. The observed spread is due to the host galaxy reddenings of each SN and the intrinsic diversity of the $V-i$ color curves. The $\Psi_{0,V-i}$ curve and the δ_{V-i} values, obtained from the minimization of equation (21), are shown in the middle and bottom panel of Figure 7, respectively. We find that $\Psi_{0,V-i}$ is quadratic in $t - t_i^{\text{peak}}$ (solid line), where the $\hat{\sigma}$ value of 0.046 mag corresponds to the minimum error on $V-i$ induced by random errors and intrinsic differences.

For all the independent colors we find a quadratic dependence of $\Psi_{0,c}$ on $t - t_y^{\text{peak}}$, given by

$$\Psi_{0,c} = a_c \left(\frac{t - t_y^{\text{peak}}}{10 \text{ d}} \right) + b_c \left(\frac{t - t_y^{\text{peak}}}{10 \text{ d}} \right)^2. \quad (23)$$

The a_c , b_c , and t_c^{max} values for different colors and SN subtypes are listed in Table 3, while Figure 8 shows the $\Psi_{0,c}$ curves. The δ_c estimates are collected in F6.

Table 3. Color curve shape parameters

c	SNe IIb					SNe Ib					SNe Ic				
	a_c	b_c	$\hat{\sigma}_c$	t_c^{\max}	N	a_c	b_c	$\hat{\sigma}_c$	t_c^{\max}	N	a_c	b_c	$\hat{\sigma}_c$	t_c^{\max}	N
$B-V$	0.748	-0.199	0.068	18.8	30	0.701	-0.165	0.069	21.3	25	0.598	-0.170	0.083	17.6	39
$g-i$	0.821	-0.217	0.069	18.9	21	0.789	-0.212	0.069	18.6	19	0.786	-0.219	0.083	18.0	28
$V-r$	0.287	-0.075	0.039	19.1	23	0.234	-0.056	0.040	21.0	19	0.385	-0.121	0.046	15.9	30
$V-R$	0.395	-0.107	0.047	18.5	11	0.307	-0.071	0.043	21.6	12	0.332	-0.085	0.050	19.6	20
$V-i$	0.474	-0.101	0.046	23.5	23	0.466	-0.115	0.052	20.2	19	0.558	-0.151	0.055	18.5	30
$V-I$	0.539	-0.119	0.047	22.7	10	0.450	-0.086	0.054	26.2	10	0.547	-0.115	0.070	23.7	19
$(g-r)_{\text{ZTF}}$	0.590	-0.142	0.078	20.7	36	0.576	-0.145	0.066	19.9	37	0.711	-0.211	0.070	16.9	75

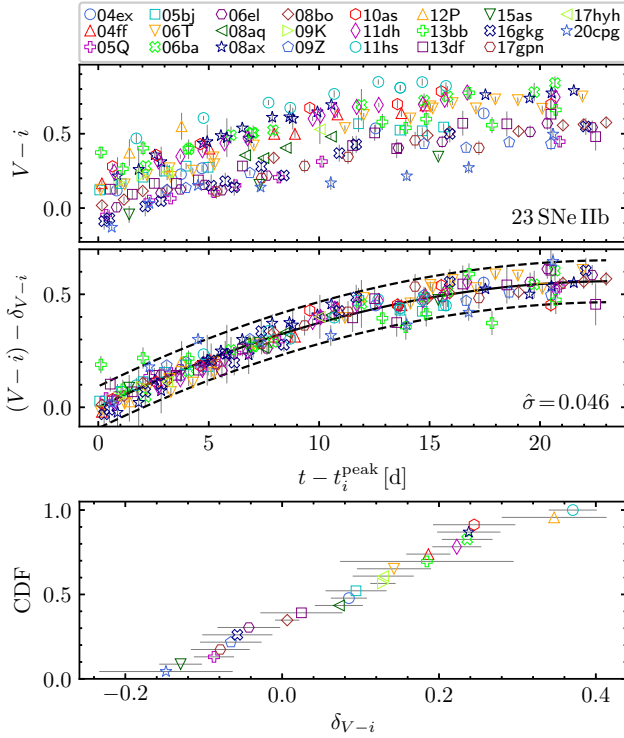


Figure 7. $V-i$ color curves of SNe IIb corrected for MW reddening and K -correction (top panel), and shifted by δ_{V-i} (middle panel). The solid line is a quadratic fit, corresponding to $\Psi_{0,V-i}$, while dashed lines indicate the $\pm 2\hat{\sigma}$ limits. Bottom panel: cumulative distribution for the δ_{V-i} values. Error bars are 1σ errors.

3.5.2. E_{B-V} and representative R_V values

For each SN subtype, using N SNe with δ_c values in more than one color, we can compute the $\delta_{0,c}$ values, the E_{B-V} estimates for each SN, and the representative host galaxy R_V maximizing equation (8), where the log-

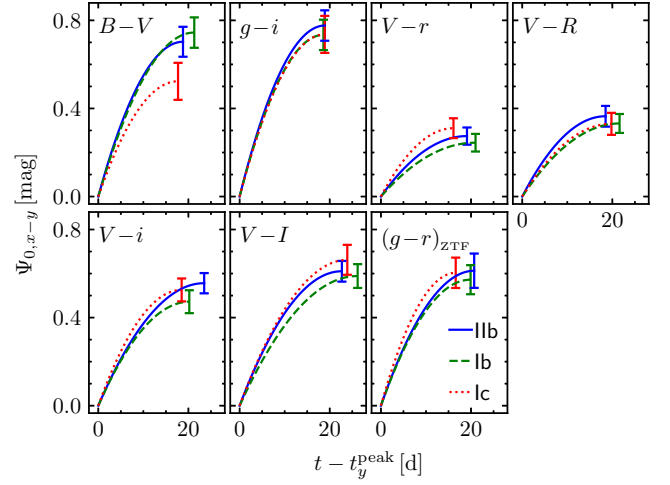


Figure 8. $\Psi_{0,c}$ curves for different colors of SNe IIb (blue solid lines), Ib (green dashed lines), and Ic (red dotted lines). Error bars indicate the $\pm 1\hat{\sigma}$ limits around the curves.

likelihood of equation (20) is given by

$$\ln \mathcal{L} = -\frac{1}{2} \sum_{j=1}^N \sum_c^{\{c\}_j} \left[\ln(\sigma_{\delta_{c,j}}^2 + \sigma_{0,c}^2) + \frac{[\delta_{c,j} - \tilde{\delta}_{0,c} - \tilde{E}_{B-V,j} R_c(R_V)]^2}{\sigma_{\delta_{c,j}}^2 + \sigma_{0,c}^2} \right]. \quad (24)$$

Here, $\{c\}_j$ are the available colors for the j -th SN, and $\sigma_{0,c}$ is the uncertainty not accounted for in the error on $\delta_{c,j}$. In the last equation we use \tilde{E}_{B-V} and $\tilde{\delta}_{0,c}$ instead of E_{B-V} and $\delta_{0,c}$ because there is a degeneracy between both parameters. Indeed, we can express E_{B-V} and $\delta_{0,c}$ as

$$E_{B-V} = \tilde{E}_{B-V} + ZP_{E_{B-V}} \quad (25)$$

and

$$\delta_{0,c} = \tilde{\delta}_{0,c} - R_c ZP_{E_{B-V}} \quad (26)$$

such that $\delta_{0,c} + E_{B-V}R_c = \tilde{\delta}_{0,c} + \tilde{E}_{B-V}R_c$. The constant $ZP_{E_{B-V}}$ corresponds to the zero-point for the reddening scale.

Table 4 collects $\tilde{\delta}_{0,c}$, $\sigma_{0,c}$, and the representative R_V values obtained from the maximization of equation (8). The \tilde{E}_{B-V} values and their weighted mean errors, given by

$$\sigma_{\tilde{E}_{B-V}} = \left[\sum_c R_c^2 / (\sigma_{\delta_c}^2 + \sigma_{0,c}^2) \right]^{-1/2}, \quad (27)$$

are listed in Column 4 of Table F7. For those SNe with only one δ_c measurement, we use $\tilde{E}_{B-V} = (\delta_c - \tilde{\delta}_{0,c})/R_c$.

For SNe IIb, Ib, and Ic we find R_V ($\pm 1\sigma$ error) values of 2.6 ± 0.4 , 2.7 ± 0.5 , and 3.8 ± 0.4 , respectively. Although SNe Ic seem to have a larger R_V value compared to SNe IIb and Ib (as previously found by Stritzinger et al. 2018a), this is only at the $\pm 2.1\sigma$ level, and we cannot exclude on this basis a single R_V for all three types of SNe.

To estimate $ZP_{E_{B-V}}$ in equation (25), we compare \tilde{E}_{B-V} against EW_{NaID} , which we use as a proxy for reddening. Column 3 of Table F7 lists the EW_{NaID} values for the SNe in our sample, which we compute using the procedure presented in Appendix D. We also include EW_{NaID} values calculated in the literature from high-resolution spectra. We focus our analysis on SNe with $EW_{\text{NaID}} < 1 \text{ \AA}$ since this observable becomes a poor tracer of reddening for larger values (e.g. Phillips et al. 2013), and with $\sigma_{EW_{\text{NaID}}} < 0.2 \text{ \AA}$ to minimize the induced scatter.

Figure 9 shows \tilde{E}_{B-V} against EW_{NaID} for each SN subtype. We express the dependence of \tilde{E}_{B-V} on EW_{NaID} as

$$\tilde{E}_{B-V} = a + bEW_{\text{NaID}}[\text{\AA}], \quad (28)$$

where the values of a , b , σ_0 (computed maximizing equation 8), and of $\hat{\sigma}$ are reported in Table 5. To evaluate the linear correlations, we calculate the Pearson correlation coefficient (r_P) and the corresponding null-hypothesis probability p -value (p_P). For SNe IIb, Ib, and Ic we obtain moderate/strong correlations, with r_P (p_P) values of 0.52 (0.05), 0.57 (0.03), and 0.75 (< 0.01), respectively. If we assume that E_{B-V} is zero for $EW_{\text{NaID}} = 0$, then from equations (25) and (28) we obtain $ZP_{E_{B-V}} = -a$. Therefore we adopt $-a$ and $\hat{\sigma}$ as $ZP_{E_{B-V}}$ and its error, respectively. The E_{B-V} values computed with equation (25), which we call E_{B-V}^{CC} (CC is for color curves), and their errors given by

$$\sigma_{E_{B-V}^{\text{CC}}} = \sqrt{\sigma_{\tilde{E}_{B-V}}^2 + \sigma_{ZP_{E_{B-V}}}^2} \quad (29)$$

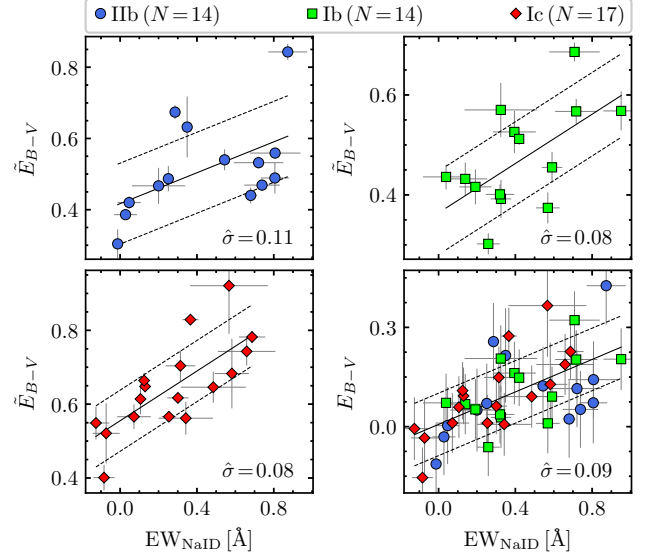


Figure 9. \tilde{E}_{B-V} versus EW_{NaID} for SNe IIb (upper left-hand panel), Ib (upper right-hand panel), and Ic (bottom left-hand panel). Bottom right-hand panel: host galaxy reddening versus EW_{NaID} . Solid and dashed lines are linear fits and $1\hat{\sigma}$ limits, respectively. Error bars indicate $\pm 1\sigma$ errors.

are reported in Column 5 of Table F7.

3.5.3. Relation between E_{B-V} and NaID EW

We note that although the b estimates differ somewhat among the three SE SN types, they are consistent within the errors, i.e. the relation between host-galaxy reddening and EW_{NaID} does not appear to depend on SN subtype. Based on this, we use the E_{B-V}^{CC} and EW_{NaID} values of SNe IIb, Ib, and Ic (bottom right-hand panel of Figure 9) to infer the relation between host galaxy reddening and EW_{NaID} . We find a linear fit

$$E_{B-V} = 0.007(\pm 0.024) + 0.246(\pm 0.054)EW_{\text{NaID}}[\text{\AA}], \quad (30)$$

with $\hat{\sigma} = 0.094$ mag, $r_P = 0.60$, and $p_P < 0.01$.

Using equation (30) we compute host galaxy reddenings for the SNe with EW_{NaID} measurements (E_{B-V}^{NaID}), which are listed in Column 6 of Table F7. We adopt the weighted average of E_{B-V}^{CC} and E_{B-V}^{NaID} as the final E_{B-V} , which are collected in Column 7 of Table F7. The typical E_{B-V} error is 0.108 mag.

3.5.4. Accuracy of the host galaxy reddening scale

As expected, our E_{B-V} estimates are not very precise due to the photometric and spectroscopic diversity of SE SNe. On the other hand, the accuracy of the reddening scale depends on the similarity between the SN sample that we use to calculate $ZP_{E_{B-V}}$ and a complete sample. To evaluate this accuracy, we compare the SN IIb, Ib, and Ic samples used to compute

Table 4. Results of the posterior probability maximization for δ_c

c	SNe IIb ($N = 27$)			SNe Ib ($N = 30$)			SNe Ic ($N = 44$)		
	$R_V = 2.6 \pm 0.4$			$R_V = 2.7 \pm 0.5$			$R_V = 3.8 \pm 0.4$		
	$\tilde{\delta}_{0,c}$	$\sigma_{0,c}$	$R_c(R_V)$	$\tilde{\delta}_{0,c}$	$\sigma_{0,c}$	$R_c(R_V)$	$\tilde{\delta}_{0,c}$	$\sigma_{0,c}$	$R_c(R_V)$
$B-V$	0.0	0.032	1.00	0.0	0.115	1.00	0.0	0.177	1.00
$g-i$	-0.525	0.0	1.69	-0.447	0.0	1.71	-1.162	0.0	1.93
$V-r$	-0.132	0.020	0.46	-0.130	0.047	0.46	-0.298	0.048	0.47
$V-R$	-0.077	0.042	0.61	-0.064	0.027	0.61	-0.299	0.035	0.66
$V-i$	-0.466	0.0	1.00	-0.420	0.024	1.02	-0.985	0.0	1.24
$V-I$	-0.215	0.050	1.18	-0.136	0.0	1.21	-0.741	0.0	1.54
$(g-r)_{\text{ZTF}}$	-0.226	0.049	1.17	-0.236	0.037	1.17	-0.604	0.087	1.20

Table 5. \tilde{E}_{B-V} versus EW_{NaID} parameters

Type	N	a	b	σ_0	$\hat{\sigma}$	b^a
IIb	14	0.417(59)	0.217(108)	0.107	0.114	0.206
Ib	14	0.364(51)	0.247(101)	0.074	0.084	0.229
Ic	17	0.555(30)	0.336(92)	0.057	0.083	0.376

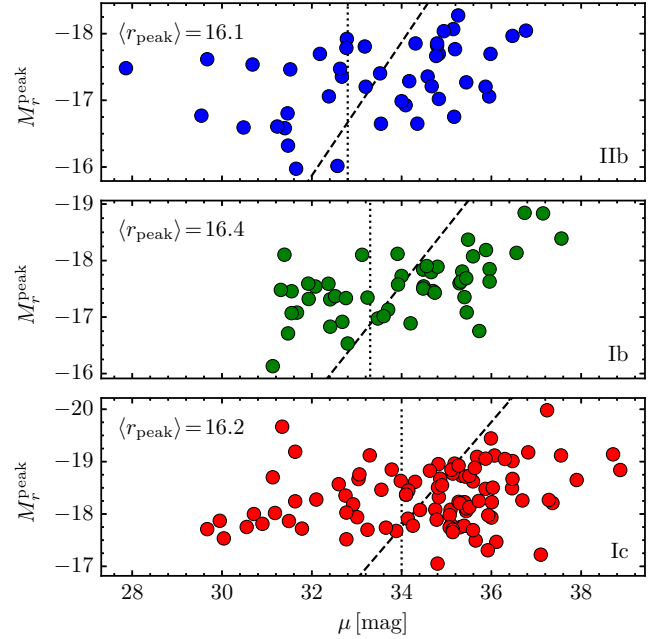
NOTE—Numbers in parentheses are 1σ errors in units of 0.001.

^aAssuming $R_V = 3.1$.

$ZP_{E_{B-V}}$ with volume-limited (VL) samples, which we use as approximations for complete samples. For this comparison, we use absolute r -band magnitudes at peak (M_r^{peak}). For 22 (6) SNe without photometry in the r (r and R) band, we measure M_r^{peak} using R (V) band photometry and the mean $r-R$ ($V-r$) color at peak of 0.13 ± 0.06 (0.04 ± 0.07). The M_r^{peak} values are listed in Table F8.

Figure 10 shows M_r^{peak} against μ , where the dashed lines indicate the average apparent r -band magnitude at peak, $\langle r_{\text{peak}} \rangle$. For SNe IIb and Ib it is evident that there is a reduction in the number of objects as we move to greater r_{peak} values (right-hand side of the dashed line), which is a consequence of the Malmquist selection bias. To minimize this bias, we select VL samples with $\mu \leq \mu_{\text{VL}}$, with μ_{VL} values of 32.8 for SNe IIb, 33.3 for Ib, and 34.0 for SNe Ic. By using these μ_{VL} values, the selection bias affecting the VL samples becomes relevant only in the small region with $r_{\text{peak}} > \langle r_{\text{peak}} \rangle$.

Figure 11 shows the cumulative distributions for the M_r^{peak} values in the VL samples and those of the SNe used to compute $ZP_{E_{B-V}}$. The similarity of the distributions for each SN subtype is evident, with $p_{\text{AD}} > 0.92$.

**Figure 10.** M_r^{peak} against μ for SNe IIb, Ib, and Ic. Dashed lines correspond to $r_{\text{peak}} = \langle r_{\text{peak}} \rangle$, and dotted lines are the limits for the volume-limited samples.

Therefore we can expect that our E_{B-V} estimates are not, on average, under- or overestimated.

3.5.5. Host galaxy reddening distribution

Figure 12 shows the histograms of E_{B-V} for SNe IIb, Ib, and Ic, where for comparison we also include the SNe II from the sample of Rodríguez et al. (2021). For 26 SE SNe we obtain negative E_{B-V} values, which range between -0.005 and -0.169 mag with a mean of -0.06 mag, and are consistent with zero to within $-1.4\sigma_{E_{B-V}}$. Although negative reddenings have no physical meaning, such values reflect the uncertainty of our methodology to measure E_{B-V} , which is due mainly to the diversity of SE SNe. Indeed, negative E_{B-V} val-

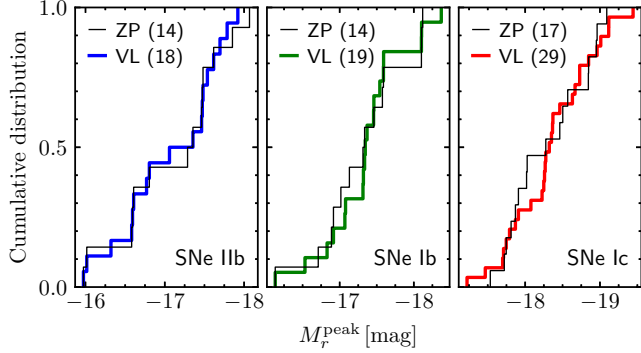


Figure 11. Cumulative distributions for the M_r^{peak} values in the volume-limited samples (thick lines) and the samples used to compute the zero-points of the reddening scales (thin lines). Numbers in parentheses are the sample sizes.

ues are inferred for SNe in our sample with the bluest intrinsic colors. Similarly, our methodology overestimates E_{B-V} for the SNe with the reddest intrinsic colors. For SNe with negative reddenings, a E_{B-V} of zero is a more appropriate value. However, correcting only the lower boundary of the E_{B-V} distribution by replacing negative reddenings by zero would bias the sample, producing an overestimation of the mean E_{B-V} , and therefore an overestimation of the mean ^{56}Ni masses of SE SNe. Given that we aim to infer accurate mean ^{56}Ni and iron yields of SE SNe, we perform the host galaxy reddening correction keeping the negative E_{B-V} values. For studies of single events, our reported luminosities and ^{56}Ni masses for SNe with negative E_{B-V} should be considered lower limits.

To identify extreme values in the distributions, we use the [Chauvenet \(1863\)](#) criterion. For SNe Ic we find that SNe 2005kl and 2013F have E_{B-V} values greater than the Chauvenet upper rejection limit ($E_{B-V} = 0.93$ mag), and hence we consider them outliers. The mean, $\hat{\sigma}$, skewness, and median values of the E_{B-V} distributions for SNe II, IIb, Ib, and Ic (after removing SNe 2005kl and 2013F) are listed in Table 6. Since the distributions are asymmetric (with positive skewness), we use the median rather than the mean as the representative value. We see that the median E_{B-V} tends to grow in the sequence of II–IIb–Ib–Ic subtypes.

Using the k -sample AD test to compare the E_{B-V} distributions of the {II,IIb}, {II,Ib}, {II,Ic}, {IIb,Ib}, {IIb,Ic}, and {Ib,Ic} samples, we obtain p_{AD} values of 0.07, 0.16, 0.02, 0.05, 0.03, and 0.36, respectively. In other words, the E_{B-V} distributions for SNe II and IIb are statistically similar, the distribution for SNe Ib is similar to those of SNe II, IIb, and Ic, while the distribution for SNe Ic and those for SNe II and SNe IIb

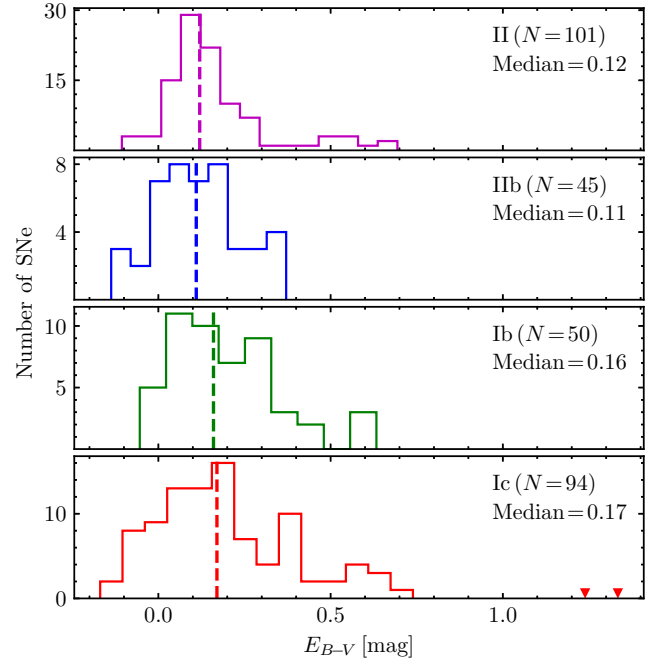


Figure 12. Histograms for the E_{B-V} values of the SNe IIb, Ib, and Ic in our sample, and of the SNe II in the sample of [Rodríguez et al. \(2021\)](#). Dashed lines indicate median values, while red triangles mark the locations of the outliers.

Table 6. Statistics of the E_{B-V} distributions

Type	N	Mean	$\hat{\sigma}$	Skewness	Median
II	101	0.16	0.15	1.53	0.12
IIb	45	0.12	0.13	0.14	0.11
Ib	50	0.19	0.16	0.96	0.16
Ic	94	0.20	0.20	0.65	0.17

are different (null hypothesis rejected at the 2–3% significance level). These findings remain unchanged if we adopt $R_V = 3.1$ for SE SNe. The difference between the E_{B-V} distributions for SNe IIb and Ic has been previously reported by [Stritzinger et al. \(2018a\)](#). For the E_{B-V} distributions of the {II,IIb,Ib} sample we find a $p_{\text{AD}} = 0.04$, which increases to 0.05 if we use $R_V = 3.1$. Therefore, it is still not clear-cut whether or not the E_{B-V} values for SNe II, IIb, and Ib are drawn from a common distribution.

3.5.6. Intrinsic color curves

The intrinsic color curves (given by equation 19) can be constructed using equations (23) and (26), along with the derived a_c , b_c , $\hat{\delta}_{0,c}$, R_c , and $\text{ZP}_{E_{B-V}}$ values. Figure 13 shows the intrinsic $B-V$ color curves for SE SNe,

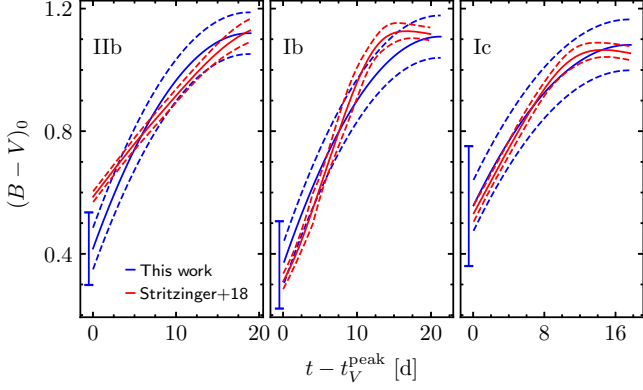


Figure 13. Intrinsic $B-V$ color curves (solid lines) estimated in this work (blue) and in Stritzinger et al. (2018a) (red). Dashed lines are $\pm 1\hat{\sigma}$ limits, while error bars represent the error on $(B-V)_0$ due to the intrinsic uncertainty and $ZP_{E_{B-V}}$ error.

along with those presented in Stritzinger et al. (2018a). We see that despite the evident differences in shape, they are consistent within their $1\hat{\sigma}$ limits. The $\hat{\sigma}$ scatter around the color curves of Stritzinger et al. (2018a) is 2–3 times lower than in our templates. We notice that the intrinsic color curves of Stritzinger et al. (2018a) were constructed with only 3 SNe per subtype, as opposed to the 25–39 SNe per subtype that we use to determine the shape of the $(B-V)_0$ curves. The figure also shows the error on $(B-V)_0$ due to the intrinsic uncertainty and $ZP_{E_{B-V}}$ error, which is ~ 2 times greater than the $\hat{\sigma}$ value. The latter means that the intrinsic $B-V$ color curves of SE SNe are more diverse than apparent from the templates of Stritzinger et al. (2018a).

3.6. Bolometric flux

Let f_λ be the SED and $f_{x_1 \leq \lambda \leq x_n}$ the integral of f_λ between $\bar{\lambda}_{x_1}$ and $\bar{\lambda}_{x_n}$. The bolometric flux can be expressed as

$$f_{\text{bol}} = f_{\lambda < B} + f_{B \leq \lambda \leq x_{\text{IR}}} + f_{\lambda > x_{\text{IR}}}. \quad (31)$$

Here, x_{IR} is the reddest available photometric IR band, while $f_{\lambda < B}$ and $f_{\lambda > x_{\text{IR}}}$ are the flux at wavelengths below $\bar{\lambda}_B$ and beyond $\bar{\lambda}_{x_{\text{IR}}}$, respectively.

3.6.1. Observed flux

Given measured photometry in filters $S = \{x_1, \dots, x_n\}$, a proxy for $f_{x_1 \leq \lambda \leq x_n}$ is the quantity

$$f_S = \frac{1}{2} \sum_{j=1}^{n-1} (\bar{\lambda}_{x_{j+1}} - \bar{\lambda}_{x_j}) (\bar{f}_{x_{j+1}} + \bar{f}_{x_j}) \quad (32)$$

(e.g. Lusk & Baron 2017). Here,

$$\bar{f}_x = 10^{-0.4(m_{x,0} - ZP_{\text{flux},x})} \quad (33)$$

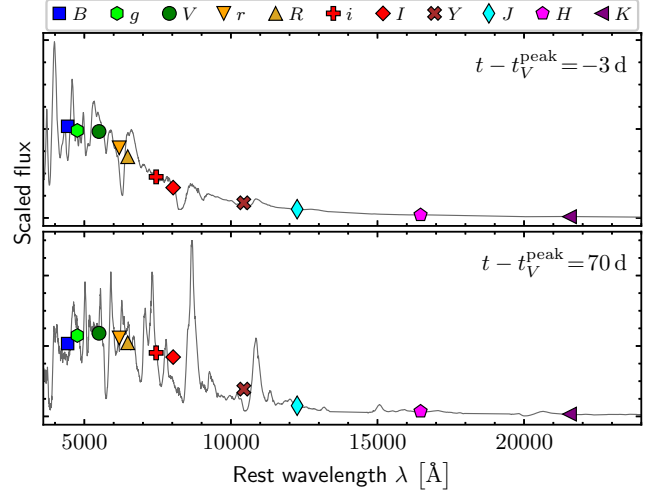


Figure 14. Optical/IR spectra of SN 2011dh at -3 (top panel) and 70 d (bottom panel) from t_V^{peak} . Colored symbols are the monochromatic fluxes estimated with the magnitudes computed from the spectra.

is the monochromatic flux (in $\text{ergs}^{-1} \text{cm}^{-2} \text{\AA}^{-1}$) associated with the intrinsic x -band magnitude $m_{x,0}$, and $ZP_{\text{flux},x}$ is a constant providing the conversion from magnitudes to monochromatic fluxes (listed in Table 14). To quantify the relative difference between $f_{x_1 \leq \lambda \leq x_n}$ and f_S , we define

$$\alpha_S = f_{x_1 \leq \lambda \leq x_n} / f_S. \quad (34)$$

To estimate α_S we assemble 34 observed optical/IR spectra of eight SE SNe, covering the λ range between 0.36 and $2.4 \mu\text{m}$. From those spectra, we compute synthetic magnitudes for optical $BgVrRiI$ and IR $YJHK$ bands (see Appendix A), which we convert to \bar{f}_x using equation (33). Figure 14 shows the optical/IR spectra of SN 2011dh at two different epochs and the $(\bar{\lambda}_x, \bar{f}_x)$ values for the aforementioned filters. We then calculate f_S (equation 32) and $f_{x_1 \leq \lambda \leq x_n}$ for different filter combinations.

The top panel of Figure 15 shows the α_S values for $S = BVrIJHK$. We see a dependence of α_S on $t - t_V^{\text{peak}}$, which we express as

$$\alpha_S = \delta_{0,\alpha_S} + \Psi_{0,\alpha_S}(t - t_V^{\text{peak}}), \quad (35)$$

with

$$\Psi_{0,\alpha_S}(t - t_V^{\text{peak}}) = b_S \frac{t - t_V^{\text{peak}}}{100 \text{ d}}. \quad (36)$$

Minimising equation (21) with $X = t - t_V^{\text{peak}}$ and $Y = \alpha_S$, we infer the δ_{α_S} estimates for each SN (bottom right panel) and Ψ_{0,α_S} (bottom left panel). We adopt the mean and $\hat{\sigma}$ of the δ_{α_S} estimates as δ_{0,α_S} and its error, respectively.

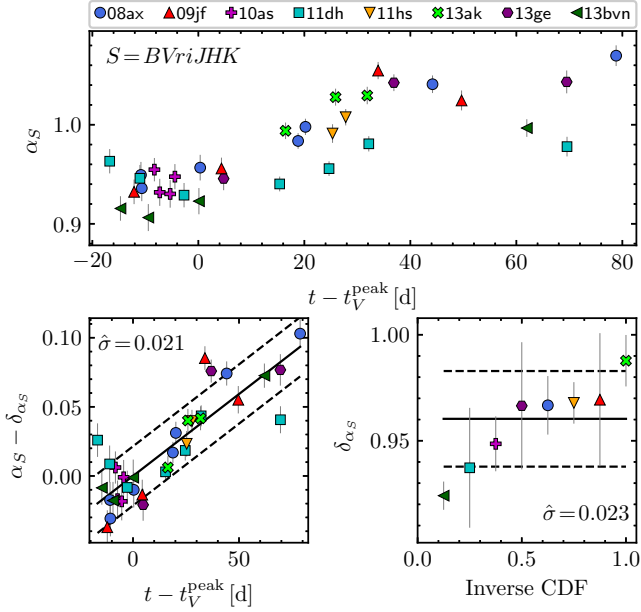


Figure 15. Top panel: α_S against $t - t_V^{\text{peak}}$ for $S = BVriJHK$. Bottom left panel: α_S values shifted by δ_{α_S} , where the solid line is a straight line fit corresponding to Ψ_{0,α_S} . Bottom right panel: inverse CDF for the δ_{α_S} values, where the solid line is the mean value. Dashed lines are $\pm 1\sigma$ limits, and error bars are 1σ errors.

Table 7. Parameters of the α_S calibrations

S	b_S	δ_{0,α_S}	$t - t_V^{\text{peak}}$ range (d)
<i>BVriJH</i>	0.124	0.960 ± 0.023	-17, 79
<i>BVriJHK</i>	0.119	0.960 ± 0.023	-17, 79
<i>BgVriJHK</i>	0.112	0.963 ± 0.023	-17, 79
<i>BgVriYJH</i>	0.058	0.988 ± 0.021	-17, 79
<i>BgVrRiLJH</i>	0.021	0.989 ± 0.016	-17, 79
<i>BVRiJHK</i>	0.0	0.990 ± 0.019	-17, 79
<i>BgVrRiIYJH</i>	0.0	1.004 ± 0.015	-17, 79
<i>BVrRiLJHK</i>	0.0	0.992 ± 0.018	-17, 79
<i>BgVrRiLJHK</i>	0.0	0.993 ± 0.016	-17, 79
<i>uB</i>	-0.484	1.247 ± 0.120	-17, 47
<i>UB</i>	-0.021	1.174 ± 0.118	-17, 271

Table 7 summarizes the parameters of the α_S calibrations for different sets of optical/IR filters, which are valid in the range $-17\text{d} < t - t_V^{\text{peak}} < 79\text{d}$. To avoid relying on extrapolations, for $t - t_V^{\text{peak}}$ greater than 79 d we adopt the α_S value evaluated at 79 d.

3.6.2. Unobserved flux at $\lambda < \bar{\lambda}_B$

To estimate $f_{\lambda < B}$, we use the intrinsic B -band magnitude (B_0) and the UV correction (UVC; Pritchard et al. 2014), defined as

$$\text{UVC} = -2.5 \log(f_{\lambda < B}) - B_0. \quad (37)$$

To calibrate UVC, we first compute $f_{\lambda < B}$ for 21 SE SNe with BV and UVOT u , $w1$, and $w2$ photometry. For those SNe, we express $f_{\lambda < B}$ as

$$f_{\lambda < B} = f_{\lambda < u} + \alpha_{uB} f_{uB}, \quad (38)$$

where α_{uB} is the factor to convert f_{uB} to $f_{u \leq \lambda \leq B}$ (i.e. equation 34 with $S = uB$). To calculate α_{uB} , we use the spectra of 15 SE SNe (scaled to match the BV photometry) to estimate $f_{\lambda_u \leq \lambda \leq \lambda_B}$, and their uB photometry to compute f_{uB} . The calibration of α_{uB} as a function of $t - t_V^{\text{peak}}$ is provided in Table 7.

Figure 16 shows spectra of SN 2011dh at -14d and 15d since t_V^{peak} , along with the monochromatic fluxes estimated from the observed B and UVOT photometry. The effective wavelength of the $w2$ and $w1$ bands is not constant because it depends strongly on the SED shape, being larger for redder SEDs (see Appendix A). To estimate the unobserved UV flux (in our case, $f_{\lambda < w2}$), some authors extrapolate the bluest ($\bar{\lambda}_x, \bar{f}_x$) point linearly to zero flux at 200nm (e.g. Lyman et al. 2014; Taddia et al. 2018b; Sharon & Kushnir 2020). This has been justified by the argument that the contribution of the flux to the bolometric flux is negligible below this wavelength (e.g. see the UV spectra of Ben-Ami et al. 2012, 2015, and Kwok et al. 2022). Applying such an extrapolation, we find that the contribution of $f_{\lambda < w2}$ to $f_{\lambda < B}$ is lower than 10% for 95% of the available epochs, with a typical contribution value around 3%. Therefore, we choose to ignore this flux contribution. In addition, given the scarcity of UV spectra in the UVOT filter wavelength ranges, we adopt the flux computed with equation (32) and $S = \{w2, w1, u\}$ as $f_{\lambda < u}$.

The top panel of Figure 17 shows the UVC values as a function of the intrinsic $B - V$ color for epochs between 3 and 40 d since explosion. We express the observed correlation between UVC and $(B - V)_0$ as

$$\text{UVC} = \delta_{0,\text{UVC}} + \Psi_{0,\text{UVC}}((B - V)_0). \quad (39)$$

Minimising equation (21) with $X = (B - V)_0$ and $Y = \text{UVC}$, we obtain the δ_{UVC} values for each SN (bottom right panel) and $\Psi_{0,\text{UVC}}$ (bottom left panel). We adopt the mean and $\hat{\sigma}$ value of the δ_{UVC} estimates as $\delta_{0,\text{UVC}}$ and its error, respectively. The expression for UVC is then

$$\text{UVC} = 12.27 + 0.99(B - V)_0 \pm 0.19, \quad (40)$$

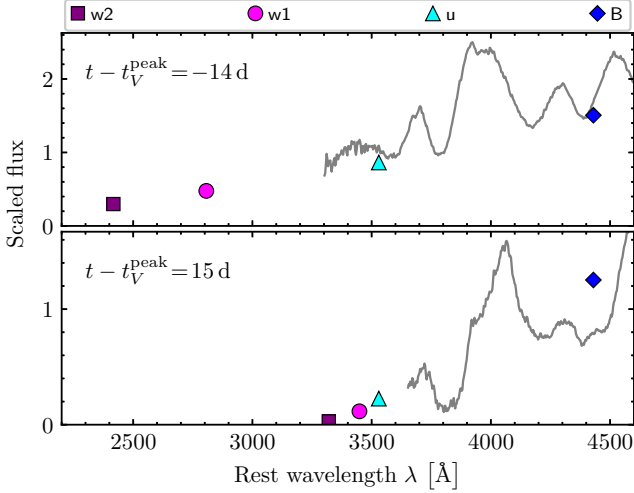


Figure 16. Spectra of SN 2011dh at -14 (top panel) and 15 d (bottom panel) since t_V^{peak} . Colored symbols are monochromatic fluxes computed from observed photometry.

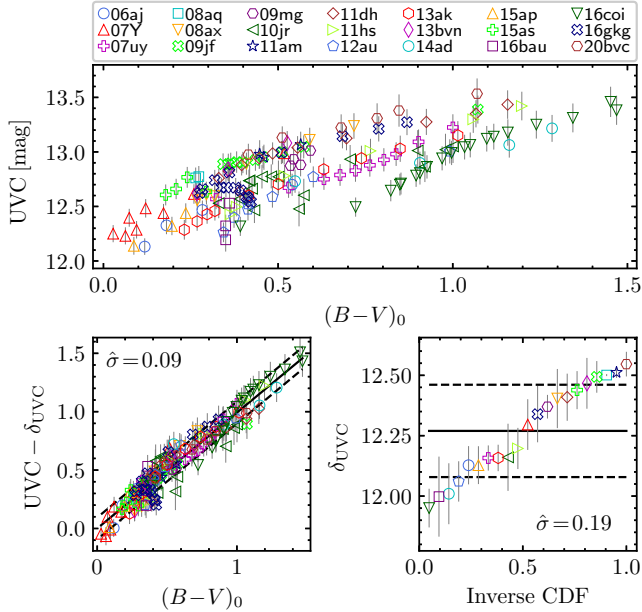


Figure 17. Top panel: UV corrections against the intrinsic $B-V$ color for $t - t_{\text{expl}} < 40$ d. Bottom left panel: UVC values shifted by δ_{UVC} , where the solid line is a straight line fit corresponding to $\Psi_{0,\text{UVC}}$. Bottom right panel: inverse CDF for the δ_{UVC} values, where the solid line is the mean value. Dashed lines are $\pm 1\hat{\sigma}$ limits, and error bars are 1σ errors.

which is valid for $t - t_{\text{expl}} < 40$ d. The UVC $\hat{\sigma}$ value we obtain is much lower than that previously reported by Pritchard et al. (2014) ($\hat{\sigma} = 0.63$ mag). The SN sample of that work is more heterogeneous, as it includes SNe II and II_n, which may partly explain their higher $\hat{\sigma}$ value.

In our sample, only SNe 2011dh, 2012au, and 2016coi have UVOT photometry at $t - t_{\text{expl}} > 40$ d. For

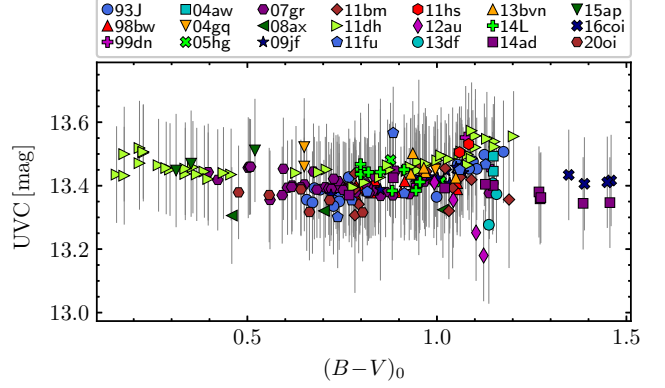


Figure 18. UV corrections against the intrinsic $B-V$ color for $t - t_{\text{expl}} > 40$ d.

those SNe, we obtain roughly constant UVC estimates, with mean values of 13.44 ± 0.04 , 12.93 ± 0.05 and 13.56 ± 0.07 mag, respectively. To check the constancy of UVC for such epochs, we use the UBV photometry of 21 SE SNe and assume $f_{\lambda < B} = \alpha_{UB} f_{UB}$. The calibration of α_{UB} , computed in the same way as α_{uB} , is reported in Table 7.

Figure 18 shows UVC against $(B-V)_0$ for $t - t_{\text{expl}} > 40$ d, where we see that the UVC estimates remain nearly constant. For SNe 2011dh, 2012au, and 2016coi we obtain mean UVC values of 13.49 ± 0.04 , 13.31 ± 0.10 , and 13.43 ± 0.07 mag, which are consistent with our previous finding within their errors. For the 21 SNe in the figure we compute a mean UVC of 13.42 ± 0.06 . Hereafter for $t - t_{\text{expl}} > 40$ d we adopt $\text{UVC} = 13.42 \pm 0.19$, where we assume an error of 0.19 mag in order not to underestimate the UVC uncertainty with respect to the error obtained for $t - t_{\text{expl}} < 40$ d.

3.6.3. Unobserved IR flux

We model the flux at $\lambda > \bar{\lambda}_{\text{IR}}$ as a power law, given by

$$f_{\lambda} = C \cdot (\lambda/\text{\AA})^k. \quad (41)$$

To measure the power law index k , we fit equation (41) to the $(\bar{\lambda}_x, \bar{f}_x)$ points computed with JHK or YJH photometry.

Figure 19 shows the k values obtained with the JHK (k_{JHK}) and YJH (k_{YJH}) photometry as a function of the intrinsic $V-H$ color. We can see that the k estimates are almost all larger than the power law index for the Rayleigh-Jeans tail of a Planck function ($k = -4$), which is typically assumed to model the IR flux of SE SNe (e.g. Lyman et al. 2014; Taddia et al. 2018b). Furthermore, k grows with redder color.

A linear fit only to the data points having relative k errors lower than 10% gives

$$k = -3.38[\pm 0.03] + 0.39[\pm 0.03](V-H)_0 \quad (42)$$

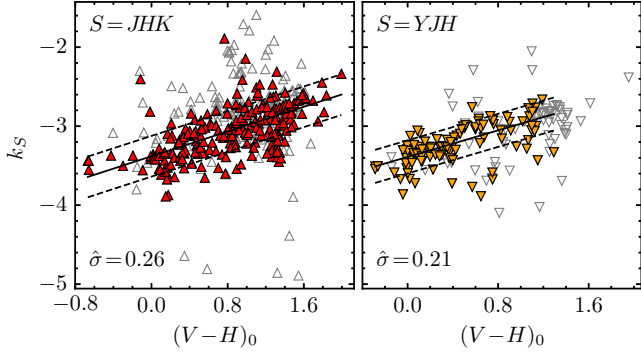


Figure 19. Power-law indices for the *JHK* (left-hand panel) and *YJH* (right-hand panel) photometry against the intrinsic $V-H$. Filled symbols are k values with relative errors lower than 10%. Solid lines are straight line fits to the filled symbols, dashed lines are $\pm 1 \hat{\sigma}$ limits. Error bars are omitted for clarity.

for *JHK*, and

$$k = -3.39[\pm 0.03] + 0.42[\pm 0.06](V-H)_0 \quad (43)$$

for *YJH*. The parameters of both fits are consistent with each other. As the k_{JHK} and k_{YJH} values come from independent SN samples, equations (42) and (43) are two independent estimates of the dependence of k on $(V-H)_0$. Combining both samples, we obtain the linear fit

$$k = -3.38[\pm 0.02] + 0.40[\pm 0.02](V-H)_0, \quad (44)$$

with $\sigma_0 = 0.12$ and $\hat{\sigma} = 0.24$. We use this expression to indirectly estimate k from the observed $(V-H)_0$ color, and then we adopt the weighted average of this value and k_{JHK} (or k_{YJH}) as the final k .

Once we determine k for each SN, we compute the corresponding C value fitting equation (41) to the IR photometry. We then calculate $f_{\lambda > x_{\text{IR}}}$ by integrating the power law from $\bar{\lambda}_{x_{\text{IR}}}$ to infinity, i.e.

$$f_{\lambda > x_{\text{IR}}} = -C \cdot (\bar{\lambda}_{x_{\text{IR}}}/\text{\AA})^{k+1}/(k+1). \quad (45)$$

3.6.4. Fractional flux evolution

Using equations (31), (34), (37), and (45) we next compute bolometric fluxes for 15 SNe IIb, 15 SNe Ib, and 19 SNe Ic having optical/IR photometry in bands between B and H/K .

Figure 20 shows the temporal evolution of the fractional flux in different wavelength ranges. Before t_V^{peak} , the contribution of $f_{\lambda < B}$ to f_{bol} is comparable to that of $f_{B \leq \lambda \leq x_{\text{IR}}}$, while $f_{\lambda > x_{\text{IR}}}/f_{\text{bol}}$ is $\lesssim 5\%$. After t_V^{peak} , $f_{\lambda < B}$ decreases drastically, accounting for $< 10\%$ of the bolometric flux at $t - t_V^{\text{peak}} \sim 20$ d. At that time, the contribution of $f_{\lambda > x_{\text{IR}}}$ to f_{bol} is about 5–15%, while

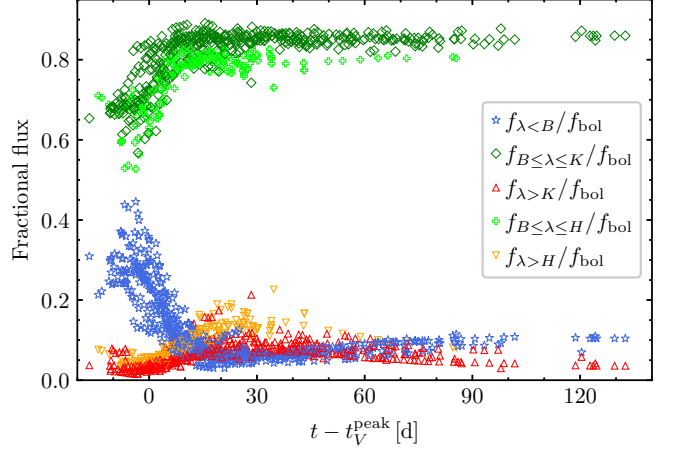


Figure 20. Fractional flux in a given wavelength range as a function of the time since the V -band maximum light.

$f_{B \leq \lambda \leq x_{\text{IR}}}$ accounts for $> 80\%$ of the bolometric flux. For $t - t_V^{\text{peak}} > 60$ d, the contribution of $f_{B \leq \lambda \leq K}$, $f_{\lambda < B}$, and $f_{\lambda > K}$ to f_{bol} remains at about 85, 10, and 5%, respectively.

3.7. Bolometric corrections

We define the bolometric correction as

$$\text{BC}_x = -2.5 \log(f_{\text{bol}}) - m_{x,0}, \quad (46)$$

which can be calibrated as a function of the color (e.g. Lyman et al. 2014). However, given that the color curves of SE SNe are non-monotonic (e.g. Stritzinger et al. 2018a), the same color can correspond to different epochs with different SEDs and therefore with different BC values.

The top panel of Figure 21 shows the BC_B estimates of SNe IIb against the intrinsic $B-V$ color, where blue (red) symbols correspond to $t - t_V^{\text{peak}}$ epochs before (after) the time of maximum $B-V$ color, t_{B-V}^{max} . We see that the BC_B values for $t - t_V^{\text{peak}} > t_{B-V}^{\text{max}}$ tend to be lower than those for $t - t_V^{\text{peak}} < t_{B-V}^{\text{max}}$ within the same color range. To disentangle this degeneracy, we parametrize the dependence of BC_x on a given color, $c = x - y$, as

$$\text{BC}_{x,c} = \begin{cases} \text{ZP}_{x,c} + a_1 c + a_2 c^2, & t - t_y^{\text{peak}} \leq t_c^{\text{max}} \\ \text{ZP}_{x,c} + a_3 + a_4 c, & t - t_y^{\text{peak}} > t_c^{\text{max}} \end{cases} \quad (47)$$

Here, $\text{ZP}_{x,c}$ is the zero-point for the BC calibration, while the a_i parameters are obtained by minimizing

$$s^2 = \sum_j^N \left[\sum_k^{\leq t_c^{\text{max}}} (\text{BC}_{x,j,k} - \delta_{\text{BC},j} - a_1 c_{j,k} - a_2 c_{j,k}^2)^2 + \sum_k^{> t_c^{\text{max}}} (\text{BC}_{x,j,k} - \delta_{\text{BC},j} - a_3 - a_4 c_{j,k})^2 \right]. \quad (48)$$

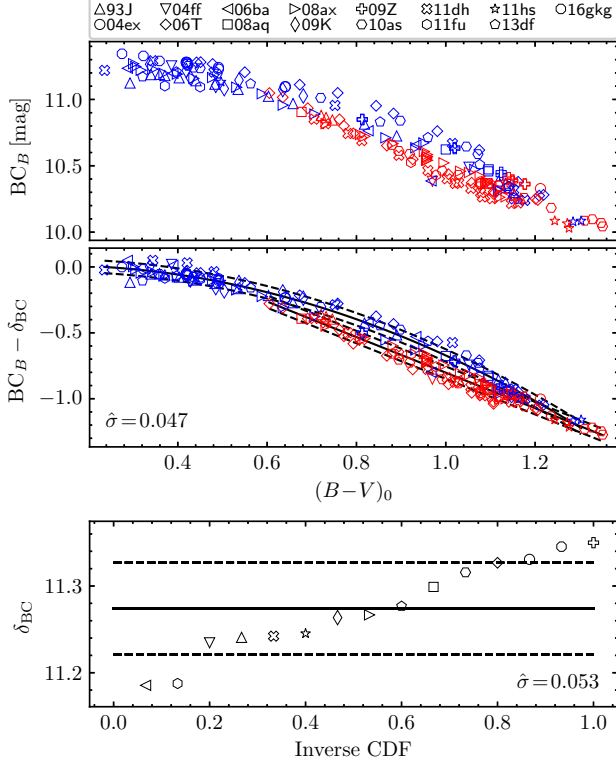


Figure 21. Top panel: BC_B values for SNe IIb versus the intrinsic $B-V$ color, where blue (red) symbols correspond to epochs before (after) the maximum of the $B-V$ color. Middle panel: BC_B values shifted by δ_{BC} , where solid lines are polynomial fits. Bottom panel: Inverse CDF for the δ_{BC} estimates, where the solid line indicates the mean value. Dashed lines are the $\pm 1\hat{\sigma}$ limits.

We adopt the mean and sample standard deviation of the $\delta_{BC,j}$ values as $ZP_{x,c}$ and its error, respectively.

The middle and bottom panels of Figure 21 show the result of the minimisation of equation (48), while Table F9 summarizes the BC parameters for different combinations of bands and colors. We also compare the M_r^{peak} distributions of the SNe IIb, Ib, and Ic used to calibrate BCs for different band-color combinations with the M_r^{peak} distributions of VL samples (see Section 3.5.4), finding p_{AD} values greater than 0.12, 0.18, and 0.35 for SNe IIb, Ib, and Ic, respectively. Based on this, we can expect that the luminosities computed with the BC technique are not, on average, over- or underestimated.

In Figure 22 we compare our BC calibrations with those of Lyman et al. (2014, 2016), which were computed with 15 SE SNe (3 SNe IIb, 6 SNe Ib, and 6 SNe Ic). From the latter calibrations we subtract the zero-point used by the authors to define the bolometric magnitude scale (equivalent to -11.497 mag). In the residuals panels we see that our BC calibrations are con-

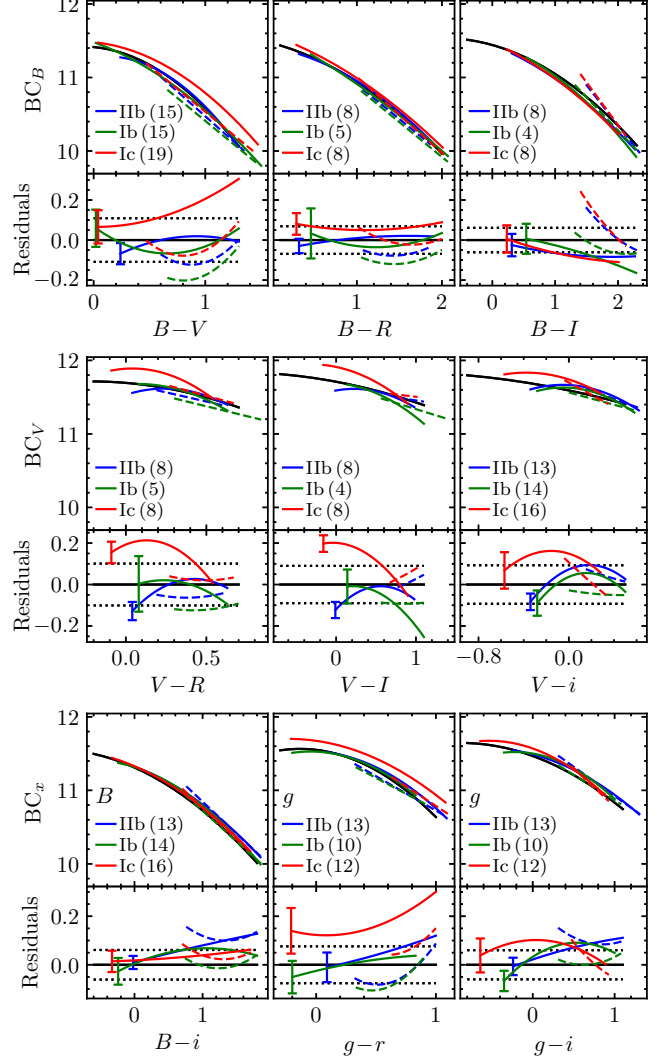


Figure 22. BC calibrations along with the residuals with respect to the Lyman et al. (2014, 2016) calibrations (black lines). Colored solid (dashed) lines are our BC calibrations for times before (after) the epoch of maximum color. The number of SNe used to calibrate the BC is indicated in parentheses. Error bars indicate the 1σ error around our calibrations, while dotted lines indicate the $\pm 1\hat{\sigma}$ limits of the Lyman et al. (2014, 2016) calibrations.

sistent with those of Lyman et al. (2014, 2016) to within their errors.

3.8. Bolometric light curves

We now apply the results of the previous sections to the data in order to derive bolometric light curves for the SN sample. For a SN with photometry in n optical bands, we compute luminosities for each of the $n - 1$ independent band-color combinations using

$$\log L_{x,c} = (\mu - BC_{x,c} - m_{x,0})/2.5 - 2.922 \quad (49)$$

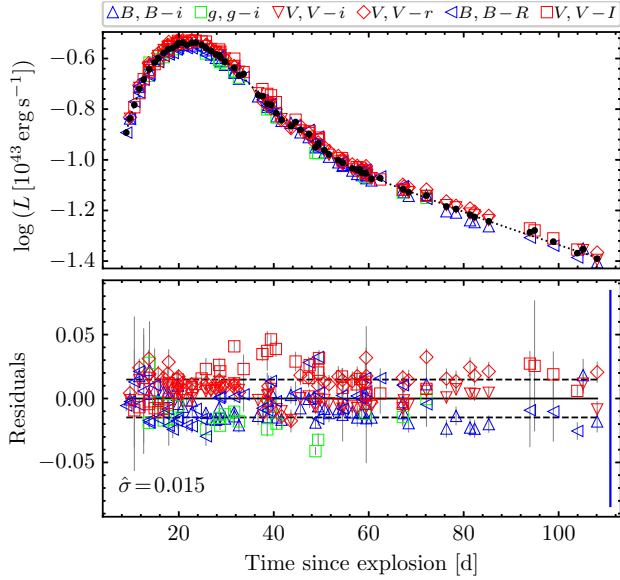


Figure 23. Top panel: bolometric light curve of SN 2009jf computed with different band-color combinations (empty symbols). The dotted line is the ALR fit to the weighted average light curve (black circles). Bottom panel: residuals around the ALR fit. Error bars are 1σ errors due to uncertainties on photometry, while the blue vertical bar depicts the 1σ error at peak due to the error on μ , reddening, and BC. Dashed lines are the $\pm 1\hat{\sigma}$ limits.

(e.g. Rodríguez et al. 2021). Then, we adopt the weighted mean of the $\log L_{x,c}$ estimates in windows of 0.25 d as the final $\log L$ values, with weights

$$w_{x,c} = \left[\left[1 + \frac{dBC_{x,c}}{dc} \right]^2 \sigma_{m_x}^2 + \left[\frac{dBC_{x,c}}{dc} \right]^2 \sigma_{m_y}^2 \right]^{-1}. \quad (50)$$

As an example, Figure 23 shows the bolometric light curve of SN 2009jf computed with $BgVrRi$ photometry. Figure 24 shows the final bolometric light curves for the sample, interpolated with the ALR code.

The error on $\log L$ is given by

$$\sigma_{\log L} = 0.4 \sqrt{\sigma_{\text{phot}}^2 + \sigma_{\text{BC}}^2 + \sigma_{\mu}^2 + \sigma_E^2}, \quad (51)$$

where σ_{phot} , σ_{BC} , and σ_E are the errors due to uncertainties on photometry, BC ZP, and reddening, respectively. The σ_{phot} and σ_{BC} errors are the weighted mean errors computed with equation (50) and with $w_{x,c} = 1/\sigma_{\text{ZP},x,c}^2$, respectively, while

$$\sigma_E = \sqrt{\zeta_{\text{MW}}^2 \sigma_{E_{B-V}^{\text{MW}}}^2 + \zeta_{\text{h}}^2 \sigma_{E_{B-V}}^2}. \quad (52)$$

Here,

$$\zeta_s = \frac{1}{n-1} \sum_{x,c} \left[R_x^s + (R_x^s - R_y^s) \frac{dBC_{x,c}}{dc} \right], \quad (53)$$

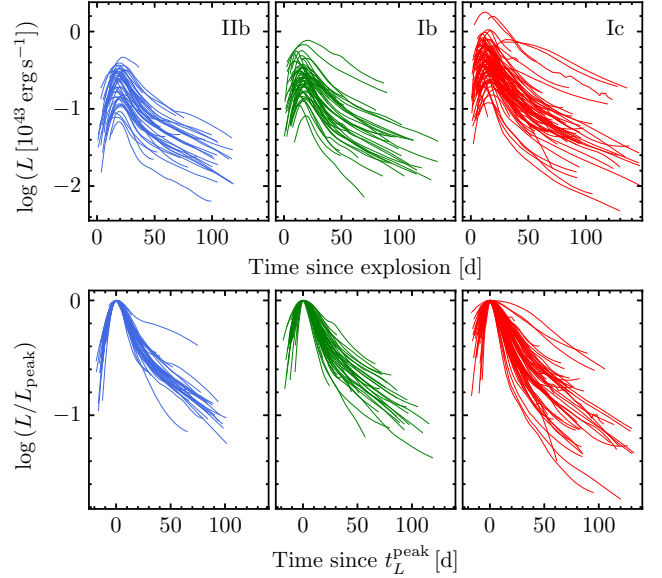


Figure 24. Bolometric SN light curves interpolated with the ALR code (top panels) and normalized to the peak (bottom panels).

where $s = \{\text{h, MW}\}$ and $R_x^s = A_x^s/E_{B-V}^s$ (see Appendix B).

3.9. Explosion parameters

From the bolometric light curves derived above we now measure $\log L_{\text{peak}}$, t_L^{peak} , and the decline rate $\Delta m_{15}(\text{bol}) = 2.5 \log(L_{\text{peak}}/L(t_L^{\text{peak}} + 15 \text{ d}))$, which are listed in Table F10. We then compute $\log M_{\text{Ni}}$ and t_{esc} using the procedure described in Section 3.1.1. Figure 25 shows, for example, the $\log M_{\text{Ni}}$ estimates of SN 2009jf as a function of the time since explosion before (top panel) and after (bottom panel) correcting for the γ -ray deposition function.

The error on $\log M_{\text{Ni}}$ is given by

$$\sigma_{\log M_{\text{Ni}}} = \sqrt{\tilde{\sigma}_{\log M_{\text{Ni}}}^2 + \sigma_t^2 + \frac{\sigma_{\text{BC}}^2 + \sigma_{\mu}^2 + \sigma_E^{\text{tail}^2}}{6.25}}, \quad (54)$$

where $\tilde{\sigma}_{\log M_{\text{Ni}}}$ is the uncertainty due to errors on photometry and t_{esc} (provided by EMCEE), σ_t is the error in $\log M_{\text{Ni}}$ due to the uncertainty in t_{expl} , while σ_E^{tail} is the σ_E error in the radioactive tail. To estimate σ_t , we compute $\log M_{\text{Ni}}$ assuming $t_{\text{expl}} = t_{\text{non-det}}$ and $t_{\text{expl}} = t_{\text{detect}}$. These epochs correspond to the lowest and greatest possible value for t_{expl} . Figure 26 shows the change in $\log M_{\text{Ni}}$ ($\Delta \log M_{\text{Ni}}$) versus the change in t_{expl} (Δt_{expl}). The distribution, which is well represented by the straight line $\Delta \log M_{\text{Ni}} = -0.0001 - 0.0054(\Delta t_{\text{expl}}/\text{d})$, indicates that $\log M_{\text{Ni}}$ decreases as t_{expl} advances. Based on this, we adopt $\sigma_t = 0.0054 \sigma_{t_{\text{expl}}} \text{ d}^{-1}$. The $\log M_{\text{Ni}}$ and t_{esc} values are summarized in Columns 8 and 9 of

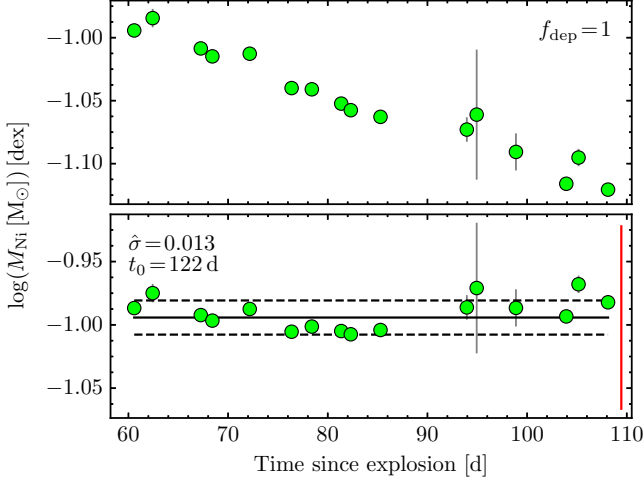


Figure 25. $\log M_{\text{Ni}}$ estimates for SN 2009jf versus the time since explosion, before (top panel) and after (bottom panel) correcting for the γ -ray deposition function. The solid horizontal lines corresponds to the $\log M_{\text{Ni}}$ value that maximizes the posterior probability, while dashed lines are the $\pm 1\hat{\sigma}$ limits. Error bars are 1σ errors due to uncertainties on photometry, while the red vertical bar depicts the 1σ error due to the uncertainty on μ , reddening, explosion epoch, and BC.

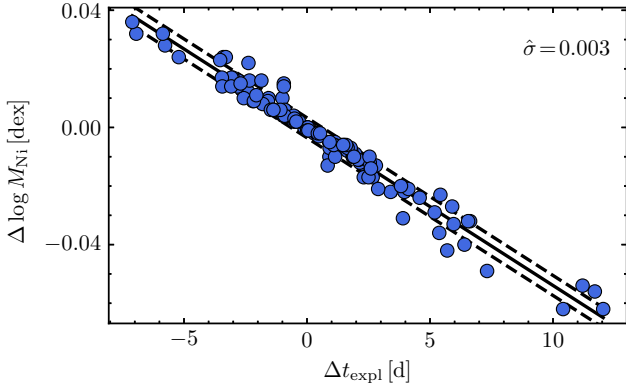


Figure 26. Change in $\log M_{\text{Ni}}$ against change in explosion time. Negative (positive) Δt_{expl} values are quantities computed using $t_{\text{non-det}}$ (t_{detect}) as explosion time. The solid line is a straight line fit and dashed lines are $\pm 1\hat{\sigma}$ limits.

Table F10, respectively. The mean $\log M_{\text{Ni}}$ error for our SN sample is 0.120 dex, of which 65, 31, 2, 1.5, and 0.5% is induced by σ_E^{tail} , σ_μ , σ_{BC} , $\tilde{\sigma}_{\log M_{\text{Ni}}}$, and σ_t , respectively.

We also compute $\log(L_{\text{peak}}/M_{\text{Ni}})$ for the 20 SNe I Ib, 21 SNe Ib, and 34 SNe Ic with $\log M_{\text{Ni}}$ estimates. The error on $\log(L_{\text{peak}}/M_{\text{Ni}})$ is given by

$$\sigma_{\log(L_{\text{peak}}/M_{\text{Ni}})} = \sqrt{\tilde{\sigma}_{\log M_{\text{Ni}}}^2 + \sigma_t^2 + \frac{\sigma_{\text{phot}}^{\text{peak}^2} + \sigma_E^{\text{pt}^2}}{6.25}}, \quad (55)$$

where $\sigma_{\text{phot}}^{\text{peak}}$ is the σ_{phot} error at peak time, and

$$\sigma_E^{\text{pt}} = \sqrt{[\zeta_{\text{MW}}^{\text{peak}} - \zeta_{\text{MW}}^{\text{tail}}]^2 \sigma_{E_{\text{B-V}}^{\text{MW}}}^2 + [\zeta_{\text{h}}^{\text{peak}} - \zeta_{\text{h}}^{\text{tail}}]^2 \sigma_{E_{\text{B-V}}}^2}, \quad (56)$$

where the terms ζ_s^{peak} and ζ_s^{tail} for $s = \{\text{MW}, \text{h}\}$ are given by equation (53) evaluated at t_L^{peak} and in the radioactive tail, respectively. The $\log(L_{\text{peak}}/M_{\text{Ni}})$ estimates and their errors are listed in Column 10 of Table F10. The typical $\log(L_{\text{peak}}/M_{\text{Ni}})$ error is 0.031 dex, of which 72, 19, 7, and 2% is induced by σ_E^{pt} , $\tilde{\sigma}_{\log M_{\text{Ni}}}$, σ_t , and $\sigma_{\text{phot}}^{\text{peak}}$, respectively.

A rough estimate of the ejecta mass (M_{ej}) and the kinetic energy (E_{k}) can be computed with the relations

$$M_{\text{ej}} = \frac{1}{2} \left(\frac{13.7c}{\kappa} \right) (t_L^{\text{peak}})^2 v_{\text{peak}} \quad (57)$$

(e.g. Prentice et al. 2019) and

$$E_{\text{k}} = 0.3 M_{\text{ej}} v_{\text{peak}}^2 \quad (58)$$

(e.g. Prentice et al. 2016), where v_{peak} is the velocity of the ejecta at t_L^{peak} , c is the light speed, and $\kappa = 0.07 \text{ cm}^2 \text{ g}^{-1}$ is the opacity of the ejecta⁹. For 68 SNe in our dataset we adopt the v_{peak} values reported by Prentice et al. (2019), who use the He I $\lambda 5876$ and Si II $\lambda 6355$ absorption lines to estimate the expansion velocities of SNe I Ib/Ib and Ic, respectively. We use the same lines to measure the expansion velocities of 87 SNe, which we adopt as v_{peak} if the epoch of the spectrum (t_{spec}) is within ± 3 d since t_L^{peak} . If t_{spec} is more than three days lower (greater) than t_L^{peak} , then we adopt the measured velocity as an upper (lower) limit for v_{peak} . For seven SNe, where the presence of He I $\lambda 5876$ or Si II $\lambda 6355$ absorption lines in the spectra is unclear, we adopt the expansion velocities inferred from the Fe II $\lambda 5169$ absorption line. For 14 SNe without public spectra, we adopt the expansion velocities reported in the literature. We assume an error of 15% for all expansion velocities. The v_{peak} , M_{ej} , and E_{k} estimates are collected in Columns 5, 6, and 7 of Table F10, respectively. The reported errors on M_{ej} and E_{k} are random and do not account for systematic errors due to the use of the highly approximate equations (57) and (58).

4. RESULTS

4.1. Distributions and correlations

⁹ The relations for M_{ej} and E_{k} are based on Arnett's rule, which does not hold for SE SNe (Khatami & Kasen 2019). Therefore, the derived M_{ej} and E_{k} values should be treated with caution.

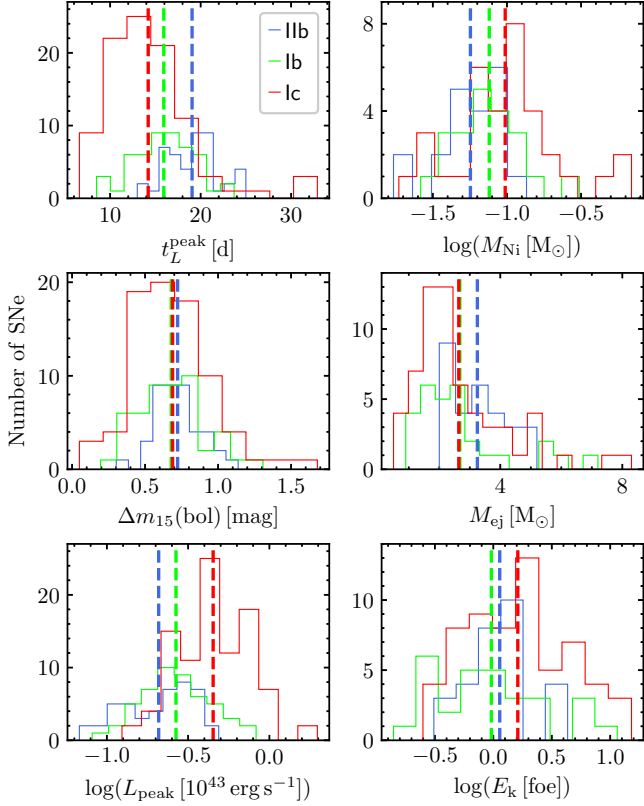


Figure 27. Histograms of the bolometric light-curve properties (left-hand panels) and the explosion parameters (right-hand panels). Dashed lines indicate mean values.

Figure 27 shows the histograms of the bolometric light-curve properties and the explosion parameters, and Table 8 summarises the statistics of those distributions. The ^{56}Ni mass distribution is discussed further in Section 4.3. The mean values of the t_L^{peak} and $\Delta m_{15}(\text{bol})$ distributions are similar to, and ~ 0.15 mag lower than, respectively, the estimates inferred for the V -band (see Section 3.4). The mean peak luminosity, mean ^{56}Ni mass, and mean kinetic energy increase in the sequence of IIb–Ib–Ic subtypes. The median peak luminosities and mean kinetic energies are consistent with those reported by [Prentice et al. \(2016\)](#) and [Lyman et al. \(2016\)](#), respectively. All SE SN subtypes have similar mean M_{ej} values around $2.6\text{--}3.2 M_{\odot}$, which are consistent with the mean M_{ej} of $2.8 M_{\odot}$ for all SE SNe reported by [Prentice et al. \(2019\)](#). Based on the $\hat{\sigma}$ values and ranges of explosion parameters and bolometric light-curve properties, we find that SE SNe become more heterogeneous in the sequence of IIb–Ib–Ic subtypes. The relative homogeneity of SNe IIb has been previously noted by [Lyman et al. \(2016\)](#).

For comparison with models, in Table 9 we list the average explosion parameters and bolometric light-

Table 8. Statistics of the bolometric light-curve properties and explosion parameters

Type	N	Min	Max	Mean	Median	$\hat{\sigma}$	Range
t_L^{peak} [d]							
IIb	45	13.0	25.0	19.1	19.3	2.8	12.0
Ib	50	8.5	23.7	15.9	16.0	3.3	15.2
Ic	96	6.6	32.9	14.2	13.3	4.9	26.3
$\Delta m_{15}(\text{bol})$ [mag]							
IIb	42	0.30	1.14	0.72	0.71	0.16	0.83
Ib	49	0.20	1.31	0.68	0.65	0.23	1.11
Ic	81	0.05	1.68	0.69	0.67	0.27	1.63
$\log L_{\text{peak}}$ [10^{43} erg s $^{-1}$]							
IIb	45	-1.17	-0.31	-0.68	-0.63	0.21	0.86
Ib	50	-1.09	-0.08	-0.57	-0.58	0.22	1.01
Ic	96	-0.91	0.29	-0.35	-0.36	0.22	1.20
M_{Ni} [M_{\odot}]							
IIb	20	0.018	0.138	0.065	0.062	0.03	0.12
Ib	21	0.027	0.322	0.091	0.079	0.06	0.29
Ic	34	0.019	0.706	0.145	0.107	0.15	0.69
$\log M_{\text{Ni}}$ [M_{\odot}]							
IIb	20	-1.76	-0.87	-1.25	-1.23	0.22	0.90
Ib	21	-1.58	-0.51	-1.12	-1.12	0.24	1.07
Ic	34	-1.73	-0.16	-1.01	-1.00	0.35	1.57
M_{ej} [M_{\odot}]							
IIb	29	2.0	5.2	3.2	3.2	0.9	3.2
Ib	29	0.9	7.2	2.7	2.3	1.6	6.3
Ic	61	0.5	8.3	2.6	2.2	1.6	7.8
E_{k} [foe]							
IIb	29	0.31	4.32	1.41	1.13	1.05	4.01
Ib	29	0.14	11.48	1.87	0.93	2.63	11.34
Ic	61	0.25	15.20	2.80	1.56	3.30	14.95
$\log E_{\text{k}}$ [foe]							
IIb	29	-0.51	0.64	0.05	0.05	0.29	1.14
Ib	29	-0.85	1.06	-0.02	-0.03	0.49	1.91
Ic	61	-0.60	1.18	0.21	0.19	0.46	1.78

curve properties of the CMFGEN models for SNe IIb, Ib, and Ic presented in [Dessart et al. \(2016\)](#) along with the initial mass function (IMF) averaged characteristics of the SEDONA models for SNe Ib/Ic reported by [Woosley et al. \(2021\)](#). The progenitors of the [Dessart et al. \(2016\)](#) ([Woosley et al. 2021](#)) models are mass donors (stripped helium stars) in close-binary systems. Based on the H/He composition of the ejecta models, [Dessart et al. \(2016\)](#) classified 17, 6, and 4 of their 27 models as SNe IIb, Ib, and Ic, respectively. Among the [Woosley et al. \(2021\)](#) models, we select 41

with standard mass-loss rate and initial helium star masses of 3.3 to 8.0 M_{\odot} , which were found to be consistent with normal SNe Ib and Ic (i.e., SNe Ic-BL and GRB-SNe are not included, see [Woosley et al. 2021](#)). In the table we also list the average characteristics we obtain for SNe IIB, Ib, and Ic (excluding SNe Ic-BL) in our sample, and the corresponding mean values for SNe Ib/Ic adopting that 35.6% and 21.5% of all SE SNe are of Type Ib and Ic (excluding Ic-BL and peculiar events), respectively ([Shivvers et al. 2017](#)).

The models of [Dessart et al. \(2016\)](#) for SNe IIB have mean $\Delta m_{15}(\text{bol})$, E_k , and M_{Ni} consistent with our estimates to 1.7σ , while the average t_L^{peak} and $\log L_{\text{peak}}$ are 5 d longer and 0.15 dex lower than our estimates, respectively. The models for SNe Ib and Ic have average $\log L_{\text{peak}}$ and E_k consistent with our estimates to 2.1σ , while the mean $\Delta m_{15}(\text{bol})$ and t_L^{peak} are at least 0.25 mag lower and 16.8 d longer than our estimates, respectively. The models of [Woosley et al. \(2021\)](#) for SNe Ib/Ic have IMF-averaged M_{ej} , E_k , and M_{Ni} values lower than our mean estimates but consistent with them to 2.6σ , while the IMF-averaged $\log L_{\text{peak}}$ and t_L^{peak} are 0.22 dex lower and 5.8 d longer than our mean values, respectively.

Models of [Dessart et al. \(2016\)](#) and [Woosley et al. \(2021\)](#) have mean $\log(L_{\text{peak}}/M_{\text{Ni}})$ and t_L^{peak} values at least 5σ lower and longer than observations, respectively. If the systematic differences between the average t_L^{peak} of models and observations are because we overestimate t_{expl} , then the $\log M_{\text{Ni}}$ values computed from observations are underestimated (see Section 3.9) and therefore the observed average $\log(L_{\text{peak}}/M_{\text{Ni}})$ values are overestimated. Reducing the explosion epochs of the observed SNe IIB, Ib, Ic, and Ib/Ic by 5.0, 19.5, 16.8, and 5.8 d (the differences of the mean t_L^{peak} values for models and observations), respectively, the observed average $\log(L_{\text{peak}}/M_{\text{Ni}})$ estimates reduce to 0.49 ± 0.02 , 0.44 ± 0.03 , 0.51 ± 0.06 , and 0.54 ± 0.03 dex, respectively. These values are at least 4σ greater than those computed from models. This means that, even if our explosion epochs are overestimated, the mean ratio of peak luminosity to ^{56}Ni mass for models is 0.13–0.25 dex lower than observations. The latter suggests that models of [Dessart et al. \(2016\)](#) and [Woosley et al. \(2021\)](#) underestimate the peak luminosity of SE SNe, which is consistent with findings in previous studies (e.g. [Ertl et al. 2020](#); [Afsariardchi et al. 2021](#); [Woosley et al. 2021](#); [Sollerman et al. 2022](#); see Section 1). This is further discussed in Section 5.4.

Figure 28 summarizes the r_p values of the correlations between bolometric light-curve properties and explosion parameters for each SN subtype. We focus on correlations with $|r_p| \geq 0.5$ (i.e. moderate/strong correlations). For those correlations we measure $p_P \leq 0.003$, i.e. they are significant at the $> 99.7\%$ level. We recover the correlation between $\log M_{\text{Ni}}$ and $\log L_{\text{peak}}$, and between $\log E_k$ and $\log M_{\text{ej}}$ reported in previous works (e.g. [Lyman et al. 2016](#); [Taddia et al. 2018b, 2019](#); [Barbarino et al. 2021](#)). We also recover the correlations between $\log M_{\text{Ni}}$ and $\log M_{\text{ej}}$ for SNe Ic (e.g. [Taddia et al. 2019](#); [Barbarino et al. 2021](#)). The observed correlation between $\log M_{\text{ej}}$ and $\Delta m_{15}(\text{bol})$ (top panels of Figure 29) is expected because the diffusion time increases with M_{ej} (e.g. [Arnett 1982](#)). For SNe Ib and Ic we detect a correlation between t_L^{peak} and $\Delta m_{15}(\text{bol})$, and between $\log M_{\text{ej}}$ and t_L^{peak} . The first correlation is consistent with our findings for the V-band in Section 3.4, while the second correlation is equivalent to the first one since $\log M_{\text{ej}}$ and $\Delta m_{15}(\text{bol})$ are correlated. For SNe Ic we find correlations between $\log E_k$ and $\log L_{\text{peak}}$, $\log M_{\text{Ni}}$ and $\Delta m_{15}(\text{bol})$ (also for SNe Ib), and between $\log M_{\text{Ni}}$ and t_L^{peak} . The latter two correlations are consistent with the picture that $\log M_{\text{Ni}}$ and $\log M_{\text{ej}}$ correlate for SNe Ic (bottom panels of Figure 29). In our case, the latter correlation is given by

$$\log(M_{\text{Ni}} [M_{\odot}]) = -1.452 + \log(M_{\text{ej}} [M_{\odot}]) \pm 0.24 \quad (59)$$

(1σ error), or $M_{\text{Ni}}/M_{\text{ej}} = 4.1_{-1.8}^{+3.1}\%$.

4.2. Peak time-luminosity relation

The top panels of Figure 30 show $\log(L_{\text{peak}}/M_{\text{Ni}})$ as a function of t_L^{peak} (the peak time-luminosity relation) for each SN subtype and for SE SNe as a whole. We see that the distributions for different SN subtypes are similar. In particular, SN IIB 2013bb (the most massive H/He-rich SNe yet found, [Prentice et al. 2019](#)) is located close to the slow-rising ($t_L^{\text{peak}} > 30$ d) SNe Ic. This is consistent with the finding of [Woosley et al. \(2021\)](#), who suggest that SN 2013bb belongs to the SNe Ib/Ic group but with a more massive progenitor and with a small residual H envelope. In the figure we also show the models of [Dessart et al. \(2016\)](#) and [Woosley et al. \(2021\)](#).

Table 10 lists the β values for each SN subtype and for SE SNe as a whole obtained by fitting the [Khatami & Kasen \(2019\)](#) relation (equation 12) to our data (Column 2) and to the models of [Dessart et al. \(2016\)](#) (β_D , Column 4), along with the empirical mean β values reported by [Afsariardchi et al. \(2021\)](#) and their σ/\sqrt{N} errors (β_A , Column 3). For completeness, we also compute β for SNe Ic classified as Ic-BL and for SNe Ic, Ib/Ic, and SE SNe without including SNe Ic-BL.

Table 9. Average bolometric light-curve properties and explosion parameters

	I Ib	Ib	Ic	Ib/Ic
	This work			
$\log L_{\text{peak}} [10^{43} \text{ erg s}^{-1}]$	-0.68 ± 0.03 (45)	-0.57 ± 0.03 (50)	-0.40 ± 0.03 (70)	-0.51 ± 0.02
$t_L^{\text{peak}} [\text{d}]$	19.1 ± 0.4 (45)	15.9 ± 0.5 (50)	15.0 ± 0.6 (70)	15.6 ± 0.4
$\Delta m_{15} (\text{bol})$	0.72 ± 0.02 (42)	0.68 ± 0.03 (49)	0.66 ± 0.04 (57)	0.67 ± 0.03
$M_{\text{ej}} [M_{\odot}]$	3.2 ± 0.2 (29)	2.7 ± 0.3 (29)	2.6 ± 0.3 (42)	2.7 ± 0.2
$E_k [\text{foe}]$	1.41 ± 0.19 (29)	1.87 ± 0.49 (29)	1.55 ± 0.25 (42)	1.75 ± 0.32
$M_{\text{Ni}} [M_{\odot}]$	0.065 ± 0.006 (20)	0.091 ± 0.014 (21)	0.157 ± 0.034 (25)	0.116 ± 0.015
$\log(L_{\text{peak}}/M_{\text{Ni}})$	0.52 ± 0.02 (20)	0.55 ± 0.03 (21)	0.60 ± 0.06 (25)	0.57 ± 0.03
	Dessart et al. (2016)			Woosley et al. (2021)
$\log L_{\text{peak}} [10^{43} \text{ erg s}^{-1}]$	-0.83 ± 0.04 (17)	-0.50 ± 0.10 (6)	-0.62 ± 0.10 (4)	-0.73
$t_L^{\text{peak}} [\text{d}]$	24.1 ± 0.9 (17)	35.4 ± 2.1 (6)	31.8 ± 1.4 (4)	21.4
$\Delta m_{15} (\text{bol})$	0.66 ± 0.03 (17)	0.33 ± 0.03 (6)	0.41 ± 0.02 (4)	–
$M_{\text{ej}} [M_{\odot}]$	2.4 ± 0.1 (17)	5.0 ± 0.0 (6)	3.6 ± 0.0 (4)	2.19
$E_k [\text{foe}]$	1.80 ± 0.35 (17)	2.99 ± 0.76 (6)	1.88 ± 0.35 (4)	1.06
$M_{\text{Ni}} [M_{\odot}]$	0.069 ± 0.006 (17)	0.211 ± 0.036 (6)	0.140 ± 0.028 (4)	0.09
$\log(L_{\text{peak}}/M_{\text{Ni}})$	0.36 ± 0.01 (17)	0.22 ± 0.01 (6)	0.26 ± 0.01 (4)	0.32

NOTE—Uncertainties are the standard error of the mean ($\hat{\sigma}/\sqrt{N}$). Numbers in parentheses are the sample sizes. SNe Ic and Ib/Ic do not include SNe Ic-BL. Values of Woosley et al. (2021) are IMF-averaged quantities.

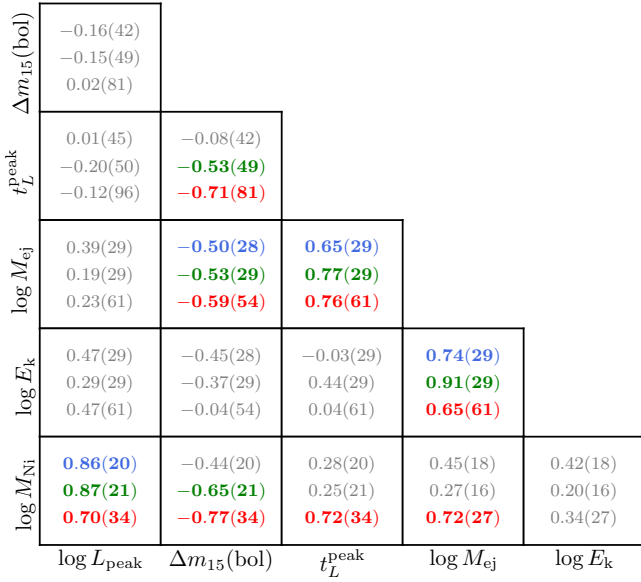


Figure 28. Correlation matrix of the bolometric light-curve properties and explosion parameters. The Pearson correlation coefficient and the number of SNe (in parenthesis) are reported for SNe I Ib (top values), Ib (middle values), and Ic (bottom values). Correlations with $|r_P| \geq 0.5$ are indicated with bold colored numbers.

As expected, the β_D value for SE SNe is consistent with $\beta = 9/8$ reported by Khatami & Kasen (2019), which is based on the SN models of Dessart et al. (2016). Our

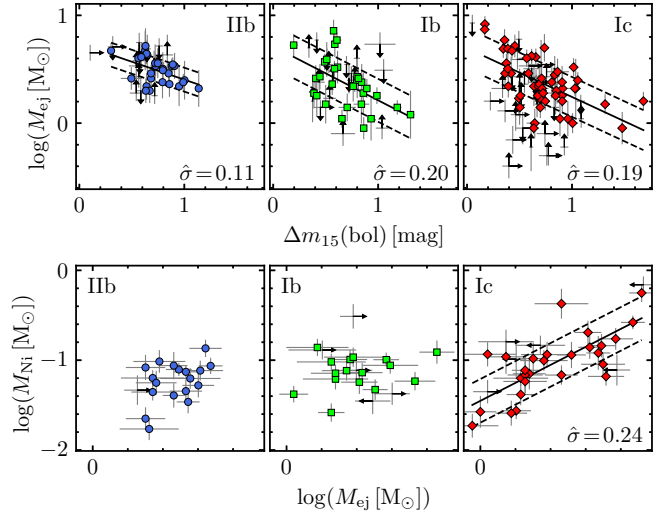


Figure 29. Ejecta mass against decline rate (top panels) and ^{56}Ni mass measured from the radioactive tail luminosity against ejecta mass (bottom panels). Solid lines correspond to linear fits, while dashed lines are the $\pm 1 \hat{\sigma}$ limits. Arrows indicate lower/upper limits and error bars are 1σ errors.

β estimates are, in general, greater than the β_A values but consistent with them to within $0.1\text{--}2.3\sigma$. In addition, our β values reduce but do not resolve the tension detected by Afsariardchi et al. (2021) between empirical β values and those based on the models of

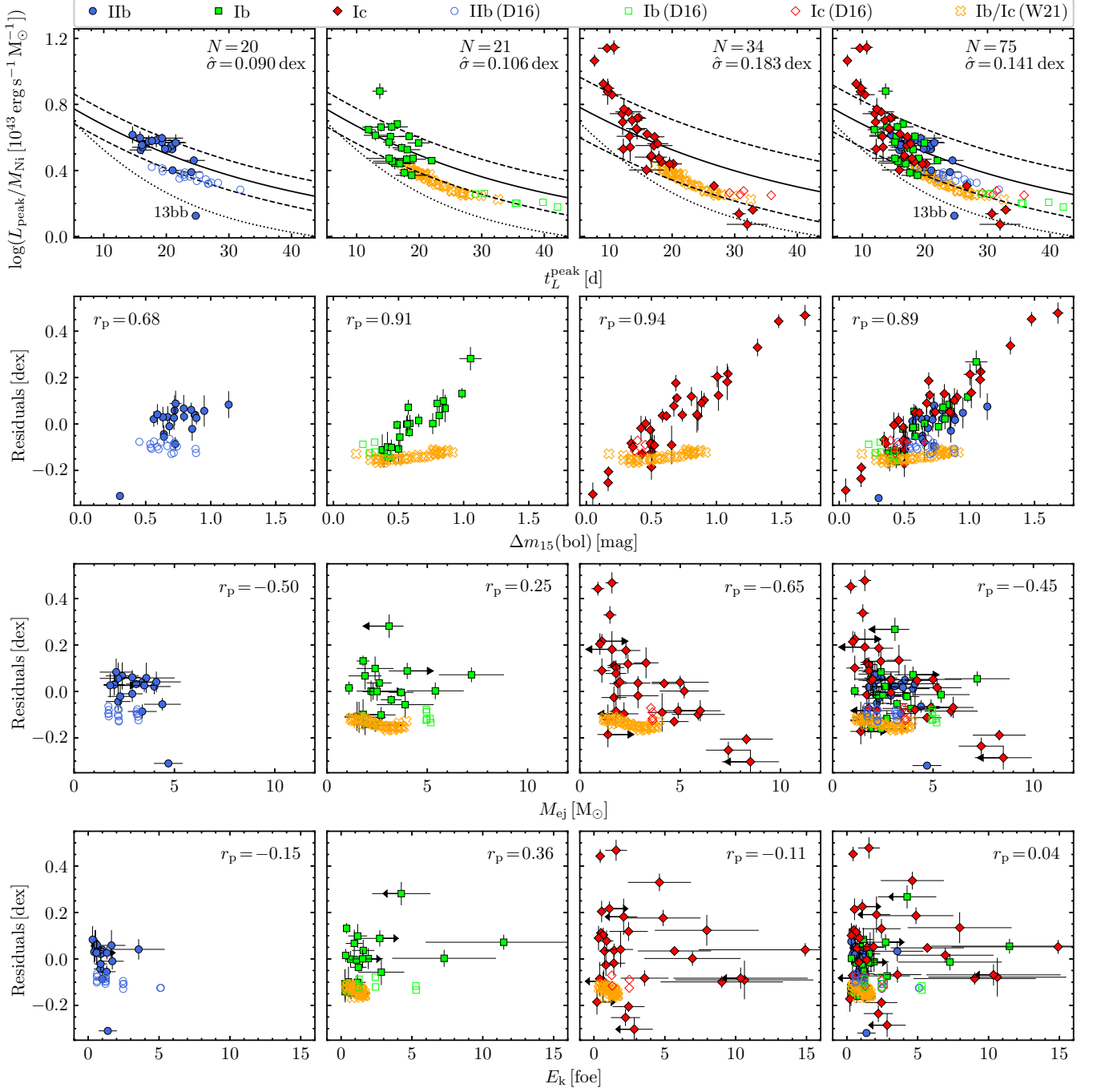


Figure 30. Top row: peak time-luminosity relations for SE SNe. Solid lines correspond to the Khatami & Kasen (2019) relation (equation 12) fitted to observations (filled symbols), and dashed lines are $\pm 1 \hat{\sigma}$ limits. Dotted lines correspond to Arnett’s rule. Second, third, and fourth rows: residuals against decline rate, ejecta mass, and kinetic energy, respectively, where the Pearson correlation coefficient is indicated in each panel. Error bars are 1σ errors, and arrows indicate lower/upper limits. We also show the models of Dessart et al. (2016) and Woosley et al. (2021) with empty symbols.

Table 10. β parameters for the peak time-luminosity relation

Type	β	β_A	β_D
I Ib	$0.88 \pm 0.07(20)$	$0.78 \pm 0.07(8)$	$1.15 \pm 0.02(17)$
Ib	$0.90 \pm 0.08(21)$	$0.66 \pm 0.07(8)$	$1.19 \pm 0.05(6)$
Ic	$0.81 \pm 0.10(34)$	–	–
Ic ^a	$0.86 \pm 0.13(25)$	$0.88 \pm 0.31(4)$	$1.15 \pm 0.11(4)$
Ic-BL	$0.64 \pm 0.19(9)$	$0.56 \pm 0.12(7)$	–
Ib/Ic ^a	$0.88 \pm 0.08(46)$	–	$1.18 \pm 0.03(10)$
SE ^a	$0.88 \pm 0.06(66)$	–	$1.16 \pm 0.02(27)$
SE	$0.85 \pm 0.05(75)$	$0.70 \pm 0.07(27)$	–

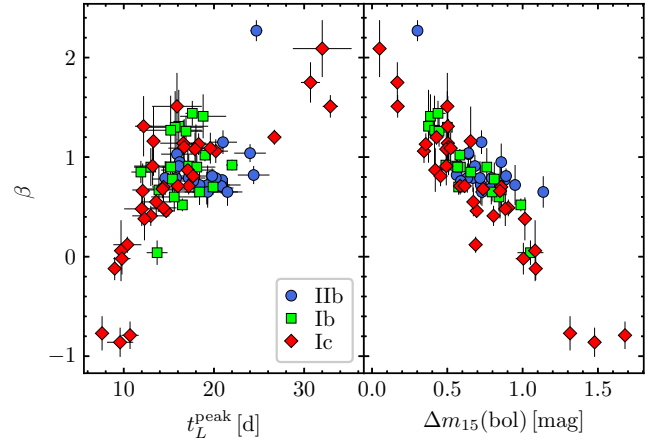
NOTE—Uncertainties are 1σ errors. Numbers in parentheses are the sample sizes.

^aWithout including SNe Ic-BL.

Dessart et al. (2016). We also find a discrepancy of 6σ between our β value for SNe Ib/Ic and $\beta = 1.36$ reported by Woosley et al. (2021) for their SN Ib/Ic models.

As demonstrated by Khatami & Kasen (2019), their relation (shown as solid lines in Figure 30) provides a more accurate representation of the peak time-luminosity relation than Arnett’s rule (dotted lines). However, we notice that SNe with t_L^{peak} lower and greater than 15d are located systematically above and below the Khatami & Kasen (2019) relation, respectively, indicating that β varies significantly from one SN to another. This can be seen in the left-hand panel of Figure 31, which shows β for each SN computed with equation (12) against peak time. The β values range from -0.86 to 2.27 , and tend to decrease as t_L^{peak} decreases. In particular, eight SNe have $\beta \lesssim 0$ where β values ≤ 0 are physically meaningless. This, along with the fact that the distribution of our SNe in the peak time-luminosity space is not well described by equation (12) with a single β value, casts doubt on the usefulness of the Khatami & Kasen (2019) relation for estimating ^{56}Ni masses of SE SNe.

The second, third, and fourth rows of Figure 30 show the residuals of the Khatami & Kasen (2019) relation against decline rate, ejecta mass, and kinetic energy, respectively. We find strong correlations between residuals and decline rate for SNe I Ib ($r_p = 0.68$), SNe Ib ($r_p = 0.91$), SNe Ic ($r_p = 0.94$), and all SE SNe ($r_p = 0.89$), and between residuals and ejecta mass for SNe Ic ($r_p = -0.65$). On the other hand, the residuals for the models of Dessart et al. (2016) and

**Figure 31.** Empirical β values for SE SNe against peak time (left-hand panel) and decline rate (right-hand panel).

Woosley et al. (2021)¹⁰ show only a small variation with $\Delta m_{15}(\text{bol})$ or M_{ej} . The right-hand panel of Figure 31 shows β against decline rate, where we find strong correlations between both parameters (r_p of -0.67 , -0.91 , -0.94 , and -0.88 for SNe I Ib, Ib, Ic and all SE SNe, respectively). This confirms that β is not constant for SE SNe, but instead decreases with decline rate. Therefore, the Khatami & Kasen (2019) relation with a single β value is not very useful to estimate individual ^{56}Ni masses of SE SNe. Despite this, using an empirical average β value it would still be possible to estimate the mean ^{56}Ni mass of a SN sample but with a large error. Given the strength of the correlation between the observed residuals and decline rates for all SE SNe, we attempt to include the decline rate as an additional parameter in the calibration of the peak time-luminosity relation.

The top panel of Figure 32 shows the peak time-luminosity relation for SE SNe corrected for the decline rate, which we parameterize as

$$\log(L_{\text{peak}}/M_{\text{Ni}}) - b\Delta m_{15}(\text{bol}) = a - \log\left(\frac{t_L^{\text{peak}}}{10\text{d}}\right), \quad (60)$$

where $a = 0.571 \pm 0.020$, $b = 0.326 \pm 0.028$, and $\sigma_0 = 0.044$ dex. By applying the correction for decline rate, the $\hat{\sigma}$ value reduces from 0.141 dex (see top-right panel of Figure 30) to 0.061 dex. We also propose an alternative calibration for the peak time-luminosity relation uncorrected for decline rate, given by

$$\log(L_{\text{peak}}/M_{\text{Ni}}) = \log\left[\frac{2(1 + t_L^{\text{peak}}/t_*)}{(t_L^{\text{peak}}/t_*)^2}\right]. \quad (61)$$

¹⁰ Since Woosley et al. (2021) do not provide $\Delta m_{15}(\text{bol})$, we use their $\Delta m_{15}(V)$ values and the transformation $\Delta m_{15}(\text{bol}) = -0.10 + 0.93\Delta m_{15}(V)$ obtained with our SN sample.

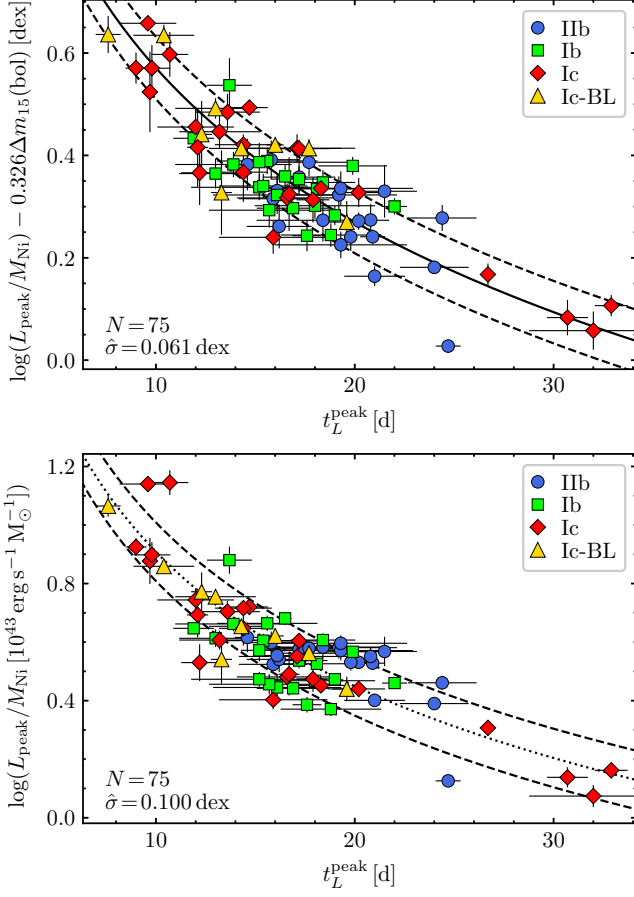


Figure 32. Peak time-luminosity relation for SE SNe, corrected (top panel) and uncorrected for decline rate (bottom panel). Solid and dotted lines are the best fits given by equations (60) and (61), respectively, while dashed lines are $\pm 1 \hat{\sigma}$ limits around the fits.

with $t_* = 15.74 \pm 0.28$ d, $\sigma_0 = 0.081$ dex, and $\hat{\sigma} = 0.100$ dex. This calibration, shown in the bottom-panel of Figure 32, is useful for those SNe without $\Delta m_{15}(\text{bol})$ estimates. We note that, in the peak time-luminosity relations shown in Fig. 32, the SNe classified as Ic-BL (yellow triangles) are not distinct from the rest of the SNe Ic.

Figure 33 shows the empirical peak time-luminosity relation for SE SNe corrected for decline rate (solid black line) along with the location of models of Dessart et al. (2016) and Woosley et al. (2021). We see that unlike the empirical relation, which decreases logarithmically with peak time, the $\log(L_{\text{peak}}/M_{\text{Ni}}) - 0.326\Delta m_{15}(\text{bol})$ estimates for models remain nearly constant with an average value of 0.138 ± 0.002 dex ($\hat{\sigma}/\sqrt{N}$ error). In the four-parameter space shown in the figure, models of Dessart et al. (2016) and Woosley et al. (2021) are consistent with observations only for SNe with $t_L^{\text{peak}} \sim 27$ d. Since 98% of the SNe in our sample have $t_L^{\text{peak}} < 27$ d,

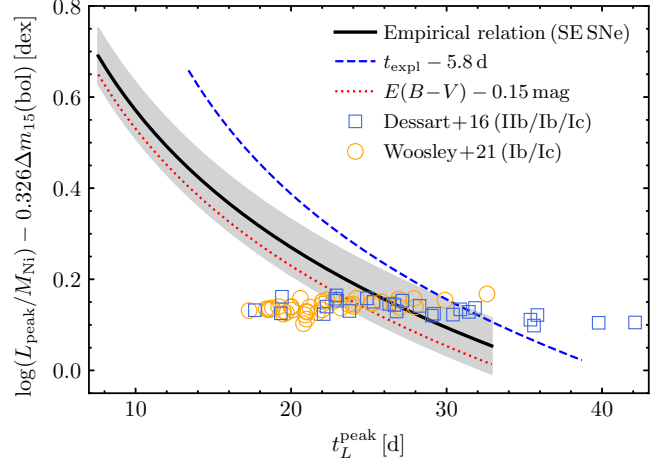


Figure 33. Empirical peak time-luminosity relation corrected for decline rate (solid black line) along with its $\pm 1 \hat{\sigma}$ region (gray region). The red dotted (blue dashed) line shows the effect on the empirical relation of decreasing $E(B - V)$ by 0.15 mag (t_{expl} by 5.8 d). Models of Dessart et al. (2016) and Woosley et al. (2021) are shown with empty symbols.

we can state that models of Dessart et al. 2016 and Woosley et al. 2021 in general overestimate (underestimate) M_{Ni} (L_{peak}) for SE SNe for a given peak time, decline rate, and peak luminosity (^{56}Ni mass). Note that if we reduce t_{expl} by 5.8 d to have an average t_L^{peak} for SNe Ib/Ic equal to that for models of Woosley et al. (2021) (see Table 9), then the empirical relation becomes steeper (blue dashed line) and the discrepancy between observations and models increases. The figure also shows the effect on the empirical relation of decreasing $E(B - V)$ by 0.15 mag (the median $E(B - V)$ of our SN sample), which produces a vertical displacement of only -0.04 dex. Therefore, the calibration of the peak time-luminosity relation is little affected by changes in $E(B - V)$.

4.3. ^{56}Ni mass distribution

4.3.1. Mean ^{56}Ni mass

The $\log M_{\text{Ni}}$ values computed with equation (60) or (61) ($\log M_{\text{Ni}}^{\text{peak}}$) are listed in Column 9 of Table F10. We adopt the weighted average of $\log M_{\text{Ni}}^{\text{peak}}$ and $\log M_{\text{Ni}}$ measured from the radioactive tail as the final $\log M_{\text{Ni}}$, which are collected in Column 10 of Table F10. The M_{Ni} values and their errors, given by

$$M_{\text{Ni}} = 10^{\log M_{\text{Ni}} + 0.5\phi} \quad (62)$$

and

$$\sigma_{M_{\text{Ni}}} = M_{\text{Ni}} \sqrt{10^\phi - 1} \quad (63)$$

respectively (Rodríguez et al. 2021) with $\phi = \ln(10)\sigma_{\log M_{\text{Ni}}}^2$, are listed in Column 11 of Table F10.

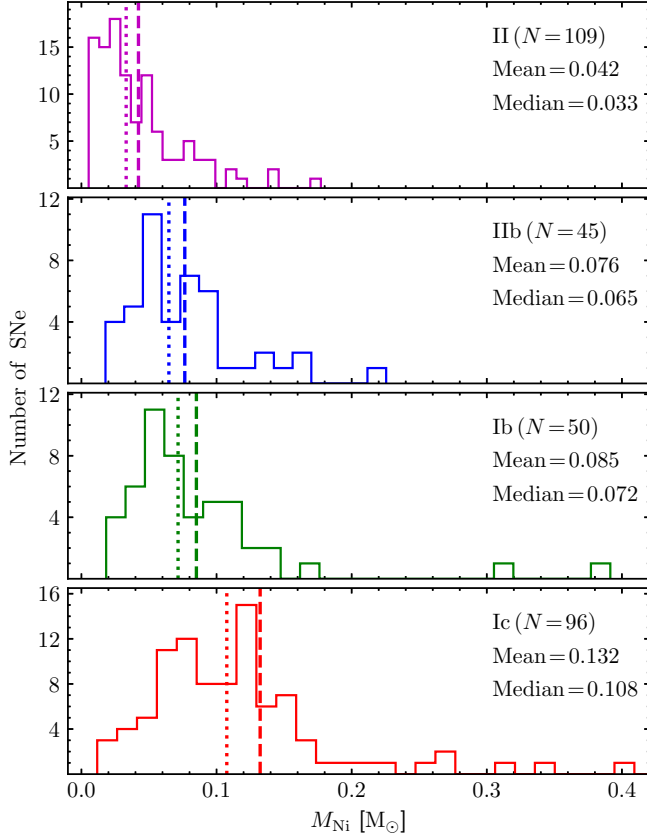


Figure 34. ^{56}Ni mass distribution for each SN subtype. Dashed and dotted lines indicate mean and median ^{56}Ni mass values, respectively. The four SN Ic events with ^{56}Ni masses between 0.45 and $0.70 M_{\odot}$ are not shown for clarity. For comparison, we include the distribution for the SN II sample of Rodríguez et al. (2021).

Figure 34 shows the M_{Ni} histograms for each SN subtype, while Table 11 summarizes the statistics of those distributions. To evaluate possible systematics on the derived mean M_{Ni} resulting from reddening effects, we re-compute the mean M_{Ni} using only SNe with E_{B-V} lower than the median E_{B-V} for each SN subtype (Column 9). The resulting mean values are consistent with the previous result to within 0.7σ . We also compare the mean M_{Ni} values with those computed using M_{Ni} from the peak (Column 10) and the radioactive tail (Column 11) luminosity. These estimates are again consistent at 1.3σ .

4.3.2. Selection bias correction

Our SN sample, collected from the literature and the ZTF BTS, is potentially affected by selection bias. To correct for this bias, we use the VL samples given in Section 3.5.4 as approximations for complete samples.

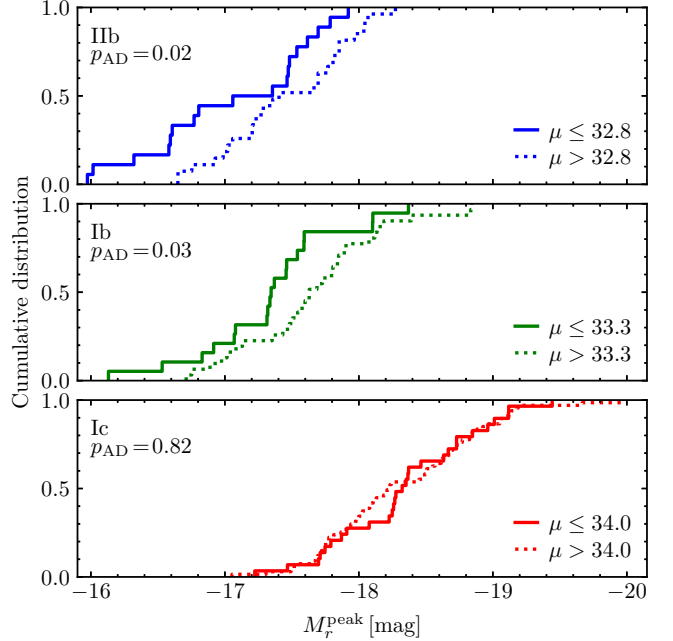


Figure 35. Cumulative distributions for the M_r^{peak} values in the volume-limited (solid lines) and non-volume-limited (dotted lines) samples.

Figure 35 shows the cumulative distributions for the M_r^{peak} values in the VL samples (solid lines) and those for the SNe at $\mu > \mu_{\text{VL}}$, which we refer as the non-VL (NVL) samples. Using the k -sample AD test we obtain p_{AD} values of 0.02, 0.03, and 0.82 for the VL and NVL M_r^{peak} distributions of SNe I Ib, Ib, and Ic, respectively. For SNe Ic the null hypothesis that the VL and NVL samples are drawn from a common M_r^{peak} distribution cannot be rejected at the 82% significance level, so we expect that the mean ^{56}Ni masses of the VL and NVL samples be statistically consistent between them. Indeed, the mean M_{Ni} values of the latter samples (0.116 ± 0.018 and $0.139 \pm 0.015 M_{\odot}$, respectively) are consistent within 1σ . We therefore adopt the mean ^{56}Ni mass of the full sample ($\langle M_{\text{Ni}} \rangle = 0.132 \pm 0.012 M_{\odot}$) as representative of a VL sample. In the case of SNe I Ib and Ib, the mean M_{Ni} value of the NVL sample is 2.5 and 2.0σ greater than for the VL sample, respectively, indicating the need for selection-bias correction.

To correct the SNe I Ib and Ib samples for selection bias, we proceed as in Rodríguez et al. (2021). First, we divide both the VL and the NVL sample into absolute magnitude groups, and assume that the brightest groups are less affected by selection bias. Then, in order to have the same ratio between the number of SNe in the brightest group (N_{bright}) and in a dimmer group (N_{dim}) for the VL and NVL sample, we have to include M dim

Table 11. Statistics of the ^{56}Ni mass distributions

Type	N	Min	Max	Median	Mean	$\hat{\sigma}$	σ	Mean		
								M_{Ni} with low E_{B-V} ^a	Peak M_{Ni}	Tail M_{Ni}
Iib	45	0.018	0.226	0.065	0.076	0.043	0.006	0.070 ± 0.007	0.077 ± 0.007	0.065 ± 0.006
Ib	50	0.018	0.391	0.072	0.085	0.065	0.009	0.095 ± 0.017	0.085 ± 0.009	0.091 ± 0.014
Ic	96	0.012	0.704	0.108	0.132	0.113	0.012	0.130 ± 0.018	0.135 ± 0.012	0.145 ± 0.026

NOTE—Values are in M_{\odot} units. $\sigma = \hat{\sigma}/\sqrt{N}$ is the standard error of the mean.

^aMean ^{56}Ni mass and σ error estimated with SNe having E_{B-V} lower than the median E_{B-V} .

SNe to the NVL sample, such that

$$\left(\frac{N_{\text{bight}}}{N_{\text{dim}}}\right)_{\text{VL}} = \left(\frac{N_{\text{bight}}}{N_{\text{dim}} + M}\right)_{\text{NVL}}. \quad (64)$$

In our case, given the low number of SNe in the VL samples, we divide the VL and NVL samples into two groups containing SNe brighter and dimmer than the mean M_r^{peak} value for the SNe in the VL samples (-17.059 for SNe Iib and -17.340 for SNe Ib). For SNe Iib (Ib) we obtain $N_{\text{bight}}/N_{\text{dim}}$ ratios of 10/8 (10/9) and 20/7 (24/7) for the VL and NVL sample, respectively. Therefore, following equation (64), we have to include 9 (15) dim SNe from the VL sample to the NVL sample of SNe Iib (Ib).

The mean ^{56}Ni mass corrected for selection bias can be written as

$$\langle M_{\text{Ni}} \rangle = \langle M_{\text{Ni}} \rangle_{\text{unc}} - \text{sbc}, \quad (65)$$

where sbc is the selection bias correction, given by

$$\text{sbc} = \frac{M}{N + M} (\langle M_{\text{Ni}} \rangle_{\text{unc}} - \langle M_{\text{Ni}} \rangle_M) \quad (66)$$

(Rodríguez et al. 2021), while $\langle M_{\text{Ni}} \rangle_{\text{unc}}$ and $\langle M_{\text{Ni}} \rangle_M$ are the mean ^{56}Ni mass computed with the full SN sample (of size N) and with the M dim SNe, respectively. Performing 10^5 simulations, where the M SNe are randomly selected from the VL dim sample, for SNe Iib and Ib we compute a sbc value of 0.010 ± 0.001 and $0.003 \pm 0.001 M_{\odot}$, respectively. Therefore for these two SN subtypes we obtain $\langle M_{\text{Ni}} \rangle$ estimates of 0.066 ± 0.006 and $0.082 \pm 0.009 M_{\odot}$, respectively.

We find that the $\langle M_{\text{Ni}} \rangle$ values for SNe Iib and Ib are consistent to within 1.5σ , and the individual M_{Ni} values may be drawn from a common distribution ($p_{\text{AD}} = 0.62$). This has been previously suggested by Afsariardchi et al. (2021) based on 8 SNe Iib and 8 SNe Ib. For SNe Ic we find that their $\langle M_{\text{Ni}} \rangle$ value is 4.9σ and 3.3σ greater than those of SNe Iib and

Ib, respectively. Specifically, we can reject the hypothesis that the M_{Ni} values of SNe Ib and Ic are drawn from a common distribution ($p_{\text{AD}} = 0.02$), contrary to the findings of Anderson (2019) and Afsariardchi et al. (2021). In the first work the author used a collection of ^{56}Ni masses generally measured with Arnett’s rule, and hence those estimates are suspect. In the second work, the results are based on small numbers (8 SNe Ib and 4 SNe Ic). We also compute $\langle M_{\text{Ni}} \rangle$ for SNe Ic-BL (26 SNe) and for Ic without Ic-BL (70 SNe), obtaining values of 0.138 ± 0.019 and $0.130 \pm 0.014 M_{\odot}$, respectively, that are consistent at 0.3σ . Thus, in terms of the ^{56}Ni mass, there is no systematic difference between SNe Ic-BL and other SNe Ic.

Our $\langle M_{\text{Ni}} \rangle$ values for SNe Iib, Ib, and Ic are 1.8, 2.2, and 3.6 times greater, respectively, than the value for SNe II reported by Rodríguez et al. (2021) ($0.037 \pm 0.005 M_{\odot}$) at significance levels of 3.7σ , 4.4σ , and 7.3σ , respectively. This finding is again consistent with previous works (e.g. Kushnir 2015; Anderson 2019; Meza & Anderson 2020; Sharon & Kushnir 2020; Rodríguez et al. 2021; Afsariardchi et al. 2021).

4.4. Mean iron yield

Using the relative fractional SN rates provided in Shivvers et al. (2017), the mean ^{56}Ni mass of SE and CC SNe is given by

$$\langle M_{\text{Ni}} \rangle_{\text{SE}} = 0.36 \langle M_{\text{Ni}} \rangle_{\text{Iib}} + 0.356 \langle M_{\text{Ni}} \rangle_{\text{Ib}} + 0.284 \langle M_{\text{Ni}} \rangle_{\text{Ic}} \quad (67)$$

and

$$\langle M_{\text{Ni}} \rangle_{\text{CC}} = 0.696 (\pm 0.067) \langle M_{\text{Ni}} \rangle_{\text{II}} + 0.304 (\pm 0.05) \langle M_{\text{Ni}} \rangle_{\text{SE}}, \quad (68)$$

respectively. With our $\langle M_{\text{Ni}} \rangle$ estimates for SNe Iib, Ib, and Ic, and $\langle M_{\text{Ni}} \rangle_{\text{II}} = 0.039 \pm 0.005 M_{\odot}$ (which includes long-rising and CSM-interacting SNe) reported in Rodríguez et al. (2021), we obtain $\langle M_{\text{Ni}} \rangle_{\text{SE}}$ and $\langle M_{\text{Ni}} \rangle_{\text{CC}}$ of 0.090 ± 0.005 and $0.055 \pm 0.006 M_{\odot}$, respectively. Of the mean ^{56}Ni mass produced by CC SNe,

50% is produced by SE SNe and 50% by SNe II. Finally, assuming a M_{Fe} to M_{Ni} ratio of 1.07 ± 0.04 (e.g. [Rodríguez et al. 2021](#)), we obtain a mean iron yield of 0.097 ± 0.007 and $0.058 \pm 0.007 M_{\odot}$ for SE and CC SNe, respectively. Our mean iron yield for CC SNe is 22% lower than the estimate of $0.074 M_{\odot}$ that [Maoz & Graur \(2017\)](#) derived, based on previous estimates of $\langle M_{\text{Ni}} \rangle$ for the various SN types.

The distances we have used in this work and those used in [Rodríguez et al. \(2021\)](#) are based on a Cepheid-calibrated Hubble parameter $H_0 = 74 \text{ km s}^{-1} \text{ Mpc}^{-1}$. For a different choice of H_0 , our ^{56}Ni mass and iron yield measurements will scale as $(74/H_0)^2$.

5. DISCUSSION

5.1. Comparison with other works

We now compare the M_{Ni} values we have computed from the radioactive tail ($M_{\text{Ni}}^{\text{tail}}$) with ^{56}Ni masses reported in the literature. We do not include SN samples with ^{56}Ni masses computed from pseudo-bolometric light curves (e.g. [Cano 2013](#); [Prentice et al. 2019](#); [Meza & Anderson 2020](#)) because, given that those light curves are not corrected for the unobserved UV and IR flux, the inferred M_{Ni} values are in principle lower limits. From the literature we select ^{56}Ni masses reported by [Prentice et al. \(2016\)](#) and [Lyman et al. \(2016\)](#), computed with Arnett’s rule and the Arnett model, respectively, the M_{Ni} values computed with the [Khatami & Kasen \(2019\)](#) relation (K&K) by [Afsariardchi et al. \(2021\)](#), and the $M_{\text{Ni}}^{\text{tail}}$ estimates reported by [Sharon & Kushnir \(2020\)](#) and [Afsariardchi et al. \(2021\)](#). In [Prentice et al. \(2016\)](#), peak luminosities were calculated using fluxes integrated over bands from u/U to K and assuming a 10% contribution from the unobserved UV and IR flux, while ^{56}Ni masses were computed with Arnett’s rule. In [Lyman et al. \(2016\)](#), luminosities were estimated with the BC technique and the BC calibration of [Lyman et al. \(2014, 2016\)](#), while the ^{56}Ni masses were estimated with an updated version of the Arnett model given by [Valenti et al. \(2008a\)](#). In [Sharon & Kushnir \(2020\)](#), luminosities were calculated via flux integration over bands from u/U to H/K , along with corrections for the missing UV and IR flux. To compute $M_{\text{Ni}}^{\text{tail}}$, [Sharon & Kushnir \(2020\)](#) replaced the deposition function (equation 6) with a more versatile function (with two free parameters). In [Afsariardchi et al. \(2021\)](#), luminosities were estimated with the BC technique and the BC calibration of [Lyman et al. \(2014, 2016\)](#). To calculate ^{56}Ni masses with the K&K relation, [Afsariardchi et al. \(2021\)](#) used their empirically calibrated β values for each SN subtype, while to com-

pute $M_{\text{Ni}}^{\text{tail}}$ the authors neglected the term describing the escape of positrons (equation 5). In addition, 20 SNe in the present work have ^{56}Ni masses estimated by comparing hydrodynamical models with bolometric light curves (16 SNe) or pseudo-bolometric light curves with fluxes integrated from u/U to K (SNe 1993J, 1994I, 2008D, and 2011fu). These SNe, along with the reported μ , E_{B-V}^{MW} , E_{B-V} , R_V , t_{expl} , L_{peak} , and inferred ^{56}Ni masses are collected in Table F11. For the comparison with the M_{Ni} values from the literature, we rescale our $M_{\text{Ni}}^{\text{tail}}$ values using the distances, reddenings, and explosion epochs adopted in the respective works. For the comparison we also have to compensate for differences in luminosity due to differences in the techniques used to calculate luminosity. For this, we divide our $M_{\text{Ni}}^{\text{tail}}$ values by the ratio of L_{peak} from the literature to our L_{peak} values (which we rescale using the distances and reddenings from the literature).

Figure 36 shows the ratios of the ^{56}Ni masses computed in the literature with the methods mentioned above to the $M_{\text{Ni}}^{\text{tail}}$ values estimated here, against peak times. The median ratios of the $M_{\text{Ni}}^{\text{tail}}$ values ($\hat{\sigma}$ values) reported by [Sharon & Kushnir \(2020\)](#) ($N = 10$) and [Afsariardchi et al. \(2021\)](#) ($N = 24$) to those estimated here are of 1.11 (0.20) and 0.96 (0.21), respectively. Our $M_{\text{Ni}}^{\text{tail}}$ estimates are, on average, consistent to within $1\hat{\sigma}/\sqrt{N}$ with those computed with the methodology of [Afsariardchi et al. \(2021\)](#). The $M_{\text{Ni}}^{\text{tail}}$ values of [Sharon & Kushnir \(2020\)](#) are, on average, $1.7\hat{\sigma}/\sqrt{N}$ greater than our estimates. This difference, which is due to the deposition function adopted by [Sharon & Kushnir \(2020\)](#), will be discussed further in Section 5.3.2. The median ratio of the ^{56}Ni masses computed with the K&K relation by [Afsariardchi et al. \(2021\)](#) ($N = 24$) to our $M_{\text{Ni}}^{\text{tail}}$ estimates is of 0.98, which is consistent with unity. This is expected because the β values used by [Afsariardchi et al. \(2021\)](#) to compute M_{Ni} were empirically calibrated against $M_{\text{Ni}}^{\text{tail}}$. We see, however, that the K&K relation tends to overestimate (underestimate) the ^{56}Ni masses of SNe with peak times lower (greater) than 18 d, which is expected given that the peak time-luminosity relation of SE SNe is not well described by the [Khatami & Kasen \(2019\)](#) relation (see Section 4.2).

In the bottom panels of Figure 36 we see that the ^{56}Ni mass ratios for Arnett’s rule ($N = 22$), the Arnett model ($N = 23$), and hydrodynamical models ($N = 22$) are greater than unity, and tend to increase as peak times decrease. This behavior in the case of Arnett’s rule can also be seen in top panels of Figure 30, where the difference between the observed $\log(L_{\text{peak}}/M_{\text{Ni}})$ values and Arnett’s rule is greater for SNe with short peak

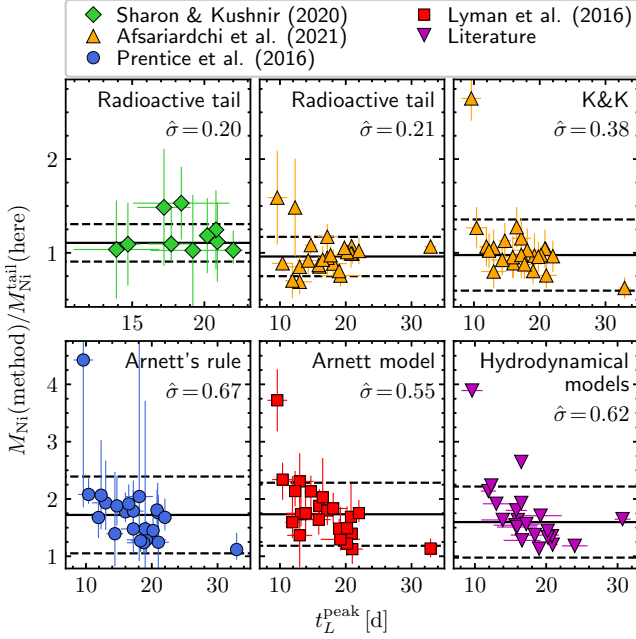


Figure 36. Ratios of the ^{56}Ni masses estimated with different methods in the literature to our recalibrated $M_{\text{Ni}}^{\text{tail}}$ values against peak time. Solid lines are median values, dashed lines are $\pm 1 \hat{\sigma}$ limits, and error bars are 1σ errors.

times. The median ^{56}Ni mass ratios ($\hat{\sigma}$ values) for the three methods mentioned above are of 1.72 (0.67), 1.73 (0.55) and 1.60 (0.62), respectively, which are at least $4.5 \hat{\sigma}/\sqrt{N}$ greater than unity. This indicates that the Arnett model and Arnett’s rule systematically overestimate the ^{56}Ni mass of SE SNe typically by 70%, while hydrodynamical models typically overestimate it by 60%. To quantify more accurately the typical overestimation of M_{Ni} by Arnett’s rule, we estimate ^{56}Ni masses using $M_{\text{Ni}} = L_{\text{peak}}/(q_{\gamma}(t_L^{\text{peak}}) + q_{\text{pos}}(t_L^{\text{peak}}))$ and our t_L^{peak} and $\log L_{\text{peak}}$ values listed in Table F10, and compare them with our $M_{\text{Ni}}^{\text{tail}}$ estimates. We find a median ^{56}Ni mass ratio of 1.72 ± 0.06 ($\hat{\sigma}/\sqrt{N}$ error), which is equal to our previous estimate and confirms that Arnett’s rule overestimate M_{Ni} of SE SNe typically by 70%. We also find a mean ^{56}Ni mass ratio of 1.77 ± 0.06 , which is lower than the average overestimation factor of ~ 2 found by Afsariardchi et al. (2021) from observations, and greater than the average overestimation factor of 1.30–1.41 suggested by Dessart et al. (2016) and Woosley et al. (2021) based on their models.

Table 12 summarizes the mean ^{56}Ni masses (uncorrected for selection bias) we obtain for SNe IIb, Ib, Ic without Ic-BL, and Ic-BL, along with the values reported by Prentice et al. (2019), Anderson (2019), and Afsariardchi et al. (2021). In these three works, respectively, the authors computed mean ^{56}Ni masses using the largest samples of SE SNe to date with ^{56}Ni masses com-

Table 12. Mean ^{56}Ni masses reported in the literature.

Type	N	Mean M_{Ni} (M_{\odot})	N	Mean M_{Ni} (M_{\odot})
			This work	
IIb	45	0.076 ± 0.006	8	0.060 ± 0.007
Ib	50	0.085 ± 0.009	8	0.110 ± 0.039
Ic	70	0.130 ± 0.014	4	0.200 ± 0.110
Ic-BL	26	0.138 ± 0.019	7	0.150 ± 0.026
			Anderson (2019)	
IIb	27	0.124 ± 0.012	21	0.070 ± 0.030
Ib	33	0.199 ± 0.025	25	0.090 ± 0.060
Ic	48	0.198 ± 0.020	19	0.110 ± 0.090
Ic-BL	32	0.507 ± 0.072	11	0.150 ± 0.070

NOTE—Uncertainties are the standard error of the mean. SNe Ic do not include SNe Ic-BL.

puted from SNe analyzed homogeneously (80 SNe), with M_{Ni} values collected from the literature (143 SNe), and with $M_{\text{Ni}}^{\text{tail}}$ estimates (27 SNe). Our mean ^{56}Ni masses are statistically consistent to those of Afsariardchi et al. (2021), while the mean ^{56}Ni masses of Anderson (2019) are 1.5–3.7 times larger than our estimates. This is in part because the ^{56}Ni masses collected and used by Anderson (2019) were generally estimated with Arnett’s rule. We find a good agreement between our mean values and those of Prentice et al. (2019), even though their M_{Ni} estimates were computed with Arnett’s rule and the Arnett model, which overestimate M_{Ni} typically by 70%. This is because the L_{peak} estimates of Prentice et al. (2019), which only include fluxes in the wavelength range 400–1000 nm, are on average 1.71 times lower than our L_{peak} values. Therefore, the underestimated L_{peak} values and the overestimated ^{56}Ni masses in Prentice et al. (2019) offset each other, resulting in mean ^{56}Ni masses which are, on average, similar to our results.

5.2. Comparison with neutrino-driven explosion models

Various neutrino-driven explosion models have predicted maximum possible values for the synthesized ^{56}Ni mass in CC SN explosions, of 0.15 to $0.226 M_{\odot}$ (e.g. Ugliano et al. 2012; Pejcha & Thompson 2015; Sukhbold et al. 2016; Suwa et al. 2019; Ertl et al. 2020; Woosley et al. 2021). Although in our sample there are some SNe with ^{56}Ni masses 1σ greater than these theoretical limits, we include them when computing mean ^{56}Ni masses, as there is no observational evidence supporting the existence of such upper limits (e.g.

differences in any other characteristics of such high-yield SNe). Based on spherically symmetric neutrino-driven explosion models, Woosley et al. (2021) reported an IMF-averaged ^{56}Ni yield of $0.09 M_{\odot}$ for models consistent with SNe Ib/Ic (excluding SNe Ic-BL), whose M_{Ni} do not exceed $0.15 M_{\odot}$. In our sample, there are two SNe Ib and five SNe Ic (excluding SNe Ic-BL) with ^{56}Ni masses exceeding $0.15 M_{\odot}$ by $> 1\sigma$. If we nonetheless exclude those events, we obtain mean ^{56}Ni masses of 0.074 ± 0.005 and $0.105 \pm 0.008 M_{\odot}$ for SNe Ib and Ic, respectively. Accounting for their relative rates (see Section 4.1), for SNe Ib/Ic we obtain a mean M_{Ni} of $0.086 \pm 0.004 M_{\odot}$, which is consistent with the value reported by Woosley et al. (2021).

5.3. Systematics

5.3.1. Sample completeness

In Section 4.3.2 we used VL samples as a reference to evaluate the selection bias correction. However, a volume-limited sample is merely an approximation for a complete sample. In particular, our VL samples could underestimate the fraction of faint ($M_r^{\text{peak}} > -16.5$) SNe IIb/Ib due to Malmquist bias. In addition, Ouchi et al. (2021) show that if SE SNe with $M_{\text{Ni}} < 0.01$ (corresponding to $M_r^{\text{peak}} > -15.5$) exist, then they will be missing from samples collected from the literature. If the fraction of faint SE SNe is intrinsically low, then their omission from the sample should not have a severe effect on the mean ^{56}Ni and iron yields. However, if faint SE SNe are actually common, then the mean ^{56}Ni and iron yields we report should be considered upper limits.

Recently, Rodríguez (2022) computed progenitor luminosities (L_{prog}) for a sample of 112 SNe II and compared them to the luminosities of red supergiants (RSGs, identified as the progenitors of SNe II, e.g. Smartt et al. 2009) in LMC, SMC, M31, and M33. In particular, after correcting for selection bias, Rodríguez (2022) found a smaller fraction of SN II with $L_{\text{prog}} < 10^{4.6} L_{\odot}$ compared to RSG samples. This is most likely because the VL sample used to evaluate the selection bias correction is not complete for low-luminosity SNe II. Given that these SNe produce a low amount of ^{56}Ni and given that the SN sample of Rodríguez (2022) is virtually identical to that of Rodríguez et al. (2021), the mean ^{56}Ni mass we adopted for SNe II and the $\langle M_{\text{Ni}} \rangle_{\text{CC}}$ value we compute are potentially overestimated. To roughly quantify this overestimation, we calculate the fraction of missing SNe II with $L_{\text{prog}} < 10^{4.6} L_{\odot}$ in the selection-bias corrected sample of Rodríguez (2022) by assuming that all RSGs with luminosity between $10^{4.361}$ and $10^{5.091} L_{\odot}$ (the minimum and maximum L_{prog} value in the SN sample of Rodríguez 2022, respectively) explode as SNe II.

Using the the RSG samples used in Rodríguez (2022), we find that the fraction of missing low-luminosity SNe II is 0.29, while the mean ^{56}Ni mass of the SNe II with $L_{\text{prog}} < 10^{4.6} L_{\odot}$ is $0.011 M_{\odot}$. Therefore, if all RSGs with luminosity between $10^{4.361}$ and $10^{5.091} L_{\odot}$ indeed explode as SNe II, then the mean ^{56}Ni mass for SNe II is reduced by $0.008 M_{\odot}$, while our $\langle M_{\text{Ni}} \rangle_{\text{CC}}$ value reduces by $0.0057 M_{\odot}$. Since the possible overestimation of $\langle M_{\text{Ni}} \rangle_{\text{CC}}$ is similar to the $\langle M_{\text{Ni}} \rangle_{\text{CC}}$ error of $0.006 M_{\odot}$, this uncertainty do not have a severe effect on the mean ^{56}Ni and iron yields of CC SNe.

5.3.2. Deposition function

An important assumption we make in this work is that the deposition function of SE SNe is well represented by the formula of Clocchiatti & Wheeler (1997) (equation 6, hereafter $f_{\text{dep}}^{\text{C\&W}}$), which was derived analytically under simplistic but reasonable assumptions (at least to first order). Recently, Sharon & Kushnir (2020) proposed

$$f_{\text{dep}}^{\text{S\&K}}(t, t_{\text{esc}}, n) = (1 + (t/t_{\text{esc}})^n)^{-2/n} \quad (69)$$

as a more appropriate deposition function for SNe. This function is more versatile than $f_{\text{dep}}^{\text{C\&W}}$ because it includes a second free parameter, n , which controls the sharpness of the transition between regions optically thick ($f_{\text{dep}} = 1$) and thin ($f_{\text{dep}} = (t_{\text{esc}}/t)^2$ for $t \gg t_{\text{esc}}$) to γ -rays. To evaluate whether $f_{\text{dep}}^{\text{S\&K}}$ provides a better fit to observations in the radioactive tail than $f_{\text{dep}}^{\text{C\&W}}$, we compute $\log M_{\text{Ni}}^{\text{tail}}$ using the methodology described in Section 3.1.1 with $f_{\text{dep}}^{\text{S\&K}}$ as deposition function, and compare the $\hat{\sigma}$ estimates around the $\log M_{\text{Ni}}^{\text{tail}}$ values that maximize the posterior probability ($\hat{\sigma}_{\log M_{\text{Ni}}^{\text{tail}}}$, e.g. the $\hat{\sigma}$ value in the bottom panel of Figure 25) with the $\hat{\sigma}$ estimates computed with $f_{\text{dep}}^{\text{C\&W}}$. Among the 67 SNe that require the inclusion of a deposition function, 28 of them have $n \leq 1$, which is not a reasonable value because the derivative of equation (69) diverges at $t \rightarrow 0$ (see Sharon & Kushnir 2020).

The left-hand panel of Figure 37 shows the $\hat{\sigma}_{\log M_{\text{Ni}}^{\text{tail}}}$ values for the ^{56}Ni masses computed using $f_{\text{dep}}^{\text{S\&K}}$ against those calculated using $f_{\text{dep}}^{\text{C\&W}}$ for the 39 SNe with $n > 1$. We find that the distribution can be expressed as a straight line with a slope of unity and a y -intercept of 0.001 dex, meaning that the $\hat{\sigma}_{\log M_{\text{Ni}}^{\text{tail}}}$ values for the ^{56}Ni masses computed using $f_{\text{dep}}^{\text{S\&K}}$ are slightly greater than those calculated with $f_{\text{dep}}^{\text{C\&W}}$. Therefore, for SE SNe with $n > 1$, $f_{\text{dep}}^{\text{S\&K}}$ fits observations in the radioactive tail as well as, but not better than, $f_{\text{dep}}^{\text{C\&W}}$.

The right-hand panel of Figure 37 shows the ratios of the $M_{\text{Ni}}^{\text{tail}}$ values calculated with $f_{\text{dep}}^{\text{S\&K}}$ to those computed with $f_{\text{dep}}^{\text{C\&W}}$ against n . The observed dependence

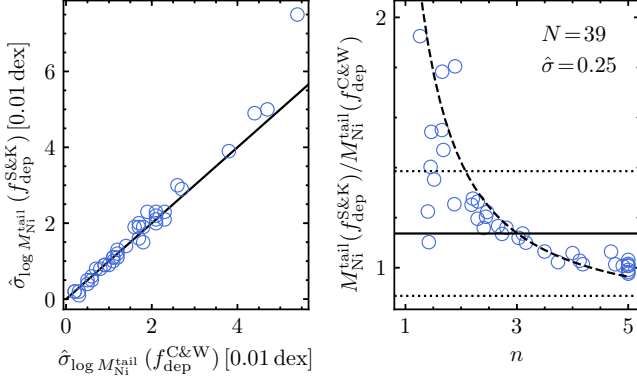


Figure 37. Left: $\hat{\sigma}$ values of the $\log M_{\text{Ni}}^{\text{tail}}$ estimates calculated with $f_{\text{dep}}^{\text{S\&K}}$ against those computed with $f_{\text{dep}}^{\text{C\&W}}$ for 39 SNe with $n > 1$. The solid line is a one-to-one correspondence. Right: ratios of the ^{56}Ni masses estimated with $f_{\text{dep}}^{\text{S\&K}}$ to those computed with $f_{\text{dep}}^{\text{C\&W}}$ against n . The solid line is the median value and dotted lines are $\pm 1\hat{\sigma}$ limits. The dashed line is $f_{\text{dep}}^{\text{C\&W}}/f_{\text{dep}}^{\text{S\&K}}$ with $t_{\text{esc}}/t = 1.37$ for $f_{\text{dep}}^{\text{C\&W}}$ and $t_{\text{esc}}/t = 1.22$ for $f_{\text{dep}}^{\text{S\&K}}$.

of these ratios on n , especially for $n > 2$, arises because in the radioactive tail $L \approx M_{\text{Ni}} q_{\gamma} f_{\text{dep}}$ (equations 1–3), so the ^{56}Ni mass ratio is $\approx f_{\text{dep}}^{\text{C\&W}}/f_{\text{dep}}^{\text{S\&K}}$. Indeed, the distribution is close to $f_{\text{dep}}^{\text{C\&W}}/f_{\text{dep}}^{\text{S\&K}}$ (dashed line) with $t_{\text{esc}}/t = 1.37$ for $f_{\text{dep}}^{\text{C\&W}}$ and $t_{\text{esc}}/t = 1.22$ for $f_{\text{dep}}^{\text{S\&K}}$, corresponding to the median t_{esc}/t values for the 39 SNe with $n > 1$. The median ^{56}Ni mass ratio is 1.14 ± 0.04 ($\hat{\sigma}/\sqrt{N}$ error), which is consistent with the overestimation factor that we obtain in Section 5.1 and indicates that $M_{\text{Ni}}^{\text{tail}}$ values computed with $f_{\text{dep}}^{\text{S\&K}}$ are typically 14% greater than those computed with $f_{\text{dep}}^{\text{C\&W}}$. In the case that $f_{\text{dep}}^{\text{S\&K}}$ is the true deposition function of SE SNe, then our $\langle M_{\text{Ni}} \rangle_{\text{CC}}$ estimate increases by $0.004 M_{\odot}$, which is lower than the $\langle M_{\text{Ni}} \rangle_{\text{CC}}$ error of $0.006 M_{\odot}$. Thus, a systematic uncertainty of 14% on ^{56}Ni mass due to the adopted deposition function does not have a severe effect on the the mean ^{56}Ni and iron yields of CC SNe.

5.4. Implications for radioactive ^{56}Ni -powered models

As we found in Section 5.1, the Arnett model, Arnett’s rule, and hydrodynamical models typically overestimate the ^{56}Ni masses of SE SNe by a factor of 1.60–1.73, so these models underestimate L_{peak} for a given ^{56}Ni mass typically by 60–70%. In addition, as mentioned in Section 4.2, models of Dessart et al. (2016) and Woosley et al. (2021) underestimate L_{peak} for a given ^{56}Ni mass, decline rate, and peak time. In particular, for a median t_L^{peak} of 15.9 d (the median for our SN sample), these models underestimate L_{peak} typically by 70%. Given that the Arnett model, Arnett’s rule, hydrodynamical models used in the references listed in Table F11, and models of Dessart et al. (2016) and

Woosley et al. (2021) assume that the SN light curves at peak are powered only by the radioactive ^{56}Ni decay chain, we can state that radioactive ^{56}Ni -powered models typically underestimate peak luminosities for SE SNe by 60–70%.

A more direct way to evaluate whether a given set of models underestimates the light at peak is by comparing the absolute magnitude of the brightest model with those of observed SE SNe. In the case of the SN Ib/Ic models of Woosley et al. (2021), the brightest model have $M_r^{\text{peak}} = -17.8$ mag (e.g. Sollerman et al. 2022). Among the 48 SNe Ib and 65 SNe Ic (without Ic-BL) in our sample with M_{Ni} that not exceed $0.15 M_{\odot}$ by $> 1\sigma$, 27% and 71% have $M_r^{\text{peak}} < -17.8$, respectively, while if we use only SNe with E_{B-V} lower than the median E_{B-V} for each SN subtype, the percentages reduces to 17% and 56%, respectively. This indicates that an important fraction of SNe Ib and Ic are brighter than predicted by the models of Woosley et al. (2021). To estimate lower limits for these fractions, we use M_r^{peak} values uncorrected for host-galaxy reddening ($M_{r,\text{unc}}^{\text{peak}}$), finding 6 SNe Ib and 14 SNe Ic with $M_{r,\text{unc}}^{\text{peak}} < -17.8$. Therefore, at least 12% of SNe Ib and 22% of SNe Ic are brighter than predicted by the models of Woosley et al. (2021). These percentages are lower than the 36% reported by Sollerman et al. (2022), which is most likely due to their sample is more affected by selection bias than our sample.

It is important to note that the Khatami & Kasen (2019) relation does not depend only on β but also, and most importantly, on the heating source. For the analysis of SE SNe, in this work and in the literature (e.g. Khatami & Kasen 2019; Afsariardchi et al. 2021; Woosley et al. 2021) the radioactive ^{56}Ni decay chain is adopted as heating source. Therefore, the accurate fit of the Khatami & Kasen (2019) relation to the peak time-luminosity relation for the numerical models of Dessart et al. (2016) and Woosley et al. (2021) with a single β value (e.g. Figure 15 of Khatami & Kasen 2019 and Figure A1 of Woosley et al. 2021) is expected because those models are powered by the radioactive ^{56}Ni decay chain. The fact that the Khatami & Kasen (2019) relation for radioactive ^{56}Ni -powered transients with a single β value does not fit observations suggests that SE SNe at peak may not be powered only by the radioactive ^{56}Ni decay chain. This evidence, along with the fact that radioactive ^{56}Ni -powered models typically underestimate peak luminosities suggests the possible presence of an additional power source contributing to the luminosity of SE SNe at peak. In Rodríguez et al. (2023) we use the bolometric light curves and ^{56}Ni masses computed in this work to show that, in all or most SE SNe,

a central engine in addition to radioactive ^{56}Ni decay operates on timescales of hours to days after the explosion. The central engine contributes significantly to the luminosity at those times, and its properties appear consistent with those of magnetars.

5.5. Reddening versus EW_{NaID} relation

The top panel of Figure 38 shows the E_{B-V} versus EW_{NaID} relation we obtained in Section 3.5 for SE SNe (blue solid line) together with the relation of Poznanski et al. (2012) for the MW (red line) for $EW_{\text{NaID}} < 1 \text{ \AA}$. The panel also shows the MW Na ID EWs reported by Poznanski et al. (2012) for a sample of high-resolution spectra of quasars (QSOs) and their MW reddenings from Schlafly & Finkbeiner (2011) (orange squares). Our relation for SE SNe provides E_{B-V} values on average 0.05 mag higher than those calculated with the Poznanski et al. (2012) relation. We also see that almost all MW values for the QSO sample are below our relation for SE SNe, indicating a systematic difference between the latter relation and that of the MW. To evaluate a possible underestimation of our EW_{NaID} values computed from low-resolution spectra (e.g. due to contamination by host galaxy light, Poznanski et al. 2011), we also measure MW Na ID EWs from the same spectra (Column 2 of Table F7). Those values along with the respective MW reddenings (Column 4 of Table F1) are plotted in the panel as green circles. To represent the dependence of MW reddening on EW_{NaID} we use the linear relation $E_{B-V} = a + b EW_{\text{NaID}} [\text{\AA}]$, whose parameters for the QSO and SE SN samples are listed in Table 13. For both samples we find strong correlations ($r_P \approx 0.6$ and $p_P < 0.001$) with parameters consistent within their errors. This means that our EW_{NaID} measurements from low-resolution spectra are consistent with those computed by Poznanski et al. (2012) from high-resolution spectra.

We have repeated the above analysis, but now using the SN II sample of Rodríguez et al. (2021). The bottom panel of Figure 38 shows the MW (green circles) and SN II (blue diamonds) reddenings against their respective Na ID EWs, measured here from SN II spectra (values reported in Table F12). We find a strong correlation between E_{B-V} and EW_{NaID} for the MW and SNe II, whose parameters are listed in Table 13. The parameters of the MW relation computed with the SN II sample are consistent within their errors with those calculated with the QSO and SE SNe samples. Combining those three samples we obtain a slope of 0.048 ± 0.005 for the MW E_{B-V} versus EW_{NaID} relation, which is 3.0σ and 3.6σ lower than the slope for SNe II and SE SNe, re-

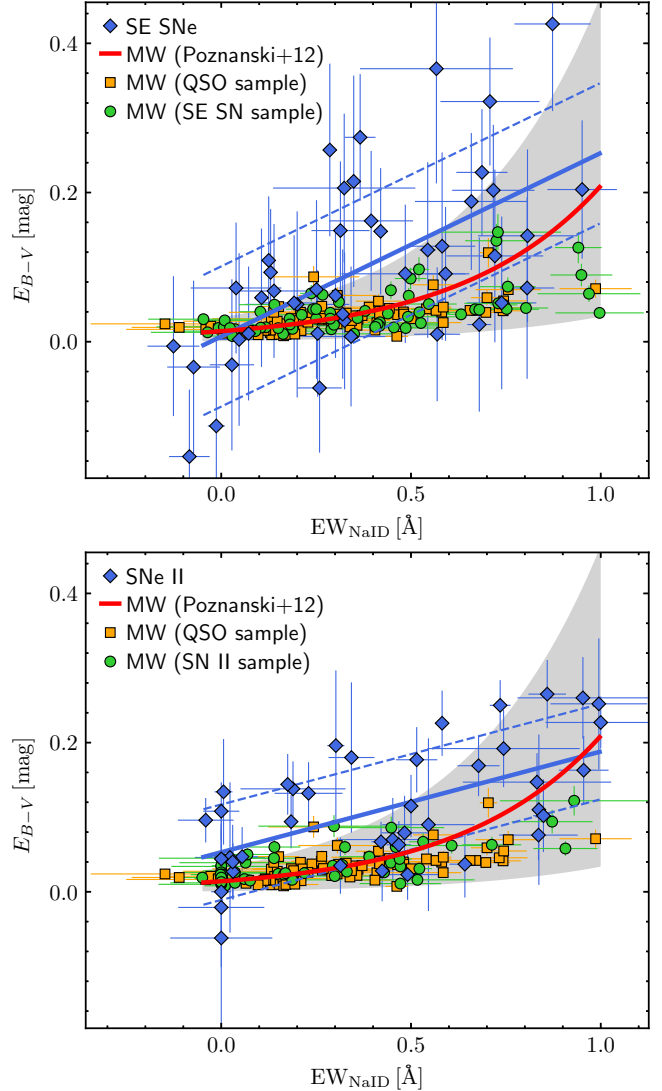


Figure 38. Top panel: MW (green circles) and SE SN (blue diamonds) reddenings against their respective Na ID EWs measured from SE SN spectra. The blue solid line is the E_{B-V} versus EW_{NaID} relation for SE SNe, while dashed lines are the $\pm 1 \sigma$ limits. Bottom panel: similar to the top panel but for SNe II instead of SE SNe. The red line and the gray region are the relation between MW reddening and EW_{NaID} reported by Poznanski et al. (2012) and its $\pm 1 \sigma$ region, respectively. Orange squares are the MW reddenings and EW_{NaID} values for the QSO sample of Poznanski et al. (2012). Error bars are 1σ errors.

spectively. If we use $R_V = 3.1$ to compute E_{B-V} in Section 3.5, the slope of the relation for SE SNe reduces to 0.234 ± 0.055 , which is 3.4σ greater than the slope for the MW. Since the methods to compute E_{B-V} for SE SNe and SNe II are systematically different, we can reject the possibility that the steeper relation between E_{B-V} and EW_{NaID} for SNe II and SE SN compared to that of the MW is due to an overestimation of the SN reddenings.

Table 13. E_{B-V} versus EW_{NaID} relation parameters

Dust source ^a	N	a	b	$\hat{\sigma}$	r_P
MW (QSOs)	86	0.014(2)	0.048(6)	0.015	0.64
MW (SE SNe)	62	0.018(3)	0.050(10)	0.024	0.61
MW (SNe II)	54	0.019(2)	0.055(9)	0.018	0.68
MW (All)	202	0.017(1)	0.048(5)	0.019	0.63
SN II hosts	41	0.053(14)	0.135(28)	0.065	0.62
SE SN hosts	45	0.007(24)	0.246(54)	0.094	0.60

NOTE—Numbers in parentheses are 1σ errors in units of 0.001.

^aFor the MW, in parentheses are indicated the spectra used to measure EW_{NaID} .

The evidence therefore suggests higher dust-to-gas ratios and/or lower neutral sodium to total gas ratios for regions where SE SNe and SNe II explode, compared to the diffuse interstellar medium of our Galaxy. For this reason, the relation of [Poznanski et al. \(2012\)](#) should not be used to measure E_{B-V} from EW_{NaID} for SE SNe and SNe II. Instead, we recommend using equation (30) and $E_{B-V} = 0.053 + 0.135 EW_{\text{NaID}}[\text{\AA}]$, respectively.

5.6. LSST

Within a few years, the Rubin Observatory Legacy Survey of Space and Time (LSST) will become the main source of photometric transient and variable data. Given the large number of CC SNe that are expected to be discovered per year (around 10^5 , [Lien & Fields 2009](#)), light-curve classifiers will be required to determine the class of those transients. In the case of SE SNe, current light-curve classifiers achieve an accuracy of 50% for the ZTF (light curves in two bands sampled with a cadence of 3 d, [Sánchez-Sáez et al. 2021](#)) and of 74% for light curves in four bands sampled with a cadence of 7–10 d ([Takahashi et al. 2020](#)). A contamination of about 25% is clearly not negligible. Therefore, if the classification accuracy does not improve much for the LSST (which will observe with six non-coeval photometric bands, with a cadence that is yet to be decided), then the number of SNe from LSST useful to improve the mean iron yield of SE SNe will be limited by the capability of carrying out spectroscopic classifications.

6. CONCLUSIONS

We have carried out a systematic analysis of 191 SE SN events, with the aim to estimate the mean ^{56}Ni and iron yields of SE SNe, and of CC SNe in general. We have used color-curves to infer host galaxy reddenings and the representative R_V value for each SN

subtype. We have derived BCs for SNe I Ib, Ib, and Ic, with suitable data for this, which we have then used to construct bolometric light curves. Using those light curves, we have calculated ^{56}Ni masses from the radioactive tail, and calibrated the relations between ^{56}Ni mass and peak time/luminosity. Finally, we have used those relations to compute ^{56}Ni masses for the entire sample.

Our main conclusions are the following:

1. For SNe I Ib, Ib, and Ic we find representative R_V values of 2.6 ± 0.4 , 2.7 ± 0.5 , and 3.8 ± 0.4 , respectively. Although SNe Ic may display a larger R_V compared to SNe I Ib and Ib, we cannot rule out that the R_V values of all SE SNe are drawn from a common distribution. We further find that the host-galaxy reddening distributions for SNe II and I Ib are statistically similar, the said distribution for SNe Ib is similar to those of SNe II, I Ib, and Ic, but the distribution for SNe Ic is statistically different from those for SNe II and SNe I Ib.
2. We find that the equation of [Khatami & Kasen \(2019\)](#) for radioactive ^{56}Ni -powered transients with a single β value, which allows to relate peak time and luminosity to the ^{56}Ni mass, is not very useful to estimate individual ^{56}Ni masses for SE SNe. The reason is that β is not constant but decreases with decline rate, varying significantly between SNe. Instead, we have derived an empirically calibrated relation between peak time, peak luminosity, and ^{56}Ni mass. This relation allows estimating ^{56}Ni masses with a precision of 24%. Furthermore, we have shown that the ^{56}Ni mass correlates not only with the peak time and luminosity, but also with the decline rate. The correlation that we infer allows estimating ^{56}Ni masses with an improved precision of 14%.
3. We derive mean ^{56}Ni masses of 0.066 ± 0.006 , 0.082 ± 0.009 , and $0.132 \pm 0.012 M_\odot$ for SNe I Ib, Ib, and Ic, respectively. The ^{56}Ni mass distributions of SNe I Ib and Ib are statistically similar, while SNe Ic synthesize systematically more ^{56}Ni than SNe I Ib and Ib. The mean ^{56}Ni mass of each of these SE SN subtypes is significantly greater than that of SNe II.
4. For SE SNe as a whole, we obtain mean ^{56}Ni and iron yields of 0.090 ± 0.005 and $0.097 \pm 0.007 M_\odot$, respectively. Combined with the recent mean ^{56}Ni mass for SNe II found by [Rodríguez et al. \(2021\)](#), we derive mean ^{56}Ni and iron yields for CC SNe as a whole, of 0.055 ± 0.006 and $0.058 \pm 0.007 M_\odot$,

respectively. Iron production in CC SNe is split about 50-50 among SE SNe and SNe II.

5. Radioactive ^{56}Ni -powered models, like those of Dessart et al. (2016), Woosley et al. (2021), and different hydrodynamical models in the literature, typically underestimate the peak luminosity for SE SNe by 60–70%. A possible explanation is the presence of a power source other than radioactive ^{56}Ni decay that contributes to the luminosity at peak.
6. From analysing the correlation between reddening and EW_{NaID} , we have found that the regions in which SE SNe and SNe II explode have higher dust-to-gas ratios and/or lower neutral sodium to total gas ratios, compared to the diffuse interstellar medium of our Galaxy.

Even though for some SE SNe the radioactive ^{56}Ni -powered models can provide ^{56}Ni masses consistent with $M_{\text{Ni}}^{\text{tail}}$, these models, in general, overestimate M_{Ni} . Therefore, they only provide an upper limit for M_{Ni} . For accurate estimations of ^{56}Ni masses of SE SNe, we recommend using the luminosity in the radioactive tail and equation (7) and/or the peak time, peak luminosity, and decline rate along with equation (60) (or equation 61 if decline rate is not available).

1 We thank A. Aryan, R. Chornock, A. Gangopadhyay,
 2 D. K. Sahu, and M. Stritzinger for sharing spectra with
 3 us. This paper is part of a project that has received
 4 funding from the European Research Council (ERC)
 5 under the European Union’s Seventh Framework Pro-
 6 gramme, Grant agreement No. 833031 (PI: Dan Maoz)
 7 and grant agreement No. 818899 (PI: Ehud Nakar).
 8 Based on observations obtained with the Samuel Oschin
 9 48-inch Telescope at the Palomar Observatory as part
 10 of the Zwicky Transient Facility project. ZTF is sup-
 11 ported by the National Science Foundation under Grant
 12 No. AST-1440341 and a collaboration including Cal-
 13 tech, IPAC, the Weizmann Institute for Science, the Os-
 14 kar Klein Center at Stockholm University, the University
 15 of Maryland, the University of Washington, Deutsches
 16 Elektronen-Synchrotron and Humboldt University, Los
 17 Alamos National Laboratories, the TANGO Consortium
 18 of Taiwan, the University of Wisconsin at Milwaukee,
 19 and Lawrence Berkeley National Laboratories. Oper-
 20 ations are conducted by COO, IPAC, and UW. The
 21 work made use of Swift/UVOT data reduced by P. J.
 22 Brown and released in the Swift Optical/Ultraviolet
 23 Supernova Archive (SOUSA). SOUSA is supported by
 24 NASA’s Astrophysics Data Analysis Program through
 25 grant NNX13AF35G. This research has made use of
 26 the NASA/IPAC Extragalactic Database (NED) which
 27 is operated by the Jet Propulsion Laboratory, Califor-
 28 nia Institute of Technology, under contract with the
 29 National Aeronautics and Space Administration. This
 30 work has made use of the Weizmann Interactive Super-
 31 nova Data Repository (<https://www.wiserep.org>). This
 32 research has made use of the Spanish Virtual Ob-
 33 servatory (<https://svo.cab.inta-csic.es>) project funded
 34 by MCIN/AEI/10.13039/501100011033/ through grant
 35 PID2020-112949GB-I00.

Software: EMCEE (Foreman-Mackey et al. 2013),
 ALR (Rodríguez et al. 2019) LOESS (Cleveland et al.
 1992)

APPENDIX

A. SYNTHETIC MAGNITUDES AND EFFECTIVE WAVELENGTHS

Given a SED f_λ (in $\text{erg s}^{-1} \text{cm}^{-2} \text{\AA}^{-1}$), we can compute the synthetic magnitude in the x -band using

$$m_x = -2.5 \log \int d\lambda S_{x,\lambda} \frac{\lambda f_\lambda}{hc} + \text{ZP}_{\text{mag},x} \quad (\text{A1})$$

(e.g. Hamuy 2001). Here, λ is the observed wavelength (in \AA), $S_{x,\lambda}$ is the peak-normalized x -band transmis-

sion function (considering a photon-counting detector), $hc = 1.986 \times 10^{-8} \text{ erg \AA}$, and $\text{ZP}_{\text{mag},x}$ is the zero-point for the magnitude system.

To convert magnitudes to monochromatic fluxes \bar{f}_x (in $\text{erg s}^{-1} \text{cm}^{-2} \text{\AA}^{-1}$), we use $f_\lambda = \bar{f}_x$ in equation (A1), thus obtaining equation (33), where

$$\text{ZP}_{\text{flux},x} = 2.5 \log \int d\lambda S_{x,\lambda} \frac{\lambda}{hc} + \text{ZP}_{\text{mag},x}. \quad (\text{A2})$$

The $ZP_{\text{mag},x}$ and $ZP_{\text{flux},x}$ values for the Johnson-Kron-Cousins $BVRI$, Sloan gri , ZTF r (r_{ZTF}), and 2MASS JHK bands were reported in Rodríguez et al. (2021). Here we compute the corresponding values for the Johnson U , ZTF g (g_{ZTF}), CSP Y , and Swift UVOT $w2$, $w1$, and u bands.

To compute $ZP_{\text{mag},x}$ for $w2$, $w1$, u , U , and Y bands in the Vega system, we use equation (A1) along with the Vega SED published by Bohlin & Gilliland (2004)¹¹ as f_λ . We adopt the transmission functions given in Stritzinger et al. (2005) for the U -band, in the CSP webpage¹² for the Y -band, and in the SVO Filter Profile Service¹³ (Rodrigo et al. 2012; Rodrigo & Solano 2020) for the UVOT filters. We also adopt $U = 0.02$ (Fukugita et al. 1996), $Y = 0.0$ (Hamuy et al. 2006), and $m_x = 0.0$ for the UVOT filters (Poole et al. 2008). To calculate $ZP_{\text{mag},g_{\text{ZTF}}}$ in the AB system, we use equation (A1), $f_\lambda = 1/\lambda^2$ and $m_x = -2.408$. To construct the g_{ZTF} transmission function, we use equation (1) of Pastorello et al. (2007), adopting the corresponding ZTF filter transmission¹⁴ and CCD quantum efficiency,¹⁵ the atmospheric extinction at Palomar Observatory of Hayes & Latham (1975) (assuming an airmass of 1.2) combined with atmospheric telluric lines, a standard aluminium reflectivity curve, and a constant lens throughput.

Table 14 collects the $ZP_{\text{mag},x}$ and $ZP_{\text{flux},x}$ values for the $w2$, $w1$, u , U , g_{ZTF} , and Y bands, along with the estimates reported in Rodríguez et al. (2021).

The monochromatic fluxes (equation 33) are associated to effective wavelengths $\bar{\lambda}_x$, given by

$$\bar{\lambda}_x = \frac{\int d\lambda S_{x,\lambda} \lambda^2 f_\lambda}{\int d\lambda S_{x,\lambda} f_\lambda} \quad (\text{A3})$$

(e.g. Bessell & Murphy 2012), which depend not only on the transmission function but also on the SED of the observed object. To estimate $\bar{\lambda}_x$ for SE SNe, we employ the spectra of the SNe in our sample as a proxy for f_λ . Since the wavelength range of our spectra do not cover the UV filters, for those bands we adopt a Planck function as f_λ with temperatures between 3400 and 19000 K, which produces intrinsic $B-V$ colors similar to those observed for SE SNe (between 0.0 and 1.5 mag). In addition, we include the effect of reddening using E_{B-V}^{MW}

Table 14. Properties of the filters used in this work

x	System	$ZP_{\text{mag},x}$	$ZP_{\text{flux},x}$	$\bar{\lambda}_x$
		(mag)	(mag)	(Å)
$w2$	Vega	13.837	-20.677	...
$w1$	Vega	14.092	-20.956	...
u^a	Vega	14.126	-21.099	3530 ± 50
U	Vega	14.229	-20.953	3630 ± 40
B	Vega	15.300	-20.462	4430 ± 50
g	AB	15.329	-20.770	4760 ± 50
g_{ZTF}	AB	15.382	-20.802	4850 ± 50
V	Vega	14.865	-21.074	5500 ± 30
r	AB	14.986	-21.361	6190 ± 30
r_{ZTF}	AB	15.212	-21.436	6400 ± 30
R	Vega	15.053	-21.629	6480 ± 50
i	AB	14.710	-21.780	7450 ± 30
I	Vega	14.538	-22.354	8030 ± 70
Y	Vega	13.933	-23.133	10440 ± 60
J	Vega	13.729	-23.787	12260 ± 60
H	Vega	13.412	-24.886	16470 ± 20
K	Vega	12.691	-25.948	21550 ± 80

^aSwift u -band.

and E_{B-V} between 0.0 and 0.4 mag, and host galaxy R_V (R_V^{host}) between 2.1 and 4.1. Column 5 of Table 14 lists the $\bar{\lambda}_x$ values and their 1σ errors for u/U , optical, and IR bands.

In the case of the $w1$ and $w2$ bands, their transmission functions have a red tail (e.g. Figure 3 in Brown et al. 2014), and so their $\bar{\lambda}_x$ values have a strong dependence on the SED shape. Indeed, we find that the dependence of $\bar{\lambda}_x$ on the intrinsic $B-V$ color and reddening can be expressed as

$$\bar{\lambda}_x = l_0 + l_1(B-V)_0 + l_2(B-V)_0^2 + \delta\lambda_{\text{red}}, \quad (\text{A4})$$

where

$$\delta\lambda_{\text{red}} = l_3 E_{B-V}^{\text{MW}} + l_4 (1 - l_5 \ln R_V^{\text{host}}) E_{B-V} \quad (\text{A5})$$

is the shift on $\bar{\lambda}_x$ induced by reddening.

Table 15 lists the l_i parameters for the $w2$ and $w1$ filters, while Figure 39 shows the correlation between $\bar{\lambda}_x - \delta\lambda_{\text{red}}$ and $(B-V)_0$ (left-hand panel), and between $\delta\lambda_{\text{red}}$ for $R_V^{\text{host}} = 3.1$ and the total reddening (right-hand panel). As we can see, $\bar{\lambda}_x$ increases as the SED becomes redder or more reddened by dust.

¹¹ https://ssb.stsci.edu/cdbs/current_calspec/alpha_lyr_stis_010.fits

¹² <https://csp.obs.carnegiescience.edu/data/filters>

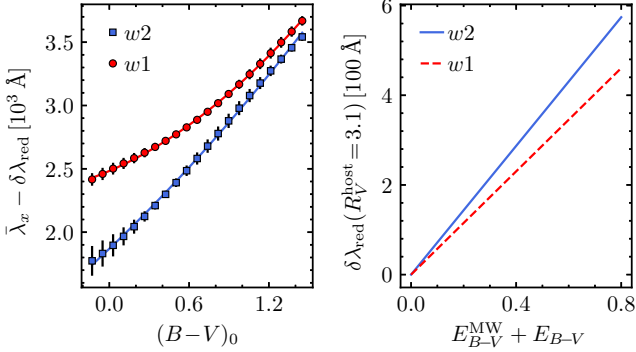
¹³ <http://svo2.cab.inta-csic.es/theory/fps/>

¹⁴ Since they consider an energy-counting detector, we have to divide the transmissions by λ before to use them in equation (A1).

¹⁵ https://github.com/ZwickyTransientFacility/ztf_information

Table 15. $\bar{\lambda}_x$ parameters for the $w2$ and $w1$ filters

x	l_0	l_1	l_2	l_3	l_4	l_5	$\hat{\sigma}$
	(Å)	(Å)	(Å)	(Å)	(Å)		(Å)
$w2$	1869	999	122	718	1337	0.40	50
$w1$	2483	452	255	576	913	0.32	30

**Figure 39.** Left panel: $\bar{\lambda}_x - \delta\lambda_{\text{red}}$ for the $w2$ and $w1$ filters as a function of $(B-V)_0$ for a Planck function. Left panel: shift on $\bar{\lambda}_x$ induced by reddening with $R_V^{\text{host}} = 3.1$ as a function of the total reddening.

B. EXTINCTION AND K -CORRECTIONS

The x -band magnitude corrected for effects of MW reddening E_{B-V}^{MW} , heliocentric redshift z , and host galaxy reddening E_{B-V} , is given by

$$m_{x,0} = m_x - A_x^h - K_x - A_x^{\text{MW}}. \quad (\text{B6})$$

Here, m_x is the apparent magnitude,

$$A_x^h = 2.5 \log \left[\frac{\int d\lambda S_{x,\lambda} \lambda f_\lambda}{\int d\lambda S_{x,\lambda} \lambda f_\lambda 10^{-0.4R_\lambda E_{B-V}}} \right] \quad (\text{B7})$$

is the host galaxy broad-band extinction,

$$K_x = -2.5 \log(1+z) + K_x^s \quad (\text{B8})$$

is the K -correction, with

$$K_x^s = 2.5 \log \left[\frac{\int d\lambda S_{x,\lambda} \lambda f_\lambda 10^{-0.4R_\lambda E_{B-V}}}{\int d\lambda' S_{x,\lambda} \lambda' f_{\lambda'} 10^{-0.4R_{\lambda'} E_{B-V}}} \right], \quad (\text{B9})$$

and

$$A_x^{\text{MW}} = 2.5 \log \left[\frac{\int d\lambda S_{x,\lambda} \lambda' f_{\lambda'} 10^{-0.4R_{\lambda'} E_{B-V}}}{\int d\lambda S_{x,\lambda} \lambda' f_{\lambda'} 10^{-0.4(R_{\lambda'} E_{B-V} + R_\lambda^{\text{MW}} E_{B-V}^{\text{MW}})}} \right] \quad (\text{B10})$$

is the MW broad-band extinction. In the previous expressions, $\lambda' = \lambda/(1+z)$ is the wavelength in the SN rest

frame, while R_λ and R_λ^{MW} are the extinction curve for the host galaxy and the MW, respectively. We adopt the Fitzpatrick (1999) extinction curve with $R_V = 3.1$ for the MW, and with R_V values of 2.6, 2.7, and 3.7 for the host galaxies of SNe IIb, Ib, and Ic, respectively (see Section 3.5).

To compute A_x^h , K_x^s , and A_x^{MW} we use the spectra of the SNe in our sample as f_λ . From those spectra we select those having differences between synthetic and observed colors lower than 0.1 mag, and then we correct them for redshift and reddening. Since A_x^h , K_x^s , and A_x^{MW} have dependencies on E_{B-V} , z , and/or E_{B-V}^{MW} , we compute those corrections using values from uniform distributions. For SNe IIb, Ib, and Ic we use $(E_{B-V}^{\text{MW}}, z, E_{B-V})$ between zero and (0.4, 0.06, 0.4), (0.3, 0.08, 0.6), and (0.3, 0.13, 0.7), respectively.

The top panels of Figure 40 shows the ratios between the A_V^h values and the input E_{B-V} against $(B-V)_0$, where blue (red) symbols correspond to $t - t_V^{\text{peak}}$ epochs before (after) the time of maximum $B-V$ color (t_{B-V}^{max}). We see that A_V^h/E_{B-V} decreases as $(B-V)_0$ increases, which is consistent with the fact that λ_V increases as the SN becomes redder. In general, we find that the quantity A_x^h/E_{B-V} is linearly correlated with the intrinsic color c_0 , i.e.,

$$A_x^h/E_{B-V} = h_{x,c,0} + h_{x,c,1}c_0. \quad (\text{B11})$$

In the case of K_x^s , we find that K_x^s/z correlates with c_0 and E_{B-V} following

$$K_x^s/z = k_{x,c,0} + k_{x,c,1}c_0 + k_{x,c,2}E_{B-V}, \quad (\text{B12})$$

while for $A_x^{\text{MW}}/E_{B-V}^{\text{MW}}$ we find a correlation with c_0 , E_{B-V} , and z , given by

$$A_x^{\text{MW}}/E_{B-V}^{\text{MW}} = g_{x,c,0} + g_{x,c,1}c_0 + g_{x,c,2}E_{B-V} + g_{x,c,3}z. \quad (\text{B13})$$

Tables F13, F14, and F15 collect the parameters of the A_x^h/E_{B-V} , K_x^s/z , and $A_x^{\text{MW}}/E_{B-V}^{\text{MW}}$ terms, respectively, for different optical bands and colors. Solid lines in Figure 40 correspond to the calibrations for $x = V$ and $c = B-V$ for epochs before (blue) and after (red) t_{B-V}^{max} . Since IR spectra are scarce, for each IR band we compute only one set of A_x^h/E_{B-V} , K_x^s/z , and $A_x^{\text{MW}}/E_{B-V}^{\text{MW}}$ calibrations for all phases, whose parameters are listed in Table F16.

Using equation (B11), (B12), and (B13), we can compute A_x^h , K_x^s , and A_x^{MW} through

$$A_x^h = (A_x^h/E_{B-V})E_{B-V}, \quad (\text{B14})$$

$$K_x = -2.5 \log(1+z) + (K_x^s/z)z, \quad (\text{B15})$$

and

$$A_x^{\text{MW}} = (A_x^{\text{MW}}/E_{B-V}^{\text{MW}})E_{B-V}^{\text{MW}}, \quad (\text{B16})$$

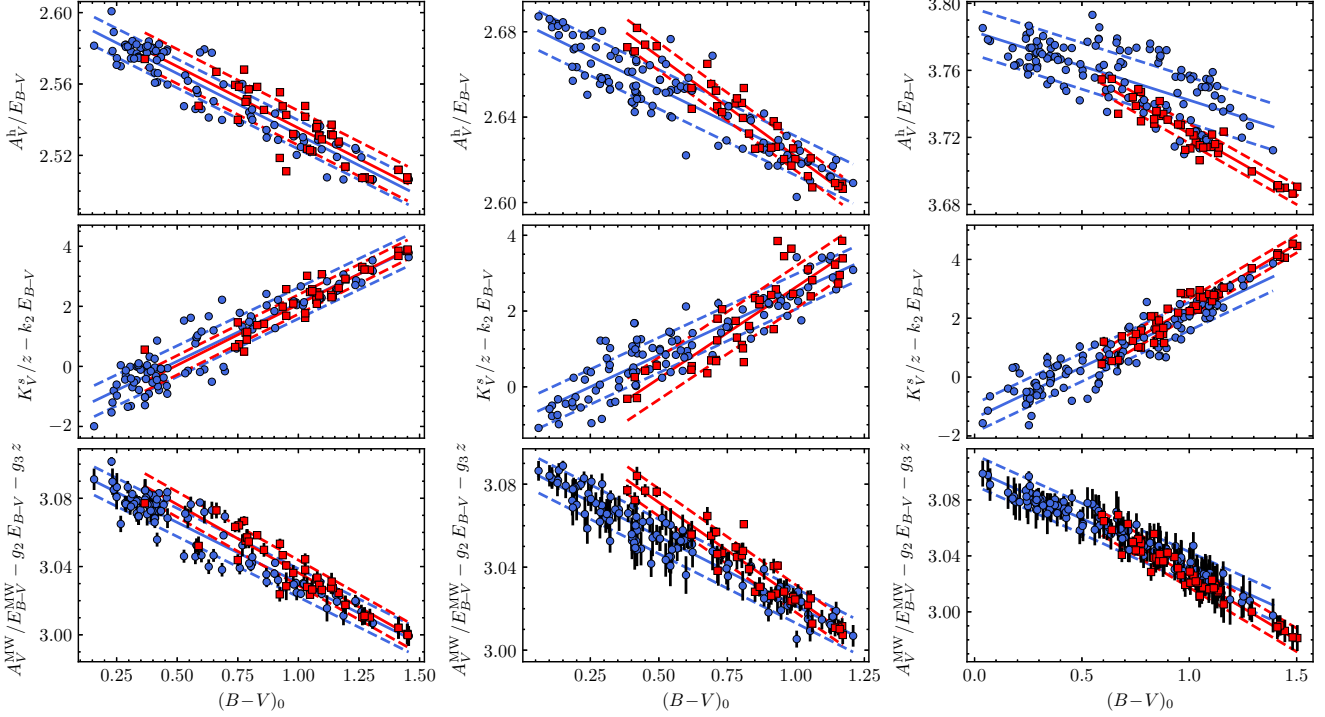


Figure 40. A_V^h/E_{B-V} (top panels), K_V^s/z (middle panels), and A_V^{MW}/E_{B-V}^{MW} (bottom panels) as a function of $(B-V)_0$ for SNe IIb (left-hand panels), Ib (middle-hand panels), and Ic (right-hand panels) at times before (blue circles) and after (red squares) the maximum of the $B-V$ color. Solid lines are straight line fits, while dashed lines are the 1σ limits around the fits.

respectively. The c_0 value, necessary to evaluate A_x^h/E_{B-V} , K_x^s/z , and A_x^{MW}/E_{B-V}^{MW} , is given by

$$c_0 = [c - (g_{c,c,0} + g_{c,c,2}E_{B-V} + g_{c,c,3}z)E_{B-V}^{MW} - (k_{c,c,0} + k_{c,c,2}E_{B-V})z - h_{c,c,0}E_{B-V}] / (1 + h_{c,c,1}E_{B-V} + k_{c,c,1}z + g_{c,c,1}E_{B-V}^{MW}), \quad (\text{B17})$$

where $c = x_1 - x_2$ is the observed color, while $g_{c,c,i} = q_{x_1,c,i} - q_{x_2,c,i}$ for $q = h, k, g$ and $i = 1, 2, 3$.

C. MAGNITUDE TRANSFORMATIONS

To compute conversions between Sloan and natural ZTF gr photometry, we use synthetic magnitudes (equation A1) calculated from the same spectra used in Appendix B. We find that $x - x_{\text{ZTF}}$ (hereafter Δx) for $x = g, r$ can be parametrized as a function of the time since explosion (t) as

$$\Delta x = \begin{cases} \delta_{x,0} + \Psi_{x,a}(t), & t \leq t_x \\ \delta_{x,0} + \Psi_{x,a}(t_x) + \Psi_{x,b}(t - t_x), & t > t_x \end{cases} \quad (\text{C18})$$

Here $\delta_{x,0}$ is the zero-point for the calibration, t_x is a reference time to be determined, while

$$\Psi_{x,a}(t) = a_{x,1} \frac{t}{100 \text{ d}} + a_{x,2} \left(\frac{t}{100 \text{ d}} \right)^2 \quad (\text{C19})$$

and

$$\Psi_{x,b}(t - t_x) = b_{x,1} \frac{t - t_x}{100 \text{ d}} + b_{x,2} \left(\frac{t - t_x}{100 \text{ d}} \right)^2 \quad (\text{C20})$$

describe the dependence of Δx on t before and after t_x , respectively.

From a sample of N SNe, we estimate t_x and the parameters of $\Psi_{x,a}$ and $\Psi_{x,b}$ minimizing

$$s^2 = \sum_{j=1}^N \left[\sum_{k}^{t_{j,k} \leq t_x} [\Delta x_{j,k} - \delta_{x,j} - \Psi_{x,a}(t_{j,k})]^2 + \sum_{k}^{t_{j,k} > t_x} [\Delta x_{j,k} - \delta_{x,j} - \Psi_{x,a}(t_x) - \Psi_{x,b}(t_{j,k} - t_x)]^2 \right]$$

where $\delta_{x,j}$ is the zero-point for the j -th SN. We then adopt the mean and $\hat{\sigma}$ of the $\delta_{x,j}$ estimates as $\delta_{x,0}$ and its error, respectively.

Figure 41 shows the results of the minimization of equation (C21) for $g - g_{\text{ZTF}}$ (top panels) and $r - r_{\text{ZTF}}$ (middle panels), where the $\delta_{x,j}$ values are shown in the bottom panels. Table 16 lists the parameters for the Sloan/ZTF magnitude transformations, along with the time range where they are valid (Column 11). The errors are ≤ 0.025 mag.

Table 16. Parameters for the transformation between Sloan and ZTF gr magnitudes

Δx	Type	$a_{x,1}$	$a_{x,2}$	t_x	$b_{x,1}$	$b_{x,2}$	$\hat{\sigma}$	$\delta_{x,0}$	N	t range
		(mag)	(mag)	(d)	(mag)	(mag)	(mag)	(mag)		(d)
$g - g_{\text{ZTF}}$	IIb	0.226	-0.152	49.9	-0.053	0.0	0.012	0.002 ± 0.017	14	2.0–137.2
	Ib	0.217	-0.153	45.7	-0.079	0.064	0.010	0.001 ± 0.009	18	2.1–134.5
	Ic	0.384	-0.329	30.3	-0.044	0.0	0.009	-0.005 ± 0.019	23	1.3–138.1
$r - r_{\text{ZTF}}$	IIb	0.266	-0.168	48.4	-0.165	0.0	0.014	-0.026 ± 0.014	11	3.1–157.6
	Ib	0.243	-0.185	45.2	-0.199	0.0	0.016	-0.022 ± 0.013	18	2.1–134.5
	Ic	0.304	-0.234	39.0	-0.142	0.0	0.021	-0.060 ± 0.025	24	3.0–144.7

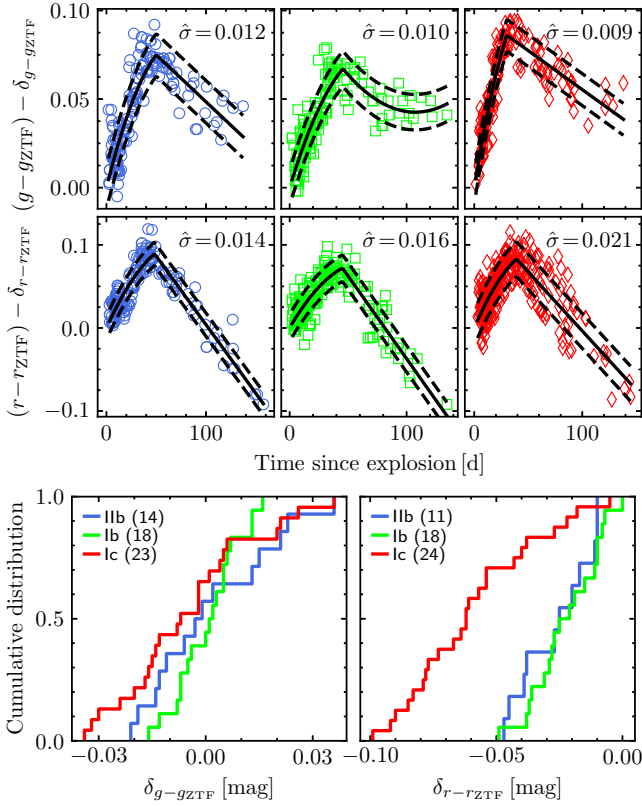


Figure 41. Top and middle rows: shapes of the magnitude transformation between Sloan and ZTF systems for SNe IIb (blue circles), Ib (green squares), and Ic (red diamonds). Solid lines are the best fits to the data, while dashed lines are the $1\hat{\sigma}$ limits around the fits. Bottom panels: Cumulative distributions for the zero-points of the $g - g_{\text{ZTF}}$ (left panel) and $r - r_{\text{ZTF}}$ (right panel) calibrations.

D. EQUIVALENT WIDTH

By definition, the equivalent width (EW) of a spectral line with flux f_λ at wavelength λ is

$$\text{EW} = \int_{\lambda_b}^{\lambda_r} \left(1 - \frac{f_\lambda}{f_{c,\lambda}}\right) d\lambda, \quad (\text{D22})$$

where $f_{c,\lambda}$ is the flux of the continuum at λ , while λ_b and λ_r are the blue and red endpoints of the line profile, respectively. For a spectrum with fluxes f_i at wavelengths λ_i and a spectral dispersion h , we evaluate equation (D22) using the trapezoidal rule, obtaining

$$\text{EW} = h \left[N - 1 - \frac{n_b + n_r}{2} - \sum_{i=b+1}^{r-1} n_i \right]. \quad (\text{D23})$$

Here

$$n_i = f_i / f_{c,\lambda_i} \quad (\text{D24})$$

is the continuum normalized flux, b and r are the indexes of the λ_i elements corresponding to λ_b and λ_r , respectively, and N is the number of pixels in the line region ($\lambda_b \leq \lambda_i \leq \lambda_r$).

To estimate $f_{c,\lambda}$, we first define the continuum region as the N_r pixels at the left of λ_r and the N_b pixels at the right of λ_b . Typically we adopt $N_r = N_b = N$, but we also choose N_r and N_b in order not to include nearby absorption lines and/or bad pixels. Then we fit a low-order polynomial (typically of order two) to the points in the continuum region, which we use as $f_{c,\lambda}$. We also measure the $\hat{\sigma}$ dispersion around the continuum fit ($\hat{\sigma}_{f_c}$), and adopt it as the error in the continuum flux.

The error on EW, computed by error propagation, is

$$\sigma_{\text{EW}} = h \left[\frac{\sigma_{n_b}^2 + \sigma_{n_r}^2}{4} + \sum_{i=b+1}^{r-1} \sigma_{n_i}^2 \right]^{1/2}, \quad (\text{D25})$$

where

$$\sigma_{n_i}^2 = n_i^2 \left[(\sigma_{f_i} / f_i)^2 + (\hat{\sigma}_{f_c}^2 + \delta_{f_c}^2) / f_{c,i}^2 \right]. \quad (\text{D26})$$

Here σ_{f_i} is the error in the line flux, which we assume equal to $\hat{\sigma}_{f_c}$ for weak lines, and δ_{f_c} is the error induced by the uncertainty on the determination of the continuum. To estimate δ_{f_c} we vary the extremes of the continuum region by ± 1 pixel, calculate the EW for each

configuration, and compute the $\hat{\sigma}$ value of the EW estimates ($\hat{\sigma}_{\text{EW}}$). Then, δ_{f_c} is such that equation (D25) is equal to $\hat{\sigma}_{\text{EW}}$ for $\hat{\sigma}_{f_c} = \sigma_{f_i} = 0$, so

$$\delta_{f_c} = \frac{\hat{\sigma}_{\text{EW}}}{h} \left[\frac{1}{4} \left(\frac{n_b^2}{f_{c,b}^2} + \frac{n_r^2}{f_{c,r}^2} \right) + \sum_{i=b+1}^{r-1} \frac{n_i^2}{f_{c,i}^2} \right]^{-1/2}. \quad (\text{D27})$$

In particular, for the case of weak lines, equation (D25) can be written as

$$\sigma_{\text{EW}} = \sqrt{2h(\lambda_r - \lambda_b - \text{EW})/\text{SNR}^2 + \hat{\sigma}_{\text{EW}}^2}, \quad (\text{D28})$$

where we adopt the ratio between the mean of the continuum flux and $\hat{\sigma}_{f_c}$ as the signal to noise ratio (SNR).

To measure EW from a sample of spectra, we combine those obtained with the same instrument configuration (i.e. with the same spectral resolution and dispersion). This improves the SNR, lessens $\hat{\sigma}_{\text{EW}}$, and therefore reduces σ_{EW} . First, for the j -th instrument configuration, we linearly interpolate the spectra in a range between $\lambda_b - hN_b$ and $\lambda_r + hN_r$ with a spectral dispersion h . Next, for each spectrum we determine the continuum and compute n_i and σ_{n_i} using equation (D24) and (D26), respectively. Then, we combine the n_i values for each λ_i using the weighted average along with the Tukey (1977) rule to identify and discard outliers. Figure 42 shows as an example the continuum normalized spectra of SN 2004gq observed with the FAST spectrograph around the host galaxy Na ID line (thin colored lines), along with the combined spectrum (thick line). After that, we compute EW_j and σ_{EW_j} in the combined spectrum using equation (D23) and (D25), respectively, and repeat the whole process for all the available instrument configurations. Finally, using the set of $\text{EW}_j \pm \sigma_{\text{EW}_j}$ values, we compute EW maximizing the log-likelihood of a constant model ($y_j = \text{EW}_j$ and $\bar{y} = \text{EW}$ in equation 9). The error on EW is given by

$$\sigma_{\text{EW}} = \left[\sum_j 1/(\sigma_{\text{EW}_j}^2 + \sigma_0^2) \right]^{-1/2}. \quad (\text{D29})$$

It is worth mentioning that the expression for the EW error given in equation (6) of Vollmann & Eversberg (2006) is incorrect. The problem originates from their equation (4), where they use $\hat{\sigma}_{f_c}$ instead of $\hat{\sigma}_{f_c}/\sqrt{N}$ as the error of the mean continuum flux. The same occurs for the error of the mean line flux (they use $\hat{\sigma}_f$ instead of $\hat{\sigma}_f/\sqrt{N}$). Including the missing $1/\sqrt{N}$ factor and assuming $\hat{\sigma}_f = \hat{\sigma}_{f_c}$, equation (6) of Vollmann & Eversberg (2006) becomes

$$\sigma_{\text{EW}} = \sqrt{2h(\lambda_r - \lambda_b - \text{EW})/\text{SNR}}, \quad (\text{D30})$$

which corresponds to equation (D28) for $\hat{\sigma}_{\text{EW}} = 0$.

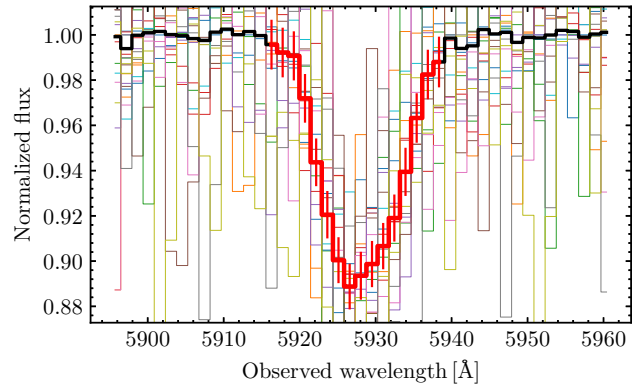


Figure 42. Continuum normalized spectra of SN 2004gq around the host galaxy Na ID line (thin colored lines) and the corresponding weighted-average spectrum (thick line). The thick red line indicates the line region, and vertical error bars are 1σ errors.

E. REFERENCE LIST FOR THE DATA

Here the references for Tables F1, F2, F5, and F7.

- (1) Pooley et al. (1993); (2) Trammell et al. (1993);
- (3) Richmond et al. (1994); (4) Benson et al. (1994);
- (5) Richmond et al. (1996a); (6) Wada & Ueno (1997);
- (7) Matthews et al. (2002); (8) Richmond et al. (1996b);
- (9) Qiu et al. (1999); (10) Galama et al. (1998);
- (11) McKenzie & Schaefer (1999); (12) Patat et al. (2001);
- (13) Sollerman et al. (2002); (14) Clocchiatti et al. (2011);
- (15) Benetti et al. (2011); (16) Stritzinger et al. (2002);
- (17) Yoshii et al. (2003); (18) Pandey et al. (2003);
- (19) Foley et al. (2003); (20) Tomita et al. (2006);
- (21) Valenti et al. (2008a); (22) Bianco et al. (2014);
- (23) Taubenberger et al. (2006); (24) Drout et al. (2011);
- (25) Stritzinger et al. (2018b); (26) Sako et al. (2018);
- (27) Pritchard et al. (2014); (28) Stritzinger et al. (2009);
- (29) Hunter et al. (2009); (30) Chen et al. (2014);
- (31) Sahu et al. (2009); (32) Roy et al. (2013);
- (33) Malesani et al. (2009); (34) Modjaz et al. (2009);
- (35) Pastorello et al. (2008b); (36) Roming et al. (2009);
- (37) Tsvetkov et al. (2009); (38) Taubenberger et al. (2011);
- (39) Pignata et al. (2011); (40) Valenti et al. (2011);
- (41) Folatelli et al. (2014); (42) Valenti et al. (2012);
- (43) Ergon et al. (2014); (44) Brown et al. (2014);
- (45) Ergon et al. (2015); (46) Milisavljevic et al. (2013a);
- (47) Kumar et al. (2013); (48) Morales-Garoffolo et al. (2015);
- (49) Bufano et al. (2014); (50) Barbarino et al. (2021);
- (51) Pian et al. (2020); (52) Fremling et al. (2016);
- (53) Liu et al. (2015); (54) Milisavljevic et al. (2013b);
- (55) Pandey et al. (2021); (56) Ben-Ami et al. (2012);
- (57) Prentice et al. (2019); (58) Van Dyk et al. (2014);
- (59) Morales-Garoffolo et al. (2014); (60) Szalai et al. (2016);
- (61) Drout et al. (2016); (62) Stritzinger et al.

(2020); (63) Srivastav et al. (2014); (64) Folatelli et al. (2016); (65) Zhang et al. (2018); (66) Sahu et al. (2018); (67) De et al. (2018); (68) Barbarino et al. (2017); (69) Gangopadhyay et al. (2020); (70) Gangopadhyay et al. (2018); (71) Singh et al. (2021); (72) Taddia et al. (2016); (73) Aryan et al. (2021); (74) Kumar et al. (2018); (75) Prentice et al. (2018); (76) Terreran et al. (2019); (77) Tsvetkov et al. (2020); (78) Tartaglia et al. (2017); (79) Bersten et al. (2018); (80) Van Dyk et al. (2018); (81) Xiang et al. (2019); (82) Teffs et al. (2021); (83) Balakina et al. (2021); (84) Graham et al. (2019); (85) Bellm et al. (2019); (86) Masci et al. (2019); (87) Kilpatrick et al. (2021);

(88) Rho et al. (2021); (89) Ho et al. (2020); (90) Medler et al. (2021); (91) Gerke et al. (2011); (92) Durrell et al. (2010); (93) McQuinn et al. (2017); (94) Riess et al. (2016); (95) Jang & Lee (2017); (96) Saha et al. (2006); (97) Taddia et al. (2015); (98) Arcavi et al. (2011); (99) Strotjohann et al. (2015); (100) Vladilo et al. (1993); (101) Ho & Filippenko (1995); (102) Takada-Hidai et al. (2002); (103) Valenti et al. (2008b); (104) Ritchey & Wallerstein (2012); (105) Cao et al. (2013); (106) Kilpatrick et al. (2018).

F. TABLES

Table F1. SN sample

SN	Type	Host galaxy	E_{B-V}^{MW} (mag)	cz (km s^{-1})	Filters	References
1993J ^a	I Ib	M81	0.069	−34	<i>UBVRI JHK</i>	1, 2, 3, 4, 5, 6, 7
1994I	Ic	M51a	0.031	463	<i>UBVRI</i>	8
1996cb	I Ib	NGC 3510	0.026	713	<i>BVR</i>	9
1998bw ^a	Ic (BL)	ESO 184-G82	0.049	2599	<i>UBVRI JHK</i>	10, 11, 12, 13, 14
1999dn ^a	Ib	NGC 7714	0.045	2798	<i>UBVRI JHK</i>	15
1999ex	Ib	IC 5179	0.017	3422	<i>UBVRI</i>	16
2002ap ^a	Ic (BL)	M74	0.062	657	<i>UBVRI JHK</i>	17, 18, 19, 20
2003jd	Ic (BL)	MCG -01-59-21	0.038	5654	<i>BVRI</i>	21, 22
2004aw ^a	Ic	NGC 3997	0.018	4771	<i>UBVRI JHK</i>	23
2004dk	Ib	NGC 6118	0.135	1573	<i>VR</i>	24
2004dn	Ic	UGC 2069	0.041	3779	<i>VR</i>	24
2004ex ^a	I Ib	NGC 182	0.018	5261	<i>BV gri YJH</i>	25
2004fe	Ic	NGC 132	0.021	5365	<i>BV gri</i>	22, 25
2004ff ^a	I Ib	ESO 552-G40	0.027	6790	<i>BV gri YJH</i>	25
2004gq ^a	Ib	NGC 1832	0.063	1939	<i>UBV gri YJH</i>	22, 25
2004gt ^a	Ic	NGC 4038	0.040	1642	<i>BV gri YJH</i>	22, 25
2004gv ^a	Ib	NGC 856	0.028	5974	<i>BV gri YJH</i>	22, 25
2005Q	I Ib	ESO 244-G31	0.020	6726	<i>BV gri</i>	25
2005aw ^a	Ic	IC 4837A	0.053	2847	<i>BV gri YJH</i>	25
2005az	Ic	NGC 4961	0.010	2535	<i>V ri</i>	22
2005bj	I Ib	MCG +03-43-05	0.076	6649	<i>BV gri</i>	25
2005em ^a	Ic	IC 307	0.079	7789	<i>BV gri YJH</i>	25
2005hg ^a	Ib	UGC 1394	0.089	6388	<i>UBV ri JHK</i>	22
2005hl	Ib	CGCG 374-027	0.071	6945	<i>gri</i>	26
2005hm	Ib	SDSS J213900.63-010138.6	0.046	10427	<i>gri</i>	26
2005kl	Ic	NGC 4369	0.022	1045	<i>V ri</i>	22

Table F1 continued

Table F1 (continued)

SN	Type	Host galaxy	E_{B-V}^{MW} (mag)	cz (km s^{-1})	Filters	References
2005kr	Ic	SDSS J030829.66+005320.1	0.085	40112	<i>gri</i>	26
2005mf ^a	Ic	UGC 4798	0.015	8023	<i>UBV ri JHK</i>	22
2006F	Ib	NGC 935	0.164	4142	<i>UBV ri</i>	22
2006T ^a	IIb	NGC 3054	0.064	2582	<i>UBV gri YJH</i>	22, 25
2006aj ^a	Ic	WISEA J032139.90+165201.8	0.126	10019	<i>w2, w1, u UBV ri JHK</i>	27, 22
2006ba ^a	IIb	NGC 2980	0.045	5720	<i>BV gri YJH</i>	22, 25
2006el	IIb	UGC 12188	0.098	5150	<i>BVR ri</i>	24, 22
2006ep ^a	Ib	NGC 214	0.031	4537	<i>BV gri YJH</i>	22, 25
2006fe	Ic	WISEA J205209.08-003039.2	0.096	21135	<i>gri</i>	26
2006fo ^a	Ib	UGC 2019	0.023	6205	<i>BV gri JHK</i>	22, 25, 26
2006jo	Ib	SDSS J012314.71-001946.7	0.030	23060	<i>gri</i>	26
2006lc ^a	Ib	NGC 7364	0.056	4865	<i>BV gri YJH</i>	22, 25, 26
2006nx	Ic	WISEA J033330.46-004038.3	0.108	37474	<i>gri</i>	26
2007C ^a	Ib	NGC 4981	0.037	1780	<i>BVR gri YJHK</i>	24, 22, 25
2007Y ^a	Ib	NGC 1187	0.018	1390	<i>w2, w1, u BV gri YJHK</i>	28, 27, 25
2007ag ^a	Ic	UGC 5392	0.025	5961	<i>BV gri YJH</i>	22, 25
2007ce ^a	Ic (BL)	WISEA J121018.10+484334.3	0.020	13890	<i>BV ri JH</i>	22
2007cl	Ic	NGC 6479	0.034	6650	<i>BV ri</i>	22
2007gr ^a	Ic	NGC 1058	0.053	518	<i>UBVRI ri JHK</i>	29, 30, 22
2007hn ^a	Ic	NPM1G -04.0556	0.071	8994	<i>BV gri YJH</i>	25
2007kj ^a	Ib	NGC 7803	0.069	5366	<i>BV gri YJH</i>	22, 25
2007ms	Ic	WISEA J203218.30-010053.2	0.181	11692	<i>gr</i>	26
2007ru	Ic (BL)	UGC 12381	0.222	4636	<i>UBVRI ri</i>	31, 22
2007uy ^a	Ib	NGC 2770	0.019	1947	<i>w2, w1, u UBVRI ri JHK</i>	32, 27, 22
2008D ^a	Ib	NGC 2770	0.019	1947	<i>BVRI ri JHK</i>	33, 34, 27, 22
2008aq ^a	IIb	DDO 151	0.039	2390	<i>w2, w1, u BV gri YJH</i>	27, 25
2008ax ^a	IIb	NGC 4490	0.019	565	<i>w2, w1, u UBVRI gri JHK</i>	35, 36, 37, 38, 22
2008bo	IIb	NGC 6643	0.051	1484	<i>BV ri</i>	22
2008hh ^a	Ic	IC 112	0.043	5819	<i>BV gri JHK</i>	22, 25
2009K ^a	IIb	NGC 1620	0.049	3512	<i>BV gri YJH</i>	22, 25
2009Z ^a	IIb	2dFGRS N271Z016	0.040	7534	<i>BV gri YJH</i>	25
2009bb ^a	Ic (BL)	NGC 3278	0.085	2961	<i>BVRI gri YJH</i>	39, 25
2009dp	Ic	NGC 6912	0.060	6968	<i>BV gri</i>	25
2009dt ^a	Ic	IC 5169	0.014	3110	<i>BV gri YJH</i>	25
2009iz ^a	Ib	UGC 2175	0.073	4256	<i>BV ri JHK</i>	22
2009jf ^a	Ib	NGC 7479	0.097	2381	<i>w2, w1, u UBVRI gri JHK</i>	40, 27, 22
2009mg	IIb	ESO 121-G26	0.039	2135	<i>w2, w1, u BV</i>	27
2010as ^a	IIb	NGC 6000	0.147	2236	<i>BVRI gri JHK</i>	41
2010jr	IIb	ESO 362-G18	0.015	3731	<i>w2, w1, u BV</i>	27
2011am	Ib	NGC 4219	0.114	1989	<i>w2, w1, u BV</i>	27

Table F1 continued

Table F1 (*continued*)

SN	Type	Host galaxy	E_{B-V}^{MW} (mag)	cz (km s^{-1})	Filters	References
2011bm ^a	Ic	IC 3918	0.029	6529	<i>UBVRI gri JHK</i>	42
2011dh ^a	I Ib	M51a	0.031	463	<i>w2, w1, u UBVRI gri JHK</i>	43, 44, 45
2011ei	I Ib	NGC 6925	0.050	2792	<i>BVRI</i>	46, 44
2011fu ^a	I Ib	UGC 1626	0.065	5543	<i>UBVRI JHK</i>	47, 48
2011hs ^a	I Ib	IC 5267	0.010	1712	<i>w2, w1, u UBVRI gri JHK</i>	44, 49
PTF11jgj	Ic	MCG +10-23-80	0.025	12000	<i>gr</i>	50
PTF11klg	Ic	CGCG 403-24	0.075	7983	<i>gr</i>	50
PTF11rka	Ic	SDSS J124044.82+125321.5	0.030	22305	<i>gri</i>	51, 50
2012P	I Ib	NGC 5806	0.044	1400	<i>BV gri</i>	44, 52
2012ap	Ic (BL)	NGC 1729	0.044	3632	<i>BVRI</i>	44, 53
2012au	Ib	NGC 4790	0.041	1344	<i>w2, w1, u UBVRI</i>	54, 55
PTF12gzk ^a	Ic	WISEA J221241.50+003042.9	0.043	4128	<i>BVRI gri YJHK</i>	56, 44, 50
iPTF12hvv	Ic	WISEA J214546.44-000330.6	0.072	8796	<i>gr</i>	50
2013F	Ic	IC 5325	0.018	1503	<i>BVRI</i>	57
2013ak	I Ib	ESO 430-20	0.393	1020	<i>w2, w1, u BV</i>	44
2013bb	I Ib	NGC 5504	0.013	5248	<i>BV gri</i>	57
2013df ^a	I Ib	NGC 4414	0.017	716	<i>UBVRI gri JH</i>	58, 44, 59, 60
2013dk	Ic	NGC 4038	0.040	1642	<i>BV</i>	44
2013ek	Ib	NGC 6984	0.032	4670	<i>BVRI</i>	57
2013ge	Ic	NGC 3287	0.020	1306	<i>BVRI ri</i>	44, 61
LSQ13abf	Ib	LEDA 1582856	0.029	6237	<i>BV ri</i>	62
iPTF13bvn	Ib	NGC 5806	0.044	1359	<i>w2, w1, u UBVRI gri</i>	44, 63, 52, 64
2014L	Ic	M99	0.033	2407	<i>UBVRI</i>	65
2014ad	Ic (BL)	Mrk 1309	0.038	1716	<i>w2, w1, u UBVRI</i>	66
2014ft	Ic	WISEA J233329.82+333848.2	0.079	18900	<i>BV gri</i>	67
LSQ14efd	Ic	WISEA J033537.94-585239.2	0.032	20146	<i>BVRI gri</i>	68
2015ah ^a	Ib	UGC 12295	0.068	4882	<i>BV gri JHK</i>	57
2015ap	Ib	IC 1776	0.036	3410	<i>w2, w1, u UBVRI gri</i>	44, 57, 69
2015as	I Ib	UGC 5460	0.008	1093	<i>w2, w1, u BVI gri</i>	44, 70
2015dj	Ib	NGC 7371	0.050	2683	<i>BV gri</i>	71
iPTF15dtg	Ic	anonymous	0.054	15709	<i>B gri</i>	72
2016P	Ic	NGC 5374	0.023	4382	<i>BVRI gri</i>	57, 69
2016bau	Ib	NGC 3631	0.014	1156	<i>w2, w1, u BVRI</i>	44, 73
2016coi ^a	Ic (BL)	UGC 11868	0.074	1093	<i>w2, w1, u UBVRI gri JHK</i>	44, 74, 75, 76, 77
2016gkg ^a	I Ib	NGC 613	0.017	1481	<i>w2, w1, u UBVRI gri JHK</i>	44, 78, 79, 57
2016iae ^a	Ic	NGC 1532	0.013	1040	<i>BV gri JHK</i>	57
2016jdw	Ib	KUG 1313+309	0.010	5661	<i>gri</i>	57
2017bgu	Ib	2MASX J16555976+4233370	0.018	2549	<i>gri</i>	57
2017dcc	Ic (BL)	LCRS B124628.6-115605	0.039	7495	<i>gri</i>	57
2017ein	Ic	NGC 3938	0.018	809	<i>BVRI gri</i>	44, 80, 81, 82

Table F1 *continued*

Table F1 (continued)

SN	Type	Host galaxy	E_{B-V}^{MW} (mag)	cz (km s^{-1})	Filters	References
2017gpn	I Ib	NGC 1343	0.293	2215	<i>BVR gri</i>	57, 83
2017hyh	I Ib	MCG +01-19-01	0.114	3609	<i>BV gri</i>	57
2017ifh	Ic (BL)	LEDA 2373101	0.112	11700	<i>BV gri</i>	57
2018ie	Ic (BL)	NGC 3456	0.058	4267	<i>BV gri</i>	57
2018cbz	Ic (BL)	IC 908	0.029	6702	<i>gri</i>	57
2018cem	Ic	CGCG 195-13	0.029	8881	<i>gzTF, rZTF</i>	84, 85, 86
2018ddu	Ic	CGCG 339-11	0.038	8889	<i>gzTF, rZTF</i>	84, 85, 86
2018dgx	Ic	CGCG 278-31	0.034	7590	<i>gzTF, rZTF</i>	84, 85, 86
2018dzw	I Ib	WISEA J155626.06+465406.0	0.011	11079	<i>gzTF, rZTF</i>	84, 85, 86
2018iby	I Ib	UGC 6338	0.018	7557	<i>gzTF, rZTF</i>	84, 85, 86
2018kva	Ic	WISEA J083516.34+481901.2	0.026	12868	<i>gzTF, rZTF</i>	84, 85, 86
2019bjv	Ic	WISEA J162538.62+472614.6	0.007	7590	<i>gzTF, rZTF</i>	84, 85, 86
2019bwi	Ib	WISEA J092524.57+652805.5	0.089	8896	<i>gzTF, rZTF</i>	84, 85, 86
2019cda	Ic	NGC 3362	0.027	8318	<i>gzTF, rZTF</i>	84, 85, 86
2019dgz	Ib	WISEA J121604.98+295106.6	0.018	10905	<i>gzTF, rZTF</i>	84, 85, 86
2019gqd	Ic	KUG 1627+399	0.010	10748	<i>gzTF, rZTF</i>	84, 85, 86
2019gwc	Ic (BL)	WISEA J160326.65+381057.0	0.011	11372	<i>gzTF, rZTF</i>	84, 85, 86
2019hjg	Ic	WISEA J154412.47+410656.8	0.018	9702	<i>gzTF, rZTF</i>	84, 85, 86
2019hsx	Ic (BL)	NGC 6621	0.040	6191	<i>gzTF, rZTF</i>	84, 85, 86
2019ieh	Ic	anonymous	0.086	9575	<i>gzTF, rZTF</i>	84, 85, 86
2019krw	Ic	WISEA J175010.53+401337.2	0.038	14090	<i>gzTF, rZTF</i>	84, 85, 86
2019lci	Ic (BL)	AGC 268171	0.064	8766	<i>gzTF, rZTF</i>	84, 85, 86
2019lfj	Ic	WISEA J015748.77+131034.4	0.047	26613	<i>gzTF, rZTF</i>	84, 85, 86
2019moc	Ic (BL)	SDSS J235545.94+215719.7	0.055	16740	<i>gzTF, rZTF</i>	84, 85, 86
2019nxu	Ib	2MASS J00031229-1050052	0.034	8860	<i>gzTF, rZTF</i>	84, 85, 86
2019odp	Ic (BL)	UGC 12373	0.165	4303	<i>gzTF, rZTF</i>	84, 85, 86
2019ofk	I Ib	WISEA J161830.46+182826.0	0.040	10679	<i>gzTF, rZTF</i>	84, 85, 86
2019pfb	Ib	CGCG 303-6	0.069	10967	<i>gzTF, rZTF</i>	84, 85, 86
2019ply	I Ib	CGCG 440-40	0.125	6499	<i>gzTF, rZTF</i>	84, 85, 86
2019qfi	Ic (BL)	WISEA J215107.56+122536.3	0.061	8543	<i>gzTF, rZTF</i>	84, 85, 86
2019qvt	Ib	anonymous	0.149	16039	<i>gzTF, rZTF</i>	84, 85, 86
2019yvr	Ib	NGC 4666	0.021	1529	<i>gri</i>	87
2020oc	Ic	anonymous	0.034	6296	<i>gzTF, rZTF</i>	84, 85, 86
2020oi	Ic	M100	0.023	1571	<i>UBV gri gzTF, rZTF</i>	84, 85, 86, 88
2020pv	Ib	2MASX J14275233+3334090	0.008	8619	<i>gzTF, rZTF</i>	84, 85, 86
2020aok	I Ib	WISEA J111501.59+523019.9	0.014	13889	<i>gzTF, rZTF</i>	84, 85, 86
2020ayz	Ic (BL)	KUG 1209+330	0.011	7527	<i>gzTF, rZTF</i>	84, 85, 86
2020bcq	Ib	NGC 5154	0.012	5545	<i>gzTF, rZTF</i>	84, 85, 86
2020bmj	Ib	WISEA J131231.72+045154.3	0.028	14321	<i>gzTF, rZTF</i>	84, 85, 86
2020bpf	Ib	anonymous	0.065	8163	<i>gzTF, rZTF</i>	84, 85, 86

Table F1 continued

Table F1 (*continued*)

SN	Type	Host galaxy	E_{B-V}^{MW} (mag)	cz (km s^{-1})	Filters	References
2020bvc	Ic (BL)	UGC 9379	0.011	7565	$w2, w1, u$ <i>UBV gri gZTF, rZTF</i>	84, 85, 86, 89, 88
2020cgu	Ic	UGC 3862	0.050	8151	<i>gZTF, rZTF</i>	84, 85, 86
2020cpg	I Ib	CGCG 73-91	0.025	11034	<i>BV gri</i>	90
2020hoi	Ib	WISEA J121345.77+242121.3	0.025	6253	<i>gZTF, rZTF</i>	84, 85, 86
2020hqn	Ic	WISEA J141809.63+052532.1	0.024	7566	<i>gZTF, rZTF</i>	84, 85, 86
2020hvp	Ib	NGC 6118	0.136	1573	<i>gZTF, rZTF</i>	84, 85, 86
2020jqm	Ic (BL)	LCRS B134642.6-033118	0.030	11081	<i>gZTF, rZTF</i>	84, 85, 86
2020kba	Ic (BL)	SDSS J155842.56+085944.7	0.041	19675	<i>gZTF, rZTF</i>	84, 85, 86
2020kzs	Ib	WISEA J171455.01+353113.6	0.026	11200	<i>gZTF, rZTF</i>	84, 85, 86
2020lao	Ic (BL)	CGCG 169-41	0.043	9238	<i>gZTF, rZTF</i>	84, 85, 86
2020mob	I Ib	NGC 6912	0.060	6968	<i>gZTF, rZTF</i>	84, 85, 86
2020nke	Ib	CGCG 139-33	0.053	9230	<i>gZTF, rZTF</i>	84, 85, 86
2020qrx	Ic	2MASX J01235845+1722074	0.138	8522	<i>gZTF, rZTF</i>	84, 85, 86
2020rlg	Ic	UGC 2945	0.186	5233	<i>gZTF, rZTF</i>	84, 85, 86
2020rwz	Ic	anonymous	0.079	11155	<i>gZTF, rZTF</i>	84, 85, 86
2020sai	Ib	anonymous	0.208	8596	<i>gZTF, rZTF</i>	84, 85, 86
2020sbw	I Ib	CGCG 389-7	0.033	6826	<i>gZTF, rZTF</i>	84, 85, 86
2020scb	Ic	CGCG 456-55	0.049	5225	<i>gZTF, rZTF</i>	84, 85, 86
2020sya	Ic	UGC 845	0.049	9423	<i>gZTF, rZTF</i>	84, 85, 86
2020urc	I Ib	UGC 1769	0.039	8013	<i>gZTF, rZTF</i>	84, 85, 86
2020uvh	Ic	PGC 15803	0.261	5156	<i>gZTF, rZTF</i>	84, 85, 86
2020xpn	Ic	WISEA J102538.99+164714.2	0.029	10396	<i>gZTF, rZTF</i>	84, 85, 86
2020yvt	I Ib	UGC 5408	0.011	2997	<i>gZTF, rZTF</i>	84, 85, 86
2020aaxf	I Ib	UGC 4352	0.067	4389	<i>gZTF, rZTF</i>	84, 85, 86
2020abdw	Ic	WISEA J020116.16+240411.8	0.082	9827	<i>gZTF, rZTF</i>	84, 85, 86
2020abpa	Ic	KUG 2329+232	0.052	6987	<i>gZTF, rZTF</i>	84, 85, 86
2020abqx	Ib	SDSS J115224.83+673251.6	0.011	18901	<i>gZTF, rZTF</i>	84, 85, 86
2020acat	I Ib	WISEA J115042.57-101312.2	0.021	2378	<i>gZTF, rZTF</i>	84, 85, 86
2020acfp	Ic	WISEA J112735.48+472246.3	0.017	9812	<i>gZTF, rZTF</i>	84, 85, 86
2020adow	Ic	KUG 0830+278	0.031	2226	<i>gZTF, rZTF</i>	84, 85, 86
2021bm	Ic	WISEA J143747.36+595423.2	0.007	9437	<i>gZTF, rZTF</i>	84, 85, 86
2021do	Ic	NGC 3147	0.022	2802	<i>gZTF, rZTF</i>	84, 85, 86
2021bwq	Ic	IC 2856	0.030	6600	<i>gZTF, rZTF</i>	84, 85, 86
2021dwg	Ic	IC 992	0.033	7793	<i>gZTF, rZTF</i>	84, 85, 86
2021gno	Ib	NGC 4165	0.029	1868	<i>gZTF, rZTF</i>	84, 85, 86
2021gvl	Ic	WISEA J142138.09+353901.8	0.012	10890	<i>gZTF, rZTF</i>	84, 85, 86
2021heh	I Ib	IC 482	0.031	8002	<i>gZTF, rZTF</i>	84, 85, 86
2021hyz	Ic (BL)	WISEA J092736.91+042710.3	0.039	13821	<i>gZTF, rZTF</i>	84, 85, 86
2021jao	Ib	CGCG 37-7	0.019	8530	<i>gZTF, rZTF</i>	84, 85, 86
2021kev	Ib	CGCG 75-118	0.024	9290	<i>gZTF, rZTF</i>	84, 85, 86

Table F1 *continued*

Table F1 (*continued*)

SN	Type	Host galaxy	E_{B-V}^{MW} (mag)	cz (km s^{-1})	Filters	References
2021kum	I Ib	WISEA J112629.27+470741.7	0.018	15889	$g_{\text{ZTF}}, r_{\text{ZTF}}$	84, 85, 86
2021kww	I Ib	WISEA J132759.23+242254.5	0.009	6900	$g_{\text{ZTF}}, r_{\text{ZTF}}$	84, 85, 86
2021mxx	Ic	UGC 11380	0.082	2893	$g_{\text{ZTF}}, r_{\text{ZTF}}$	84, 85, 86
2021pnp	I Ib	WISEA J161626.48+364424.4	0.010	9000	$g_{\text{ZTF}}, r_{\text{ZTF}}$	84, 85, 86
2021qjv	Ic (BL)	WISEA J151047.04+491218.1	0.013	11466	$g_{\text{ZTF}}, r_{\text{ZTF}}$	84, 85, 86

NOTE—References for the data are in Appendix E.

^aSNe used to compute BCs.

REFERENCES

- Afsariardchi, N., Drout, M. R., Khatami, D. K., et al. 2021, *ApJ*, 918, 89, doi: [10.3847/1538-4357/ac0aeb](https://doi.org/10.3847/1538-4357/ac0aeb)
- Anderson, J. P. 2019, *A&A*, 628, A7, doi: [10.1051/0004-6361/201935027](https://doi.org/10.1051/0004-6361/201935027)
- Anupama, G. C., Sahu, D. K., Deng, J., et al. 2005, *ApJL*, 631, L125, doi: [10.1086/497336](https://doi.org/10.1086/497336)
- Arcavi, I., Gal-Yam, A., Yaron, O., et al. 2011, *ApJL*, 742, L18, doi: [10.1088/2041-8205/742/2/L18](https://doi.org/10.1088/2041-8205/742/2/L18)
- Arnett, W. D. 1982, *ApJ*, 253, 785, doi: [10.1086/159681](https://doi.org/10.1086/159681)
- Aryan, A., Pandey, S. B., Zheng, W., et al. 2021, *MNRAS*, 505, 2530, doi: [10.1093/mnras/stab1379](https://doi.org/10.1093/mnras/stab1379)
- Balakina, E. A., Pruzhinskaya, M. V., Moskvitin, A. S., et al. 2021, *MNRAS*, 501, 5797, doi: [10.1093/mnras/staa3383](https://doi.org/10.1093/mnras/staa3383)
- Barbarino, C., Botticella, M. T., Dall’Ora, M., et al. 2017, *MNRAS*, 471, 2463, doi: [10.1093/mnras/stx1709](https://doi.org/10.1093/mnras/stx1709)
- Barbarino, C., Sollerman, J., Taddia, F., et al. 2021, *A&A*, 651, A81, doi: [10.1051/0004-6361/202038890](https://doi.org/10.1051/0004-6361/202038890)
- Bellm, E. C., Kulkarni, S. R., Graham, M. J., et al. 2019, *PASP*, 131, 018002, doi: [10.1088/1538-3873/aaecbe](https://doi.org/10.1088/1538-3873/aaecbe)
- Ben-Ami, S., Gal-Yam, A., Filippenko, A. V., et al. 2012, *ApJL*, 760, L33, doi: [10.1088/2041-8205/760/2/L33](https://doi.org/10.1088/2041-8205/760/2/L33)
- Ben-Ami, S., Hachinger, S., Gal-Yam, A., et al. 2015, *ApJ*, 803, 40, doi: [10.1088/0004-637X/803/1/40](https://doi.org/10.1088/0004-637X/803/1/40)
- Benetti, S., Turatto, M., Valenti, S., et al. 2011, *MNRAS*, 411, 2726, doi: [10.1111/j.1365-2966.2010.17873.x](https://doi.org/10.1111/j.1365-2966.2010.17873.x)
- Benson, P. J., Herbst, W., Salzer, J. J., et al. 1994, *AJ*, 107, 1453, doi: [10.1086/116958](https://doi.org/10.1086/116958)
- Bersten, M. C., Benvenuto, O., & Hamuy, M. 2011, *ApJ*, 729, 61, doi: [10.1088/0004-637X/729/1/61](https://doi.org/10.1088/0004-637X/729/1/61)
- Bersten, M. C., Benvenuto, O. G., Nomoto, K., et al. 2012, *ApJ*, 757, 31, doi: [10.1088/0004-637X/757/1/31](https://doi.org/10.1088/0004-637X/757/1/31)
- Bersten, M. C., Benvenuto, O. G., Folatelli, G., et al. 2014, *AJ*, 148, 68, doi: [10.1088/0004-6256/148/4/68](https://doi.org/10.1088/0004-6256/148/4/68)
- Bersten, M. C., Folatelli, G., García, F., et al. 2018, *Nature*, 554, 497, doi: [10.1038/nature25151](https://doi.org/10.1038/nature25151)

Table F2. Host galaxy distance moduli *

Host galaxy	SN	μ_{CPL}	μ_{TRGB}	μ_{TF}	μ_z	μ_{SVF}	μ
M81	1993J	27.87 ± 0.14^{91}	27.86 ± 0.06^{92}	27.61 ± 0.35	27.86 ± 0.05
M51a	1994I	...	29.67 ± 0.07^{93}	29.67 ± 0.07
	2011dh	29.67 ± 0.07
M74	2002ap	...	29.95 ± 0.08^{93}	29.95 ± 0.08
NGC 4038	2004gt	31.29 ± 0.11^{94}	31.68 ± 0.04^{95}	31.63 ± 0.04
	2013dk	31.63 ± 0.04
NGC 4414	2013df	31.65 ± 0.17^{96}	...	30.95 ± 0.35	31.52 ± 0.15
M100	2020oi	31.18 ± 0.05^{96}	31.18 ± 0.05

NOTE—Column 1: SN host galaxy names. Column 2: SN names, Columns 3 and 4: Cepheids and TRGB distances from the literature, respectively. Column 5: Tully-Fisher distances from EDD. Column 6: distances compute from recessional redshifts. Column 6: distances inferred from smoothed velocity fields (Kourkchi et al. 2020). Column 8: adopted distance moduli. References for the data (superscript numbers) are in Appendix E.

*This table is available in its entirety in machine-readable form.

Table F3. Maximum-light epochs *

SN	t_B^{peak}	t_g^{peak}	$t_{g\text{ZTF}}^{\text{peak}}$	t_V^{peak}	t_r^{peak}	$t_{r\text{ZTF}}^{\text{peak}}$	t_R^{peak}	t_i^{peak}	t_I^{peak}	$\langle t_V^{\text{peak}} \rangle$
1993J	49093.5(3)	49095.1(2)	49095.4(2)	...	49096.1(3)	49095.0(2)
1994I	49450.0(2)	49450.8(1)	49451.1(1)	...	49451.7(1)	49450.7(1)
1996cb	50449.9(1)	50451.7(1)	50453.4(2)	50451.7(1)

NOTE—Epochs are in MJD. Numbers in parentheses are 1σ errors in units of the last significant digits.

*This table is available in its entirety in machine-readable form.

Table F4. Decline rate parameters *

SN	$\Delta m_{15}(B)$	$\Delta m_{15}(g)$	$\Delta m_{15}(g\text{ZTF})$	$\Delta m_{15}(V)$	$\Delta m_{15}(r)$	$\Delta m_{15}(r\text{ZTF})$	$\Delta m_{15}(R)$	$\Delta m_{15}(i)$	$\Delta m_{15}(I)$	$\langle \Delta m_{15}(V) \rangle$
1993J	1.631(19)	1.015(17)	0.725(19)	...	0.571(17)	1.017(14)
1994I	2.033(52)	1.710(15)	1.417(17)	...	1.095(18)	1.703(14)
1996cb	1.365(13)	0.825(12)	0.555(13)	0.829(12)

NOTE—Values are in magnitude units. Numbers in parentheses are 1σ errors in units of the last significant digits.

*This table is available in its entirety in machine-readable form.

Table F5. SN explosion epochs^{*}

SN	$t_{\text{non-det}}$ (MJD)	t_{detect} (MJD)	Phase source	$t_{\text{expl}}^{\text{peak}}$ (MJD)	t_{expl} (MJD)
2006fo	53975.410	53994.430	97	53988.0 ± 3.2	53987.8 ± 3.0
2011dh	55712.275	55712.893	98	55713.6 ± 3.5	55712.6 ± 0.2
2013bb	56368.373	56369.320	99	56375.0 ± 3.6	56368.9 ± 0.3

NOTE—Column 1: SN names. Column 2, 3, and 4: SN last non-detection epochs, first detection epochs, and their references (codes are in Appendix E.), respectively. Column 5: explosion epochs estimated with maximum-light epochs. Column 6: explosions epochs.

^{*}This table is available in its entirety in machine-readable form.

Table F6. Vertical intercepts of the color curves^{*}

SN	δ_{B-V}	δ_{g-i}	δ_{V-r}	δ_{V-R}	δ_{V-i}	δ_{V-I}	$\delta_{(g-r)_{\text{ZTF}}}$
1993J	0.500(44)	0.240(45)	...	0.338(28)	...
1994I	0.857(53)	0.230(36)	...	0.446(72)	...
1996cb	0.295(30)	0.130(33)

NOTE—Values are in magnitude units. Numbers in parentheses are 1σ errors in units of the last significant digits.

^{*}This table is available in its entirety in machine-readable form.

Table F7. Na I D equivalent widths and host galaxy reddenings^{*}

SN	$\text{EW}_{\text{NaID}}^{\text{MW}}$ (Å)	EW_{NaID} (Å)	\tilde{E}_{B-V} (mag)	E_{B-V}^{CC} (mag)	E_{B-V}^{NaID} (mag)	E_{B-V} (mag)
1993J	0.447 ± 0.007^{100}	0.251 ± 0.010^{100}	0.487 ± 0.034	0.070 ± 0.119	0.062 ± 0.094	0.065 ± 0.074
1994I	0.180 ± 0.005^{101}	4.100 ± 0.010^{101}	0.788 ± 0.039	0.233 ± 0.092	...	0.233 ± 0.092
2002ap	0.494 ± 0.004^{102}	0.106 ± 0.002^{102}	0.614 ± 0.040	0.059 ± 0.092	0.026 ± 0.094	0.043 ± 0.066
2007gr	0.310 ± 0.000^{103}	0.130 ± 0.000^{103}	0.648 ± 0.014	0.093 ± 0.084	0.032 ± 0.094	0.066 ± 0.063
2011dh	0.250 ± 0.003^{104}	0.286 ± 0.007^{104}	0.674 ± 0.018	0.257 ± 0.115	0.070 ± 0.094	0.145 ± 0.073
iPTF13bvn	0.250 ± 0.000^{105}	0.420 ± 0.000^{105}	0.512 ± 0.011	0.148 ± 0.084	0.103 ± 0.094	0.128 ± 0.063
2016gkg	0.290 ± 0.000^{79}	0.680 ± 0.030^{78}	0.440 ± 0.021	0.023 ± 0.116	0.167 ± 0.095	0.109 ± 0.073
2017ein	0.150 ± 0.040^{106}	1.441 ± 0.067	0.942 ± 0.010	0.387 ± 0.083	...	0.387 ± 0.083

NOTE—References for the EW_{NaID} values from the literature (superscript numbers) are in Appendix E.

^{*}This table is available in its entirety in machine-readable form.

Table F8. Absolute r -band magnitudes at peak

SN	M_r^{peak}	SN	M_r^{peak}	SN	M_r^{peak}	SN	M_r^{peak}	SN	M_r^{peak}
1993J	-17.482	2007C	-17.592	iPTF12hvv	-18.729	2019bjv	-17.744	2020mob	-17.021
1994I	-17.711	2007Y	-16.131	2013F	-18.701	2019bwi	-18.370	2020nke	-17.083
1996cb	-16.593	2007ag	-18.085	2013ak	-17.537	2019cda	-17.775	2020qrx	-18.925
1998bw	-18.569	2007ce	-19.011	2013bb	-16.650	2019dgz	-17.849	2020rlg	-18.449
1999dn	-16.916	2007cl	-17.892	2013df	-17.464	2019gqd	-19.056	2020rwz	-17.307
1999ex	-17.345	2007gr	-17.534	2013dk	-19.189	2019gwc	-18.225	2020sai	-17.629
2002ap	-17.870	2007hn	-18.226	2013ek	-18.119	2019hjh	-17.494	2020sbw	-17.665
2003jd	-18.614	2007kj	-16.889	2013ge	-17.721	2019hsx	-18.826	2020scb	-18.371
2004aw	-18.366	2007ms	-17.932	LSQ13abf	-17.461	2019ieh	-18.623	2020sya	-18.130
2004dk	-17.457	2007ru	-18.848	iPTF13bvn	-16.711	2019krw	-18.491	2020urc	-17.767
2004dn	-17.699	2007uy	-17.314	2014L	-17.999	2019lci	-18.715	2020uvh	-17.776
2004ex	-17.287	2008D	-16.830	2014ad	-18.276	2019lfj	-18.649	2020xpn	-18.480
2004fe	-17.910	2008aq	-17.355	2014ft	-17.223	2019moc	-19.177	2020yvt	-17.204
2004ff	-17.696	2008ax	-16.770	LSQ14efd	-18.268	2019nxu	-17.806	2020aaxf	-16.987
2004gq	-17.541	2008bo	-15.974	2015ah	-17.576	2019odp	-17.739	2020abdw	-18.881
2004gt	-18.242	2008hh	-18.077	2015ap	-18.102	2019ofk	-17.204	2020abpa	-18.507
2004gv	-17.840	2009K	-17.807	2015as	-16.805	2019pfb	-18.187	2020abqx	-18.835
2005Q	-17.821	2009Z	-18.068	2015dj	-17.369	2019ply	-17.211	2020acat	-17.786
2005aw	-18.352	2009bb	-18.667	iPTF15dtg	-18.259	2019qfi	-18.232	2020acfp	-18.249
2005az	-18.184	2009dp	-18.323	2016P	-18.632	2019qvt	-18.845	2020adow	-18.027
2005bj	-17.853	2009dt	-17.939	2016bau	-17.079	2019yvr	-17.481	2021bm	-17.691
2005em	-18.081	2009iz	-17.016	2016coi	-17.812	2020oc	-17.053	2021do	-18.756
2005hg	-17.796	2009jf	-17.590	2016gkg	-16.607	2020oi	-18.019	2021bwq	-18.549
2005hl	-17.891	2009mg	-17.473	2016iae	-17.752	2020pv	-17.353	2021dwg	-17.655
2005hm	-16.753	2010as	-17.696	2016jdw	-17.543	2020aok	-17.966	2021gno	-16.532
2005kl	-19.667	2010jr	-16.649	2017bgu	-17.336	2020ayz	-18.772	2021gvl	-17.975
2005kr	-18.840	2011am	-17.320	2017dcc	-18.962	2020bcq	-17.505	2021heh	-18.273
2005mf	-17.747	2011bm	-18.952	2017ein	-17.866	2020bmj	-18.136	2021hyz	-18.670
2006F	-16.975	2011dh	-17.616	2017gpn	-17.059	2020bpf	-17.598	2021jao	-17.687
2006T	-17.921	2011ei	-16.016	2017hyh	-17.404	2020bvc	-18.845	2021kev	-18.075
2006aj	-19.091	2011fu	-17.853	2017ifh	-19.117	2020cgu	-18.205	2021kum	-18.045
2006ba	-17.357	2011hs	-16.582	2018ie	-17.676	2020cpg	-17.696	2021kww	-18.037
2006el	-16.927	PTF11jgj	-17.467	2018cbz	-18.674	2020hoi	-17.432	2021mxx	-17.517
2006ep	-17.131	PTF11klg	-17.791	2018cem	-18.056	2020hqn	-17.704	2021pnp	-17.270
2006fe	-18.210	PTF11rka	-19.118	2018ddu	-18.107	2020hvp	-17.070	2021qjv	-18.503
2006fo	-17.904	2012P	-16.321	2018dgx	-17.978	2020jqm	-19.443
2006jo	-18.390	2012ap	-19.120	2018dzw	-17.058	2020kba	-19.981
2006lc	-17.728	2012au	-18.104	2018iby	-16.753	2020kzs	-17.629
2006nx	-19.139	PTF12gzk	-18.463	2018kva	-19.050	2020lao	-18.729

Table F9. Parameters of the BC calibrations

x	$x - y$	a_1	a_2	a_3	a_4	$\hat{\sigma}$	ZP	N	t_{x-y}^{\max} (d)	$t - t_{\text{expl}}$ range (d)
SNe IIb										
B	$B - V$	0.206	-0.878	0.546	-1.348	0.047	11.274 ± 0.053	15	18.8	3.4, 119.6
B	$B - r$	-0.182	-0.362	0.278	-0.961	0.042	11.391 ± 0.052	13	18.2	3.4, 105.3
B	$B - R$	-0.203	-0.255	0.433	-0.939	0.051	11.410 ± 0.036	8	16.6	3.4, 119.6
B	$B - i$	-0.338	-0.177	0.396	-0.872	0.029	11.322 ± 0.027	13	18.0	3.4, 105.3
B	$B - I$	-0.328	-0.131	1.087	-1.089	0.056	11.442 ± 0.056	8	17.2	3.4, 119.6
g	$g - r$	-0.093	-0.681	0.128	-0.934	0.053	11.531 ± 0.061	13	21.7	3.4, 105.3
g	$g - R$	0.159	-0.604	0.234	-0.791	0.057	11.467 ± 0.059	6	21.8	3.4, 105.1
g	$g - i$	-0.291	-0.259	0.230	-0.797	0.045	11.490 ± 0.036	13	18.9	3.4, 105.3
g_{ZTF}	$g_{\text{ZTF}} - r_{\text{ZTF}}$	-0.072	-0.671	0.073	-0.820	0.052	11.554 ± 0.060	13	21.7	3.4, 105.3
V	$V - r$	0.190	-2.152	-0.029	-0.714	0.051	11.660 ± 0.054	13	19.1	3.4, 105.3
V	$V - R$	0.705	-1.463	0.158	-0.499	0.061	11.532 ± 0.044	8	18.5	3.4, 119.6
V	$V - i$	-0.084	-0.762	0.035	-0.559	0.049	11.665 ± 0.040	13	23.5	3.4, 105.3
V	$V - I$	0.193	-0.433	0.029	-0.165	0.063	11.591 ± 0.039	8	22.7	3.4, 119.6
r	$r - i$	0.087	-0.849	-0.082	-0.026	0.070	11.786 ± 0.068	13	24.0	3.4, 105.3
SNe Ib										
B	$B - V$	-0.545	-0.384	0.175	-1.247	0.065	11.481 ± 0.093	15	21.3	5.0, 136.1
B	$B - r$	-0.437	-0.210	0.275	-1.021	0.044	11.423 ± 0.081	14	18.5	5.0, 115.4
B	$B - R$	-0.591	-0.106	0.202	-0.946	0.054	11.609 ± 0.125	5	18.5	7.7, 136.1
B	$B - i$	-0.293	-0.228	0.242	-0.836	0.033	11.316 ± 0.055	14	17.7	5.0, 115.4
g	$g - r$	-0.076	-0.772	0.074	-0.862	0.034	11.526 ± 0.067	10	20.2	5.0, 94.8
g	$g - i$	-0.189	-0.429	0.056	-0.691	0.031	11.501 ± 0.042	10	18.6	5.0, 94.8
g_{ZTF}	$g_{\text{ZTF}} - r_{\text{ZTF}}$	-0.064	-0.776	0.008	-0.756	0.032	11.549 ± 0.067	10	20.2	5.0, 94.8
V	$V - r$	0.316	-2.591	0.049	-1.030	0.055	11.617 ± 0.076	14	21.0	5.0, 115.4
V	$V - R$	0.164	-1.159	-0.031	-0.534	0.055	11.674 ± 0.134	5	21.6	7.7, 136.1
V	$V - i$	-0.082	-0.866	-0.065	-0.417	0.064	11.629 ± 0.061	14	20.2	5.0, 115.4
r	$r - i$	0.452	-1.914	-0.128	0.514	0.073	11.740 ± 0.118	14	22.2	5.0, 115.4
SNe Ic										
B	$B - V$	-0.147	-0.543	0.300	-1.247	0.067	11.480 ± 0.083	19	17.6	5.8, 146.6
B	$B - r$	-0.349	-0.225	0.314	-1.006	0.042	11.486 ± 0.068	16	16.9	5.8, 146.6
B	$B - R$	-0.407	-0.176	0.473	-1.037	0.058	11.575 ± 0.054	8	17.3	8.9, 146.6
B	$B - i$	-0.398	-0.165	0.298	-0.861	0.033	11.329 ± 0.044	16	16.4	5.8, 146.6
B	$B - I$	-0.361	-0.129	1.200	-1.161	0.059	11.474 ± 0.068	8	17.7	8.9, 146.6
g	$g - r$	-0.231	-0.505	0.186	-1.072	0.041	11.674 ± 0.094	12	16.8	8.9, 95.8
g	$g - i$	-0.393	-0.368	0.253	-1.044	0.035	11.570 ± 0.070	12	18.0	8.9, 95.8
g_{ZTF}	$g_{\text{ZTF}} - r_{\text{ZTF}}$	-0.241	-0.496	0.041	-0.908	0.048	11.696 ± 0.092	12	16.8	8.9, 95.8
V	$V - r$	-0.003	-1.856	-0.080	-0.821	0.059	11.828 ± 0.109	16	15.9	5.8, 146.6
V	$V - R$	0.131	-1.637	-0.073	-0.592	0.051	11.887 ± 0.052	8	19.6	8.9, 146.6
V	$V - i$	-0.490	-0.649	-0.042	-0.833	0.056	11.741 ± 0.088	16	18.5	5.8, 146.6
V	$V - I$	-0.228	-0.366	-0.277	-0.129	0.047	11.911 ± 0.040	8	23.7	8.9, 146.6
r	$r - i$	-0.649	-1.452	-0.159	-1.181	0.077	11.793 ± 0.136	16	27.0	5.8, 146.6

NOTE—BC = ZP + $a_1(x - y) + a_2(x - y)^2$ if $t - t_y^{\text{peak}} \leq t_{x-y}^{\max}$, otherwise BC = ZP + $a_3 + a_4(x - y)$.

Table F10. Bolometric light-curve properties, ejecta velocities, and explosion parameters^{*}

SN	t_L^{peak}	$\log L_{\text{peak}}$	$\Delta m_{15}(\text{bol})$	v_{peak}	M_{ej}	E_k
	(d)	(dex)	(mag)	(km s^{-1})	(M_{\odot})	(foe)
(1)	(2)	(3)	(4)	(5)	(6)	(7)
1993J	20.9 ± 0.1	-0.601 ± 0.002	0.880 ± 0.010	7000	3.4 ± 0.5	0.99 ± 0.45
1994I	9.6 ± 0.1	-0.589 ± 0.007	1.478 ± 0.020	9000	0.9 ± 0.3	0.44 ± 0.24
1996cb	21.0 ± 0.2	-0.943 ± 0.002	0.727 ± 0.007	7000	3.4 ± 0.7	0.99 ± 0.47
1998bw	16.0 ± 0.4	-0.235 ± 0.005	0.615 ± 0.018	15000	4.2 ± 0.6	5.68 ± 2.56
1999dn	16.3 ± 0.8	-0.831 ± 0.007	0.405 ± 0.022	9000	2.6 ± 0.7	1.27 ± 0.64
SN	$\log M_{\text{Ni}}^{\text{tail}}$	t_{esc}	$\log(L_{\text{peak}}/M_{\text{Ni}}^{\text{tail}})$	$\log M_{\text{Ni}}^{\text{peak}}$	$\log M_{\text{Ni}}$	M_{Ni}
	(dex)	(d)	(dex)	(dex)	(dex)	(M_{\odot})
(1)	(8)	(9)	(10)	(11)	(12)	(13)
1993J	-1.129 ± 0.070	109_{-2}^{+2}	0.528 ± 0.013	-1.139 ± 0.093	-1.129 ± 0.070	0.07524 ± 0.01221
1994I	-1.729 ± 0.126	112_{-3}^{+3}	1.140 ± 0.013	-1.659 ± 0.153	-1.729 ± 0.126	0.01948 ± 0.00576
1996cb	-1.344 ± 0.126	94_{-1}^{+1}	0.401 ± 0.020	-1.429 ± 0.146	-1.345 ± 0.126	0.04715 ± 0.01396
1998bw	-0.856 ± 0.122	116_{-1}^{+1}	0.621 ± 0.009	-0.802 ± 0.135	-0.856 ± 0.122	0.14492 ± 0.04139
1999dn	-1.322 ± 0.114	-1.322 ± 0.114	0.04932 ± 0.01314

NOTE—Column 1: SN name. Columns 2, 3, and 4: peak time, peak luminosity, and decline rate, respectively. Columns 5, 6, and 7: ejecta velocity at t_L^{peak} , ejecta mass, and kinetic energy, respectively. Columns 8 and 9: ^{56}Ni mass and γ -ray escape time, respectively, measured from the luminosity in the radioactive tail. Column 10: $\log L_{\text{peak}}$ minus $\log M_{\text{Ni}}^{\text{tail}}$. Column 11: ^{56}Ni mass computed from peak time, peak luminosity (and decline rate if it is available), and the empirical correlation we present in Section 4.2. Column 12 and 13: Weighted average of $\log M_{\text{Ni}}^{\text{tail}}$ and $\log M_{\text{Ni}}^{\text{peak}}$, and the corresponding ^{56}Ni mass, respectively. L_{peak} and M_{Ni} are in units of $10^{43} \text{ erg s}^{-1}$ and M_{\odot} , respectively. Uncertainties are 1σ errors, while lower and upper t_{esc} errors are 16th and 84th percentiles.

^{*}This table is available in its entirety in machine-readable form.

- Bessell, M., & Murphy, S. 2012, *PASP*, 124, 140, doi: [10.1086/664083](https://doi.org/10.1086/664083)
- Bianco, F. B., Modjaz, M., Hicken, M., et al. 2014, *ApJS*, 213, 19, doi: [10.1088/0067-0049/213/2/19](https://doi.org/10.1088/0067-0049/213/2/19)
- Bohlin, R. C., & Gilliland, R. L. 2004, *AJ*, 127, 3508, doi: [10.1086/420715](https://doi.org/10.1086/420715)
- Brown, P. J., Breeveld, A. A., Holland, S., Kuin, P., & Pritchard, T. 2014, *Ap&SS*, 354, 89, doi: [10.1007/s10509-014-2059-8](https://doi.org/10.1007/s10509-014-2059-8)
- Bufano, F., Pignata, G., Bersten, M., et al. 2014, *MNRAS*, 439, 1807, doi: [10.1093/mnras/stu065](https://doi.org/10.1093/mnras/stu065)
- Burrows, A., & Vartanyan, D. 2021, *Nature*, 589, 29, doi: [10.1038/s41586-020-03059-w](https://doi.org/10.1038/s41586-020-03059-w)
- Campana, S., Mangano, V., Blustin, A. J., et al. 2006, *Nature*, 442, 1008, doi: [10.1038/nature04892](https://doi.org/10.1038/nature04892)
- Cano, Z. 2013, *MNRAS*, 434, 1098, doi: [10.1093/mnras/stt1048](https://doi.org/10.1093/mnras/stt1048)
- Cao, Y., Kasliwal, M. M., Arcavi, I., et al. 2013, *ApJL*, 775, L7, doi: [10.1088/2041-8205/775/1/L7](https://doi.org/10.1088/2041-8205/775/1/L7)
- Chauvenet, W. 1863, *A manual of spherical and practical astronomy*
- Chen, J., Wang, X., Ganeshalingam, M., et al. 2014, *ApJ*, 790, 120, doi: [10.1088/0004-637X/790/2/120](https://doi.org/10.1088/0004-637X/790/2/120)
- Cleveland, W. S., Grosse, E., & Shyu, W. M. 1992, in *Statistical models in S*, ed. J. M. Chambers & T. J. Hastie (London: Chapman and Hall), 309–376
- Clocchiatti, A., Suntzeff, N. B., Covarrubias, R., & Candia, P. 2011, *AJ*, 141, 163, doi: [10.1088/0004-6256/141/5/163](https://doi.org/10.1088/0004-6256/141/5/163)
- Clocchiatti, A., & Wheeler, J. C. 1997, *ApJ*, 491, 375, doi: [10.1086/304961](https://doi.org/10.1086/304961)
- Colgate, S. A., & McKee, C. 1969, *ApJ*, 157, 623, doi: [10.1086/150102](https://doi.org/10.1086/150102)
- De, K., Kasliwal, M. M., Ofek, E. O., et al. 2018, *Science*, 362, 201, doi: [10.1126/science.aas8693](https://doi.org/10.1126/science.aas8693)
- Dessart, L., Hillier, D. J., Woosley, S., et al. 2015, *MNRAS*, 453, 2189, doi: [10.1093/mnras/stv1747](https://doi.org/10.1093/mnras/stv1747)
- . 2016, *MNRAS*, 458, 1618, doi: [10.1093/mnras/stw418](https://doi.org/10.1093/mnras/stw418)
- Drout, M. R., Soderberg, A. M., Gal-Yam, A., et al. 2011, *ApJ*, 741, 97, doi: [10.1088/0004-637X/741/2/97](https://doi.org/10.1088/0004-637X/741/2/97)
- Drout, M. R., Milisavljevic, D., Parrent, J., et al. 2016, *ApJ*, 821, 57, doi: [10.3847/0004-637X/821/1/57](https://doi.org/10.3847/0004-637X/821/1/57)

Table F11. SNe with ^{56}Ni masses estimated with hydrodynamical models.

SN	μ (mag)	E_{B-V}^{MW} (mag)	E_{B-V} (mag)	R_V	t_{expl} (MJD)	L_{peak} ($10^{43} \text{ erg s}^{-1}$)	M_{Ni} (M_{\odot})	Reference
1993J	27.80	0.030	0.0	...	49074.1	0.21	0.078	Utrobin (1996)
1994I	29.60	0.030	0.270	3.1	49438.5	0.23	0.070	Sauer et al. (2006)
1998bw	32.89	0.016	0.0	...	50928.9	1.00	0.400	Nakamura et al. (2001)
2004gq	32.00	0.065	0.108	2.4	53346.9	0.20	0.110	Taddia et al. (2018b)
2004gt	31.83	0.041	0.428	2.5	53342.8	0.31	0.160	Taddia et al. (2018b)
2006T	32.50	0.066	0.323	1.3	53757.6	0.23	0.120	Taddia et al. (2018b)
2006ep	33.96	0.032	0.118	5.1	53975.5	0.24	0.120	Taddia et al. (2018b)
2006fo	34.59	0.026	0.156	4.1	53983.4	0.41	0.250	Taddia et al. (2018b)
2007C	31.61	0.037	0.554	2.4	54095.4	0.16	0.070	Taddia et al. (2018b)
2007hn	35.27	0.071	0.134	4.1	54340.8	0.41	0.250	Taddia et al. (2018b)
2008D	32.46	0.020	0.630	3.1	54474.6	0.18	0.070	Tanaka et al. (2009)
2008aq	32.15	0.039	0.0	...	54510.8	0.09	0.040	Taddia et al. (2018b)
2008ax	29.45	0.019	0.300	3.1	54528.3	0.15	0.060	Folatelli et al. (2015)
2009bb	33.00	0.087	0.344	3.4	54909.1	0.58	0.250	Taddia et al. (2018b)
2010as	32.16	0.150	0.420	1.5	55270.8	0.27	0.120	Folatelli et al. (2014)
2011dh	29.26	0.035	0.0	...	55712.5	0.14	0.060	Bersten et al. (2012)
	29.46	0.031	0.040	3.1	55712.5	0.17	0.075	Ergon et al. (2015)
2011fu	34.36	0.068	0.032	3.1	55824.0	0.31	0.150	Morales-Garoffolo et al. (2015)
2012P	32.14	0.044	0.290	3.1	55932.5	0.13	0.063	Fremling et al. (2016)
iPTF13bvn	32.14	0.044	0.080	3.1	56458.7	0.17	0.072	Fremling et al. (2016)
	32.04	0.045	0.170	3.1	56458.7	0.18	0.100	Bersten et al. (2014)
iPTF15dtg	36.83	0.054	0.0	...	57332.9	0.50	0.620	Taddia et al. (2016)

Table F12. Na ID equivalent widths and reddenings for SNe II ^{*}

SN	$\text{EW}_{\text{NaID}}^{\text{MW}}$ (\AA)	E_{B-V}^{MW} (mag) ^a	EW_{NaID}	E_{B-V} (mag) ^b
1990K	1.000 ± 0.144	0.227 ± 0.034
1991al	0.470 ± 0.031	0.044 ± 0.007	0.421 ± 0.024	0.067 ± 0.026
1992ba	0.069 ± 0.075	0.050 ± 0.008	-0.041 ± 0.072	0.096 ± 0.029

^aValues from Schlafly & Finkbeiner (2011) with a random error of 16%.^bValues from Rodríguez et al. (2021).^{*}This table is available in its entirety in machine-readable form.Durrell, P. R., Sarajedini, A., & Chandar, R. 2010, ApJ, 718, 1118, doi: [10.1088/0004-637X/718/2/1118](https://doi.org/10.1088/0004-637X/718/2/1118)Elias, J. H., Matthews, K., Neugebauer, G., & Persson, S. E. 1985, ApJ, 296, 379, doi: [10.1086/163456](https://doi.org/10.1086/163456)Ergon, M., Sollerman, J., Fraser, M., et al. 2014, A&A, 562, A17, doi: [10.1051/0004-6361/201321850](https://doi.org/10.1051/0004-6361/201321850)Ergon, M., Jerkstrand, A., Sollerman, J., et al. 2015, A&A, 580, A142, doi: [10.1051/0004-6361/201424592](https://doi.org/10.1051/0004-6361/201424592)Ertl, T., Woosley, S. E., Sukhbold, T., & Janka, H. T. 2020, ApJ, 890, 51, doi: [10.3847/1538-4357/ab6458](https://doi.org/10.3847/1538-4357/ab6458)Filippenko, A. V. 1988, AJ, 96, 1941, doi: [10.1086/114940](https://doi.org/10.1086/114940)Fitzpatrick, E. L. 1999, PASP, 111, 63, doi: [10.1086/316293](https://doi.org/10.1086/316293)

Table F13. Host galaxy broad-band extinction parameters for optical bands^{*}

Type	x	c	$t - t_{x_2}^{\text{peak}} \leq t_c^{\text{max}}$				$t - t_{x_2}^{\text{peak}} > t_c^{\text{max}}$				$t - t_{x_2}^{\text{peak}}$ range (d)	
			$h_{x,c,0}$	$h_{x,c,1}$	$\hat{\sigma}$	N	$h_{x,c,0}$	$h_{x,c,1}$	$\hat{\sigma}$	N		
		$(x_1 - x_2)$										
IIb	B	$B-V$	3.497	-0.123	0.010	99	3.466	-0.104	0.009	46	-17, 117	
	B	$B-r$	3.496	-0.099	0.008	78	3.458	-0.078	0.004	30	-18, 106	
	B	$B-R$	3.498	-0.084	0.009	48	3.461	-0.068	0.007	27	-18, 106	

NOTE—The t_c^{max} values are listed in Column 11 of Table F9.

^{*}This table is available in its entirety in machine-readable form.

Table F14. K -correction parameters for optical bands^{*}

Type	x	c	$t - t_{x_2}^{\text{peak}} \leq t_c^{\text{max}}$					$t - t_{x_2}^{\text{peak}} > t_c^{\text{max}}$					$t - t_{x_2}^{\text{peak}}$ range (d)
			$k_{x,c,0}$	$k_{x,c,1}$	$k_{x,c,2}$	$\hat{\sigma}$	N	$k_{x,c,0}$	$k_{x,c,1}$	$k_{x,c,2}$	$\hat{\sigma}$	N	
		$(x_1 - x_2)$											
IIb	B	$B-V$	-1.171	5.515	3.747	0.648	87	0.782	3.919	3.511	0.688	44	-20, 117
	B	$B-r$	-0.905	4.311	3.725	0.575	74	-0.486	4.077	3.480	0.537	33	-18, 106
	B	$B-R$	-0.973	3.542	3.733	0.424	42	-0.650	3.613	3.417	0.472	27	-18, 106

NOTE—The t_c^{max} values are listed in Column 11 of Table F9.

^{*}This table is available in its entirety in machine-readable form.

Table F15. Galactic broad-band extinction parameters for optical bands^{*}

x	c	$t - t_{x_2}^{\text{peak}} \leq t_c^{\text{max}}$						$t - t_{x_2}^{\text{peak}} > t_c^{\text{max}}$						$t - t_{x_2}^{\text{peak}}$ range (d)	
		$g_{x,c,0}$	$g_{x,c,1}$	$g_{x,c,2}$	$g_{x,c,3}$	$\hat{\sigma}$	N	$g_{x,c,0}$	$g_{x,c,1}$	$g_{x,c,2}$	$g_{x,c,3}$	$\hat{\sigma}$	N		
	$(x_1 - x_2)$														
		SNe IIb													
B	$B-V$	4.101	-0.130	-0.103	-0.445	0.011	91	4.035	-0.078	-0.104	-0.643	0.009	44	-20, 117	
B	$B-r$	4.102	-0.107	-0.102	-0.517	0.009	75	4.064	-0.083	-0.104	-0.740	0.007	33	-18, 106	
B	$B-R$	4.103	-0.089	-0.102	-0.450	0.009	44	4.060	-0.069	-0.102	-0.730	0.006	27	-18, 106	

NOTE—The t_c^{max} values are listed in Column 11 of Table F9.

^{*}This table is available in its entirety in machine-readable form.

Table F16. Parameters of the A_x^h , A_x^{MW} and K -corrections for IR bands

Type	x	c	$h_{x,c,0}$	$\hat{\sigma}$	N	$k_{x,c,0}$	$k_{x,c,1}$	$k_{x,c,2}$	$\hat{\sigma}$	N	$g_{x,c,0}$	$\hat{\sigma}$	N
IIb	Y	$V-Y$	0.849	0.008	27	-1.547	3.947	1.672	1.494	22	1.101	0.013	27
	J	$V-J$	0.666	0.005	31	-3.809	-0.950	1.108	2.271	24	0.827	0.009	31
	H	$V-H$	0.427	0.001	30	-2.397	0.501	0.654	0.764	23	0.517	0.001	31
	K	$V-K$	0.289	0.001	29	-3.773	0.870	0.380	1.153	23	0.350	0.001	31
Ib	Y	$V-Y$	0.931	0.005	10	-0.662	1.822	2.086	0.456	7	1.109	0.013	11
	J	$V-J$	0.721	0.004	13	-3.991	-2.180	1.136	0.276	8	0.824	0.005	13
	H	$V-H$	0.457	0.001	12	-1.794	-0.273	0.718	1.064	7	0.517	0.001	13
	K	$V-K$	0.308	0.001	13	-1.961	2.922	0.408	0.857	6	0.349	0.001	13
Ic	Y	$V-Y$	1.333	0.008	11	-3.952	1.716	3.111	0.418	8	1.111	0.011	11
	J	$V-J$	0.995	0.009	11	-4.743	0.396	1.650	1.147	10	0.820	0.010	11
	H	$V-H$	0.607	0.001	10	-1.820	-0.133	0.985	0.149	7	0.517	0.002	11
	K	$V-K$	0.412	0.002	11	-2.536	-0.040	0.586	1.123	9	0.350	0.002	11

NOTE— $h_{x,c,1} = g_{x,c,1} = g_{x,c,2} = g_{x,c,3} = 0$.

- Folatelli, G., Bersten, M. C., Kuncarayakti, H., et al. 2015, *ApJ*, 811, 147, doi: [10.1088/0004-637X/811/2/147](https://doi.org/10.1088/0004-637X/811/2/147)
- Folatelli, G., Contreras, C., Phillips, M. M., et al. 2006, *ApJ*, 641, 1039, doi: [10.1086/500531](https://doi.org/10.1086/500531)
- Folatelli, G., Bersten, M. C., Kuncarayakti, H., et al. 2014, *ApJ*, 792, 7, doi: [10.1088/0004-637X/792/1/7](https://doi.org/10.1088/0004-637X/792/1/7)
- Folatelli, G., Van Dyk, S. D., Kuncarayakti, H., et al. 2016, *ApJL*, 825, L22, doi: [10.3847/2041-8205/825/2/L22](https://doi.org/10.3847/2041-8205/825/2/L22)
- Foley, R. J., Papenkova, M. S., Swift, B. J., et al. 2003, *PASP*, 115, 1220, doi: [10.1086/378242](https://doi.org/10.1086/378242)
- Foreman-Mackey, D., Hogg, D. W., Lang, D., & Goodman, J. 2013, *PASP*, 125, 306, doi: [10.1086/670067](https://doi.org/10.1086/670067)
- Fremming, C., Sollerman, J., Taddia, F., et al. 2016, *A&A*, 593, A68, doi: [10.1051/0004-6361/201628275](https://doi.org/10.1051/0004-6361/201628275)
- Fremming, C., Miller, A. A., Sharma, Y., et al. 2020, *ApJ*, 895, 32, doi: [10.3847/1538-4357/ab8943](https://doi.org/10.3847/1538-4357/ab8943)
- Fukugita, M., Ichikawa, T., Gunn, J. E., et al. 1996, *AJ*, 111, 1748, doi: [10.1086/117915](https://doi.org/10.1086/117915)
- Gal-Yam, A., Yaron, O., Pastorello, A., et al. 2021, *Transient Name Server AstroNote*, 76, 1
- Gal-Yam, A., Bruch, R., Schulze, S., et al. 2022, *Nature*, 601, 201, doi: [10.1038/s41586-021-04155-1](https://doi.org/10.1038/s41586-021-04155-1)
- Galama, T. J., Vreeswijk, P. M., van Paradijs, J., et al. 1998, *Nature*, 395, 670, doi: [10.1038/27150](https://doi.org/10.1038/27150)
- Gangopadhyay, A., Misra, K., Pastorello, A., et al. 2018, *MNRAS*, 476, 3611, doi: [10.1093/mnras/sty478](https://doi.org/10.1093/mnras/sty478)
- Gangopadhyay, A., Misra, K., Sahu, D. K., et al. 2020, *MNRAS*, 497, 3770, doi: [10.1093/mnras/staa1821](https://doi.org/10.1093/mnras/staa1821)
- Gerke, J. R., Kochanek, C. S., Prieto, J. L., Stanek, K. Z., & Macri, L. M. 2011, *ApJ*, 743, 176, doi: [10.1088/0004-637X/743/2/176](https://doi.org/10.1088/0004-637X/743/2/176)
- Gomez, S., Berger, E., Hosseinzadeh, G., et al. 2021, *ApJ*, 913, 143, doi: [10.3847/1538-4357/abf5e3](https://doi.org/10.3847/1538-4357/abf5e3)
- Graham, M. J., Kulkarni, S. R., Bellm, E. C., et al. 2019, *PASP*, 131, 078001, doi: [10.1088/1538-3873/ab006c](https://doi.org/10.1088/1538-3873/ab006c)
- Graziani, R., Courtois, H. M., Lavaux, G., et al. 2019, *MNRAS*, 488, 5438, doi: [10.1093/mnras/stz078](https://doi.org/10.1093/mnras/stz078)
- Gutiérrez, C. P., Bersten, M. C., Orellana, M., et al. 2021, *MNRAS*, 504, 4907, doi: [10.1093/mnras/stab1009](https://doi.org/10.1093/mnras/stab1009)
- Hamuy, M., Folatelli, G., Morrell, N. I., et al. 2006, *PASP*, 118, 2, doi: [10.1086/500228](https://doi.org/10.1086/500228)
- Hamuy, M. A. 2001, PhD thesis, The University of Arizona
- Hayes, D. S., & Latham, D. W. 1975, *ApJ*, 197, 593, doi: [10.1086/153548](https://doi.org/10.1086/153548)
- Ho, A. Y. Q., Kulkarni, S. R., Perley, D. A., et al. 2020, *ApJ*, 902, 86, doi: [10.3847/1538-4357/aba630](https://doi.org/10.3847/1538-4357/aba630)
- Ho, L. C., & Filippenko, A. V. 1995, *ApJ*, 444, 165, doi: [10.1086/175591](https://doi.org/10.1086/175591)
- Hunter, D. J., Valenti, S., Kotak, R., et al. 2009, *A&A*, 508, 371, doi: [10.1051/0004-6361/200912896](https://doi.org/10.1051/0004-6361/200912896)
- Jang, I. S., & Lee, M. G. 2017, *ApJ*, 836, 74, doi: [10.3847/1538-4357/836/1/74](https://doi.org/10.3847/1538-4357/836/1/74)
- Jeffery, D. J. 1999, arXiv e-prints, astro, <https://arxiv.org/abs/astro-ph/9907015>
- Katz, B., Kushnir, D., & Dong, S. 2013, arXiv e-prints, arXiv:1301.6766. <https://arxiv.org/abs/1301.6766>
- Khatami, D. K., & Kasen, D. N. 2019, *ApJ*, 878, 56, doi: [10.3847/1538-4357/ab1f09](https://doi.org/10.3847/1538-4357/ab1f09)
- Kilpatrick, C. D., Takaro, T., Foley, R. J., et al. 2018, *MNRAS*, 480, 2072, doi: [10.1093/mnras/sty2022](https://doi.org/10.1093/mnras/sty2022)
- Kilpatrick, C. D., Drout, M. R., Auchettl, K., et al. 2021, *MNRAS*, 504, 2073, doi: [10.1093/mnras/stab838](https://doi.org/10.1093/mnras/stab838)
- Kourkchi, E., Courtois, H. M., Graziani, R., et al. 2020, *AJ*, 159, 67, doi: [10.3847/1538-3881/ab620e](https://doi.org/10.3847/1538-3881/ab620e)
- Krisciunas, K., Contreras, C., Burns, C. R., et al. 2017, *AJ*, 154, 211, doi: [10.3847/1538-3881/aa8df0](https://doi.org/10.3847/1538-3881/aa8df0)
- Kumar, B., Singh, A., Srivastav, S., Sahu, D. K., & Anupama, G. C. 2018, *MNRAS*, 473, 3776, doi: [10.1093/mnras/stx2498](https://doi.org/10.1093/mnras/stx2498)
- Kumar, B., Pandey, S. B., Sahu, D. K., et al. 2013, *MNRAS*, 431, 308, doi: [10.1093/mnras/stt162](https://doi.org/10.1093/mnras/stt162)
- Kushnir, D. 2015, arXiv e-prints, arXiv:1506.02655. <https://arxiv.org/abs/1506.02655>
- Kwok, L. A., Williamson, M., Jha, S. W., et al. 2022, *ApJ*, 937, 40, doi: [10.3847/1538-4357/ac8989](https://doi.org/10.3847/1538-4357/ac8989)
- Lien, A., & Fields, B. D. 2009, *JCAP*, 2009, 047, doi: [10.1088/1475-7516/2009/01/047](https://doi.org/10.1088/1475-7516/2009/01/047)
- Liu, Z., Zhao, X.-L., Huang, F., et al. 2015, *Research in Astronomy and Astrophysics*, 15, 225, doi: [10.1088/1674-4527/15/2/007](https://doi.org/10.1088/1674-4527/15/2/007)
- Lusk, J. A., & Baron, E. 2017, *PASP*, 129, 044202, doi: [10.1088/1538-3873/aa5e49](https://doi.org/10.1088/1538-3873/aa5e49)
- Lyman, J. D., Bersier, D., & James, P. A. 2014, *MNRAS*, 437, 3848, doi: [10.1093/mnras/stt2187](https://doi.org/10.1093/mnras/stt2187)
- Lyman, J. D., Bersier, D., James, P. A., et al. 2016, *MNRAS*, 457, 328, doi: [10.1093/mnras/stv2983](https://doi.org/10.1093/mnras/stv2983)
- Malesani, D., Fynbo, J. P. U., Hjorth, J., et al. 2009, *ApJL*, 692, L84, doi: [10.1088/0004-637X/692/2/L84](https://doi.org/10.1088/0004-637X/692/2/L84)
- Maoz, D., & Graur, O. 2017, *ApJ*, 848, 25, doi: [10.3847/1538-4357/aa8b6e](https://doi.org/10.3847/1538-4357/aa8b6e)
- Masci, F. J., Laher, R. R., Rusholme, B., et al. 2019, *PASP*, 131, 018003, doi: [10.1088/1538-3873/aae8ac](https://doi.org/10.1088/1538-3873/aae8ac)
- Matthews, K., Neugebauer, G., Armus, L., & Soifer, B. T. 2002, *AJ*, 123, 753, doi: [10.1086/338646](https://doi.org/10.1086/338646)
- Mazzali, P. A., Deng, J., Maeda, K., et al. 2002, *ApJL*, 572, L61, doi: [10.1086/341504](https://doi.org/10.1086/341504)
- McKenzie, E. H., & Schaefer, B. E. 1999, *PASP*, 111, 964, doi: [10.1086/316404](https://doi.org/10.1086/316404)

- McQuinn, K. B. W., Skillman, E. D., Dolphin, A. E., Berg, D., & Kennicutt, R. 2017, *AJ*, 154, 51, doi: [10.3847/1538-3881/aa7aad](https://doi.org/10.3847/1538-3881/aa7aad)
- Medler, K., Mazzali, P. A., Teffs, J., et al. 2021, *MNRAS*, 506, 1832, doi: [10.1093/mnras/stab1761](https://doi.org/10.1093/mnras/stab1761)
- Meza, N., & Anderson, J. P. 2020, *A&A*, 641, A177, doi: [10.1051/0004-6361/201937113](https://doi.org/10.1051/0004-6361/201937113)
- Milisavljevic, D., Margutti, R., Soderberg, A. M., et al. 2013a, *ApJ*, 767, 71, doi: [10.1088/0004-637X/767/1/71](https://doi.org/10.1088/0004-637X/767/1/71)
- Milisavljevic, D., Soderberg, A. M., Margutti, R., et al. 2013b, *ApJL*, 770, L38, doi: [10.1088/2041-8205/770/2/L38](https://doi.org/10.1088/2041-8205/770/2/L38)
- Minkowski, R. 1941, *PASP*, 53, 224, doi: [10.1086/125315](https://doi.org/10.1086/125315)
- Modjaz, M., Liu, Y. Q., Bianco, F. B., & Graur, O. 2016, *ApJ*, 832, 108, doi: [10.3847/0004-637X/832/2/108](https://doi.org/10.3847/0004-637X/832/2/108)
- Modjaz, M., Li, W., Butler, N., et al. 2009, *ApJ*, 702, 226, doi: [10.1088/0004-637X/702/1/226](https://doi.org/10.1088/0004-637X/702/1/226)
- Morales-Garoffolo, A., Elias-Rosa, N., Benetti, S., et al. 2014, *MNRAS*, 445, 1647, doi: [10.1093/mnras/stu1837](https://doi.org/10.1093/mnras/stu1837)
- Morales-Garoffolo, A., Elias-Rosa, N., Bersten, M., et al. 2015, *MNRAS*, 454, 95, doi: [10.1093/mnras/stv1972](https://doi.org/10.1093/mnras/stv1972)
- Nakamura, T., Mazzali, P. A., Nomoto, K., & Iwamoto, K. 2001, *ApJ*, 550, 991, doi: [10.1086/319784](https://doi.org/10.1086/319784)
- Nakar, E., & Piro, A. L. 2014, *ApJ*, 788, 193, doi: [10.1088/0004-637X/788/2/193](https://doi.org/10.1088/0004-637X/788/2/193)
- Ouchi, R., Maeda, K., Anderson, J. P., & Sawada, R. 2021, *ApJ*, 922, 141, doi: [10.3847/1538-4357/ac2306](https://doi.org/10.3847/1538-4357/ac2306)
- Pandey, S. B., Anupama, G. C., Sagar, R., et al. 2003, *MNRAS*, 340, 375, doi: [10.1046/j.1365-8711.2003.06148.x](https://doi.org/10.1046/j.1365-8711.2003.06148.x)
- Pandey, S. B., Kumar, A., Kumar, B., et al. 2021, *MNRAS*, 507, 1229, doi: [10.1093/mnras/stab1889](https://doi.org/10.1093/mnras/stab1889)
- Pastorello, A., Taubenberger, S., Elias-Rosa, N., et al. 2007, *MNRAS*, 376, 1301, doi: [10.1111/j.1365-2966.2007.11527.x](https://doi.org/10.1111/j.1365-2966.2007.11527.x)
- Pastorello, A., Mattila, S., Zampieri, L., et al. 2008a, *MNRAS*, 389, 113, doi: [10.1111/j.1365-2966.2008.13602.x](https://doi.org/10.1111/j.1365-2966.2008.13602.x)
- Pastorello, A., Kasliwal, M. M., Crockett, R. M., et al. 2008b, *MNRAS*, 389, 955, doi: [10.1111/j.1365-2966.2008.13618.x](https://doi.org/10.1111/j.1365-2966.2008.13618.x)
- Patat, F., Cappellaro, E., Danziger, J., et al. 2001, *ApJ*, 555, 900, doi: [10.1086/321526](https://doi.org/10.1086/321526)
- Pejcha, O., & Thompson, T. A. 2015, *ApJ*, 801, 90, doi: [10.1088/0004-637X/801/2/90](https://doi.org/10.1088/0004-637X/801/2/90)
- Perley, D. A., Fremling, C., Sollerman, J., et al. 2020, *ApJ*, 904, 35, doi: [10.3847/1538-4357/abd98](https://doi.org/10.3847/1538-4357/abd98)
- Phillips, M. M., Simon, J. D., Morrell, N., et al. 2013, *ApJ*, 779, 38, doi: [10.1088/0004-637X/779/1/38](https://doi.org/10.1088/0004-637X/779/1/38)
- Pian, E., Mazzali, P. A., Moriya, T. J., et al. 2020, *MNRAS*, 497, 3542, doi: [10.1093/mnras/staa2191](https://doi.org/10.1093/mnras/staa2191)
- Pignata, G., Stritzinger, M., Soderberg, A., et al. 2011, *ApJ*, 728, 14, doi: [10.1088/0004-637X/728/1/14](https://doi.org/10.1088/0004-637X/728/1/14)
- Poole, T. S., Breeveld, A. A., Page, M. J., et al. 2008, *MNRAS*, 383, 627, doi: [10.1111/j.1365-2966.2007.12563.x](https://doi.org/10.1111/j.1365-2966.2007.12563.x)
- Pooley, G. G., Green, D. A., & Romanishin, W. 1993, *IAUC*, 5773, 1
- Poznanski, D., Ganeshalingam, M., Silverman, J. M., & Filippenko, A. V. 2011, *MNRAS*, 415, L81, doi: [10.1111/j.1745-3933.2011.01084.x](https://doi.org/10.1111/j.1745-3933.2011.01084.x)
- Poznanski, D., Prochaska, J. X., & Bloom, J. S. 2012, *MNRAS*, 426, 1465, doi: [10.1111/j.1365-2966.2012.21796.x](https://doi.org/10.1111/j.1365-2966.2012.21796.x)
- Prentice, S. J., Mazzali, P. A., Pian, E., et al. 2016, *MNRAS*, 458, 2973, doi: [10.1093/mnras/stw299](https://doi.org/10.1093/mnras/stw299)
- Prentice, S. J., Ashall, C., Mazzali, P. A., et al. 2018, *MNRAS*, 478, 4162, doi: [10.1093/mnras/sty1223](https://doi.org/10.1093/mnras/sty1223)
- Prentice, S. J., Ashall, C., James, P. A., et al. 2019, *MNRAS*, 485, 1559, doi: [10.1093/mnras/sty3399](https://doi.org/10.1093/mnras/sty3399)
- Pritchard, T. A., Roming, P. W. A., Brown, P. J., Bayless, A. J., & Frey, L. H. 2014, *ApJ*, 787, 157, doi: [10.1088/0004-637X/787/2/157](https://doi.org/10.1088/0004-637X/787/2/157)
- Qiu, Y., Li, W., Qiao, Q., & Hu, J. 1999, *AJ*, 117, 736, doi: [10.1086/300731](https://doi.org/10.1086/300731)
- Rho, J., Evans, A., Geballe, T. R., et al. 2021, *ApJ*, 908, 232, doi: [10.3847/1538-4357/abd850](https://doi.org/10.3847/1538-4357/abd850)
- Richmond, M. W., Treffers, R. R., Filippenko, A. V., & Paik, Y. 1996a, *AJ*, 112, 732, doi: [10.1086/118048](https://doi.org/10.1086/118048)
- Richmond, M. W., Treffers, R. R., Filippenko, A. V., et al. 1994, *AJ*, 107, 1022, doi: [10.1086/116915](https://doi.org/10.1086/116915)
- Richmond, M. W., van Dyk, S. D., Ho, W., et al. 1996b, *AJ*, 111, 327, doi: [10.1086/117785](https://doi.org/10.1086/117785)
- Riess, A. G., Casertano, S., Yuan, W., Macri, L. M., & Scolnic, D. 2019, *ApJ*, 876, 85, doi: [10.3847/1538-4357/ab1422](https://doi.org/10.3847/1538-4357/ab1422)
- Riess, A. G., Macri, L. M., Hoffmann, S. L., et al. 2016, *ApJ*, 826, 56, doi: [10.3847/0004-637X/826/1/56](https://doi.org/10.3847/0004-637X/826/1/56)
- Ritchey, A. M., & Wallerstein, G. 2012, *ApJL*, 748, L11, doi: [10.1088/2041-8205/748/1/L11](https://doi.org/10.1088/2041-8205/748/1/L11)
- Rodrigo, C., & Solano, E. 2020, in XIV.0 Scientific Meeting (virtual) of the Spanish Astronomical Society, 182
- Rodrigo, C., Solano, E., & Bayo, A. 2012, SVO Filter Profile Service Version 1.0, IVOA Working Draft 15 October 2012
- Rodríguez, Ó. 2022, *MNRAS*, 515, 897, doi: [10.1093/mnras/stac1831](https://doi.org/10.1093/mnras/stac1831)
- Rodríguez, Ó., Meza, N., Pineda-García, J., & Ramirez, M. 2021, *MNRAS*, 505, 1742, doi: [10.1093/mnras/stab1335](https://doi.org/10.1093/mnras/stab1335)
- Rodríguez, Ó., Nakar, E., & Maoz, D. 2023, submitted to *Nature*

- Rodríguez, Ó., Pignata, G., Hamuy, M., et al. 2019, *MNRAS*, 483, 5459, doi: [10.1093/mnras/sty3396](https://doi.org/10.1093/mnras/sty3396)
- Roming, P. W. A., Pritchard, T. A., Brown, P. J., et al. 2009, *ApJL*, 704, L118, doi: [10.1088/0004-637X/704/2/L118](https://doi.org/10.1088/0004-637X/704/2/L118)
- Roy, R., Kumar, B., Maund, J. R., et al. 2013, *MNRAS*, 434, 2032, doi: [10.1093/mnras/stt1148](https://doi.org/10.1093/mnras/stt1148)
- Saha, A., Thim, F., Tammann, G. A., Reindl, B., & Sandage, A. 2006, *ApJS*, 165, 108, doi: [10.1086/503800](https://doi.org/10.1086/503800)
- Sahu, D. K., Anupama, G. C., Chakradhari, N. K., et al. 2018, *MNRAS*, 475, 2591, doi: [10.1093/mnras/stx3212](https://doi.org/10.1093/mnras/stx3212)
- Sahu, D. K., Tanaka, M., Anupama, G. C., Gurugubelli, U. K., & Nomoto, K. 2009, *ApJ*, 697, 676, doi: [10.1088/0004-637X/697/1/676](https://doi.org/10.1088/0004-637X/697/1/676)
- Sako, M., Bassett, B., Becker, A. C., et al. 2018, *PASP*, 130, 064002, doi: [10.1088/1538-3873/aab4e0](https://doi.org/10.1088/1538-3873/aab4e0)
- Sánchez-Sáez, P., Reyes, I., Valenzuela, C., et al. 2021, *AJ*, 161, 141, doi: [10.3847/1538-3881/abd5c1](https://doi.org/10.3847/1538-3881/abd5c1)
- Sauer, D. N., Mazzali, P. A., Deng, J., et al. 2006, *MNRAS*, 369, 1939, doi: [10.1111/j.1365-2966.2006.10438.x](https://doi.org/10.1111/j.1365-2966.2006.10438.x)
- Schlafly, E. F., & Finkbeiner, D. P. 2011, *ApJ*, 737, 103, doi: [10.1088/0004-637X/737/2/103](https://doi.org/10.1088/0004-637X/737/2/103)
- Schlegel, D. J., Finkbeiner, D. P., & Davis, M. 1998, *ApJ*, 500, 525, doi: [10.1086/305772](https://doi.org/10.1086/305772)
- Scholz, F. W., & Stephens, M. A. 1987, *Journal of the American Statistical Association*, 82, 918, doi: [10.1080/01621459.1987.10478517](https://doi.org/10.1080/01621459.1987.10478517)
- Schwarz, G. 1978, *Annals of Statistics*, 6, 461
- Sharon, A., & Kushnir, D. 2020, *MNRAS*, 496, 4517, doi: [10.1093/mnras/staa1745](https://doi.org/10.1093/mnras/staa1745)
- Shaya, E. J., Tully, R. B., Hoffman, Y., & Pomarède, D. 2017, *ApJ*, 850, 207, doi: [10.3847/1538-4357/aa9525](https://doi.org/10.3847/1538-4357/aa9525)
- Shivvers, I., Modjaz, M., Zheng, W., et al. 2017, *PASP*, 129, 054201, doi: [10.1088/1538-3873/aa54a6](https://doi.org/10.1088/1538-3873/aa54a6)
- Singh, M., Misra, K., Valenti, S., et al. 2021, *ApJ*, 909, 100, doi: [10.3847/1538-4357/abdf5c](https://doi.org/10.3847/1538-4357/abdf5c)
- Smartt, S. J., Eldridge, J. J., Crockett, R. M., & Maund, J. R. 2009, *MNRAS*, 395, 1409, doi: [10.1111/j.1365-2966.2009.14506.x](https://doi.org/10.1111/j.1365-2966.2009.14506.x)
- Sollerman, J., Yang, S., Perley, D., et al. 2022, *A&A*, 657, A64, doi: [10.1051/0004-6361/202142049](https://doi.org/10.1051/0004-6361/202142049)
- Sollerman, J., Holland, S. T., Challis, P., et al. 2002, *A&A*, 386, 944, doi: [10.1051/0004-6361:20020326](https://doi.org/10.1051/0004-6361:20020326)
- Srivastav, S., Anupama, G. C., & Sahu, D. K. 2014, *MNRAS*, 445, 1932, doi: [10.1093/mnras/stu1878](https://doi.org/10.1093/mnras/stu1878)
- Stritzinger, M., & Leibundgut, B. 2005, *A&A*, 431, 423, doi: [10.1051/0004-6361:20041630](https://doi.org/10.1051/0004-6361:20041630)
- Stritzinger, M., Suntzeff, N. B., Hamuy, M., et al. 2005, *PASP*, 117, 810, doi: [10.1086/431468](https://doi.org/10.1086/431468)
- Stritzinger, M., Hamuy, M., Suntzeff, N. B., et al. 2002, *AJ*, 124, 2100, doi: [10.1086/342544](https://doi.org/10.1086/342544)
- Stritzinger, M., Mazzali, P., Phillips, M. M., et al. 2009, *ApJ*, 696, 713, doi: [10.1088/0004-637X/696/1/713](https://doi.org/10.1088/0004-637X/696/1/713)
- Stritzinger, M. D., Taddia, F., Burns, C. R., et al. 2018a, *A&A*, 609, A135, doi: [10.1051/0004-6361/201730843](https://doi.org/10.1051/0004-6361/201730843)
- Stritzinger, M. D., Anderson, J. P., Contreras, C., et al. 2018b, *A&A*, 609, A134, doi: [10.1051/0004-6361/201730842](https://doi.org/10.1051/0004-6361/201730842)
- Stritzinger, M. D., Taddia, F., Holmbo, S., et al. 2020, *A&A*, 634, A21, doi: [10.1051/0004-6361/201936619](https://doi.org/10.1051/0004-6361/201936619)
- Strotjohann, N. L., Ofek, E. O., Gal-Yam, A., et al. 2015, *ApJ*, 811, 117, doi: [10.1088/0004-637X/811/2/117](https://doi.org/10.1088/0004-637X/811/2/117)
- Sukhbold, T., Ertl, T., Woosley, S. E., Brown, J. M., & Janka, H. T. 2016, *ApJ*, 821, 38, doi: [10.3847/0004-637X/821/1/38](https://doi.org/10.3847/0004-637X/821/1/38)
- Suwa, Y., Tominaga, N., & Maeda, K. 2019, *MNRAS*, 483, 3607, doi: [10.1093/mnras/sty3309](https://doi.org/10.1093/mnras/sty3309)
- Szalai, T., Vinkó, J., Nagy, A. P., et al. 2016, *MNRAS*, 460, 1500, doi: [10.1093/mnras/stw1031](https://doi.org/10.1093/mnras/stw1031)
- Taddia, F., Sollerman, J., Leloudas, G., et al. 2015, *A&A*, 574, A60, doi: [10.1051/0004-6361/201423915](https://doi.org/10.1051/0004-6361/201423915)
- Taddia, F., Fremling, C., Sollerman, J., et al. 2016, *A&A*, 592, A89, doi: [10.1051/0004-6361/201628703](https://doi.org/10.1051/0004-6361/201628703)
- Taddia, F., Sollerman, J., Fremling, C., et al. 2018a, *A&A*, 609, A106, doi: [10.1051/0004-6361/201629874](https://doi.org/10.1051/0004-6361/201629874)
- Taddia, F., Stritzinger, M. D., Bersten, M., et al. 2018b, *A&A*, 609, A136, doi: [10.1051/0004-6361/201730844](https://doi.org/10.1051/0004-6361/201730844)
- Taddia, F., Sollerman, J., Fremling, C., et al. 2019, *A&A*, 621, A71, doi: [10.1051/0004-6361/201834429](https://doi.org/10.1051/0004-6361/201834429)
- Takada-Hidai, M., Aoki, W., & Zhao, G. 2002, *PASJ*, 54, 899, doi: [10.1093/pasj/54.6.899](https://doi.org/10.1093/pasj/54.6.899)
- Takahashi, I., Suzuki, N., Yasuda, N., et al. 2020, *PASJ*, 72, 89, doi: [10.1093/pasj/psaa082](https://doi.org/10.1093/pasj/psaa082)
- Tanaka, M., Tominaga, N., Nomoto, K., et al. 2009, *ApJ*, 692, 1131, doi: [10.1088/0004-637X/692/2/1131](https://doi.org/10.1088/0004-637X/692/2/1131)
- Tartaglia, L., Fraser, M., Sand, D. J., et al. 2017, *ApJL*, 836, L12, doi: [10.3847/2041-8213/aa5c7f](https://doi.org/10.3847/2041-8213/aa5c7f)
- Taubenberger, S., Pastorello, A., Mazzali, P. A., et al. 2006, *MNRAS*, 371, 1459, doi: [10.1111/j.1365-2966.2006.10776.x](https://doi.org/10.1111/j.1365-2966.2006.10776.x)
- Taubenberger, S., Navasardyan, H., Maurer, J. I., et al. 2011, *MNRAS*, 413, 2140, doi: [10.1111/j.1365-2966.2011.18287.x](https://doi.org/10.1111/j.1365-2966.2011.18287.x)
- Teffs, J. J., Prentice, S. J., Mazzali, P. A., & Ashall, C. 2021, *MNRAS*, 502, 3829, doi: [10.1093/mnras/stab258](https://doi.org/10.1093/mnras/stab258)
- Terreran, G., Margutti, R., Bersier, D., et al. 2019, *ApJ*, 883, 147, doi: [10.3847/1538-4357/ab3e37](https://doi.org/10.3847/1538-4357/ab3e37)
- Tominaga, N., Tanaka, M., Nomoto, K., et al. 2005, *ApJL*, 633, L97, doi: [10.1086/498570](https://doi.org/10.1086/498570)

- Tomita, H., Deng, J., Maeda, K., et al. 2006, *ApJ*, 644, 400, doi: [10.1086/503554](https://doi.org/10.1086/503554)
- Trammell, S. R., Hines, D. C., Wheeler, J. C., et al. 1993, *IAUC*, 5780, 2
- Tsvetkov, D. Y., Pavlyuk, N., & Echeistov, V. 2020, *Peremennye Zvezdy*, 40, 1. <https://arxiv.org/abs/2007.05333>
- Tsvetkov, D. Y., Volkov, I. M., Baklanov, P., Blinnikov, S., & Tuchin, O. 2009, *Peremennye Zvezdy*, 29, 2. <https://arxiv.org/abs/0910.4242>
- Tukey, J. W. 1977, *Exploratory data analysis*
- Tully, R. B., Rizzi, L., Shaya, E. J., et al. 2009, *AJ*, 138, 323, doi: [10.1088/0004-6256/138/2/323](https://doi.org/10.1088/0004-6256/138/2/323)
- Turatto, M., Benetti, S., & Cappellaro, E. 2003, in *From Twilight to Highlight: The Physics of Supernovae*, ed. W. Hillebrandt & B. Leibundgut, 200, doi: [10.1007/10828549_26](https://doi.org/10.1007/10828549_26)
- Ugliano, M., Janka, H.-T., Marek, A., & Arcones, A. 2012, *ApJ*, 757, 69, doi: [10.1088/0004-637X/757/1/69](https://doi.org/10.1088/0004-637X/757/1/69)
- Utrobin, V. P. 1996, *A&A*, 306, 219
- Valenti, S., Benetti, S., Cappellaro, E., et al. 2008a, *MNRAS*, 383, 1485, doi: [10.1111/j.1365-2966.2007.12647.x](https://doi.org/10.1111/j.1365-2966.2007.12647.x)
- Valenti, S., Elias-Rosa, N., Taubenberger, S., et al. 2008b, *ApJL*, 673, L155, doi: [10.1086/527672](https://doi.org/10.1086/527672)
- Valenti, S., Fraser, M., Benetti, S., et al. 2011, *MNRAS*, 416, 3138, doi: [10.1111/j.1365-2966.2011.19262.x](https://doi.org/10.1111/j.1365-2966.2011.19262.x)
- Valenti, S., Taubenberger, S., Pastorello, A., et al. 2012, *ApJL*, 749, L28, doi: [10.1088/2041-8205/749/2/L28](https://doi.org/10.1088/2041-8205/749/2/L28)
- Van Dyk, S. D., Zheng, W., Fox, O. D., et al. 2014, *AJ*, 147, 37, doi: [10.1088/0004-6256/147/2/37](https://doi.org/10.1088/0004-6256/147/2/37)
- Van Dyk, S. D., Zheng, W., Brink, T. G., et al. 2018, *ApJ*, 860, 90, doi: [10.3847/1538-4357/aac32c](https://doi.org/10.3847/1538-4357/aac32c)
- Vladilo, G., Centurion, M., de Boer, K. S., et al. 1993, *A&A*, 280, L11
- Vollmann, K., & Eversberg, T. 2006, *Astronomische Nachrichten*, 327, 862, doi: [10.1002/asna.200610645](https://doi.org/10.1002/asna.200610645)
- Wada, T., & Ueno, M. 1997, *AJ*, 113, 231, doi: [10.1086/118247](https://doi.org/10.1086/118247)
- Wang, L., Strovink, M., Conley, A., et al. 2006, *ApJ*, 641, 50, doi: [10.1086/500422](https://doi.org/10.1086/500422)
- Weinberg, D. H., Andrews, B. H., & Freudenburg, J. 2017, *ApJ*, 837, 183, doi: [10.3847/1538-4357/837/2/183](https://doi.org/10.3847/1538-4357/837/2/183)
- Wheeler, J. C., & Harkness, R. P. 1986, in *NATO Advanced Study Institute (ASI) Series C, Vol. 180, Galaxy Distances and Deviations from Universal Expansion*, ed. B. F. Madore & R. B. Tully, 45–54
- Wheeler, J. C., & Levreault, R. 1985, *ApJL*, 294, L17, doi: [10.1086/184500](https://doi.org/10.1086/184500)
- Woosley, S. E., Sukhbold, T., & Kasen, D. N. 2021, *ApJ*, 913, 145, doi: [10.3847/1538-4357/abf3be](https://doi.org/10.3847/1538-4357/abf3be)
- Wygoda, N., Elbaz, Y., & Katz, B. 2019, *MNRAS*, 484, 3941, doi: [10.1093/mnras/stz145](https://doi.org/10.1093/mnras/stz145)
- Xiang, D., Wang, X., Mo, J., et al. 2019, *ApJ*, 871, 176, doi: [10.3847/1538-4357/aaf8b0](https://doi.org/10.3847/1538-4357/aaf8b0)
- Yoshii, Y., Tomita, H., Kobayashi, Y., et al. 2003, *ApJ*, 592, 467, doi: [10.1086/375572](https://doi.org/10.1086/375572)
- Zhang, J., Wang, X., Vinkó, J., et al. 2018, *ApJ*, 863, 109, doi: [10.3847/1538-4357/aaceaf](https://doi.org/10.3847/1538-4357/aaceaf)